

**CHARACTERIZATION OF YTTRIA STABILIZED ZIRCONIA AND CARBON
NANOTUBE DOPED - YSZ CERAMIC COMPOSITES FABRICATED BY SPARK
PLASMA SINTERING**

by

Abhinav Karanam

B.E., College of Engineering, Guindy, Anna University, 2012

A THESIS SUBMITTED IN PARTIAL FULFILLMENT OF
THE REQUIREMENTS FOR THE DEGREE OF

MASTER OF APPLIED SCIENCE

in

THE COLLEGE OF GRADUATE STUDIES

(Mechanical Engineering)

THE UNIVERSITY OF BRITISH COLUMBIA

(Okanagan)

August 2015

© Abhinav Karanam, 2015

Abstract

Zirconium oxide doped with Ytria has been recognized as a candidate material for thermal barrier coatings (TBC) due to its high thermal stability, inertness and corrosion resistance. Literature suggests that addition of Carbon Nanotubes (CNTs) to technical ceramics (e.g., Alumina) may significantly enhance the mechanical properties of the ceramic composite. However, the agglomeration of CNTs in the ceramic matrix during the fabrication process generally has a detrimental effect on the ceramic composite's mechanical properties. It was seen that during conventional sintering processes, CNTs may disintegrate when exposed to sintering temperatures for a long time, thus creating a need to identify a novel technique for successfully fabricating CNT-ceramic composites. Spark Plasma Sintering (SPS) is a novel method for fabricating ceramic composites, which are difficult to fabricate using traditional methods.

In this work, 8mol% YSZ was fabricated via SPS process, and the effect of varying sintering parameters was investigated. Also, the effect of adding Single-Wall CNTs (SWCNTs) and Multi-Wall CNTs (MWCNTs) on the densification behavior, mechanical and thermal properties of the CNT-YSZ composites were studied. The results suggest that MWCNTs did not have a very pronounced effect on the densification of YSZ and no appreciable improvement in the hardness was observed. This was likely the result of MWCNT agglomeration in the ceramic matrix. In contrast, the SWCNTs had a significant effect on the hardness of the ceramic composite with ~ 71% increase in hardness from 0 to 1wt% SWCNT addition. However, SWCNTs were also seen to hinder densification. The thermal conductivity of the SWCNT – YSZ ceramic composites was seen to be a function of the concentration of the SWCNTs in the composite.

Preface

The Results and Discussions presented in Chapter 4 of this thesis, have been published in the following publications:

- Abhinav Karanam, Lukas Bichler and Randy Fong “On The Densification Behavior Of (0.2, 0.5 And 1wt %) CNT-YSZ Ceramic Composites Processed via Spark Plasma Sintering”, Metallurgical and Materials Transactions – B; doi: 10.1007/s11663-015-0317-y.
- Abhinav Karanam, Vishank Kumar and Lukas Bichler, “Effect of SPS Process Parameters on the Densification Behaviour of Ytria Stabilized Zirconia”, SAE International Journal of Materials and Manufacturing; doi: 10.4271 / 2014-01-0835; Vol. 07, pp. 406-410.
- Abhinav Karanam and Lukas Bichler, “Evaluation of Mechanical and Thermal Properties of Spark Plasma Sintered SWCNT-YSZ Ceramic Composites”, (In progress).
- Abhinav Karanam and Lukas Bichler, “Enhancement of Mechanical Properties of Single Walled and Multi Walled CNT Reinforced YSZ Ceramic Composites”, (In progress).

Sections 4.1 and 4.2.1 of Chapter 4 have been presented at the following international conferences:

1. **September 28 – October 1 2014**

Vancouver, BC, CANADA

Abhinav Karanam and Lukas Bichler, “Development of (0.2, 0.5, and 1 wt %) ”

CNT+YSZ Ceramic Composites via Spark Plasma Sintering” 53rd Annual Conference of Metallurgists 2014.

2. June 16 – 19, 2014

Orlando, FL, USA

Abhinav Karanam and Lukas Bichler, “Effect of Single Walled- CNTs on the Fabrication and Properties of Spark Plasma Sintered 8 mol% YSZ Nano-Composites” AeroMat Conference and Exposition.

3. April 8 – 10, 2014

Detroit, MI, USA

Abhinav Karanam and Lukas Bichler, “Effect of SPS Process Parameters on the Densification Behaviour of Yttria Stabilized Zirconia” SAE World Congress and Exhibition.

The contributions of the authors and the collaborators of the above mentioned publications and presentations are as follows:

Fabrication of the ceramic specimens was performed by A. Karanam at The University of British Columbia. The Nano Indentation experiments described in the thesis were performed at the Indian Institute of Technology Madras, India, under the supervision of Dr. B. S. Murty by the author of this thesis. The thermal property measurements were carried out at Netzsch, Boston, MA, USA and the raw data was analyzed by the author of this thesis. The XRD experiments were performed by Ms. A. Lam at the University of British Columbia Vancouver and analyzed by A. Karanam. Manuscripts were compiled and written by A. Karanam, with editing and technical corrections by Dr. L. Bichler at The University of British Columbia Okanagan.

Table of Contents

Abstract.....	ii
Preface.....	iii
Table of Contents.....	v
List of Tables.....	ix
List of Figures.....	x
List of Abbreviations.....	xvii
Acknowledgements.....	xviii
Dedication.....	xix
Chapter 1: INTRODUCTION.....	1
Chapter 2: LITERATURE REVIEW.....	5
2.1 Zirconia.....	5
2.1.1 Transformation Toughening of Zirconia.....	7
2.1.2 Thermodynamics of Phase Transformations.....	7
2.2 Yttria Stabilized Zirconia.....	9
2.3 Fabrication of YSZ Ceramic Composites.....	10
2.4 Spark Plasma Sintering.....	16
2.5 Spark Plasma Sintering of YSZ.....	21
2.6 Carbon Nanotubes.....	24

2.6.1	Fabrication and Characterization of CNT-Ceramic Composites.....	25
2.6.2	Fabrication and Characterization of CNT-YSZ Ceramic Composites	27
Chapter 3: EXPERIMENTAL PROCEDURE		33
3.1	Precursor Powders	33
3.2	Powder Blending.....	35
3.3	Spark Plasma Sintering of Powder Blends	36
3.3.1	Spark Plasma Sintering of Pure 8 mol% YSZ Ceramics.....	39
3.3.2	SW/MWCNT-YSZ Ceramic Composites	41
3.4	Sample Polishing and Preparation	42
3.5	Specific Gravity Measurement	42
3.6	Hardness Measurement.....	42
3.7	Microstructure Characterization	43
3.8	Thermal Analysis	43
3.9	Nanoindentation Testing.....	44
3.10	X-Ray Diffraction	44
Chapter 4: RESULTS AND DISCUSSIONS		45
4.1	Characterization of YSZ Precursor Powder.....	45
4.2	Densification of 8mol% YSZ.....	47
4.2.1	Densification of Samples Sintered at 1300°C (Group 1).....	51
4.2.2	Densification of Samples Sintered Under 50MPa Pressure (Group 2)	62

4.3	Processing and Characterization of CNT-YSZ Ceramic Composites	72
4.3.1	Synthesis and Densification Behaviour of the SWCNT-YSZ Ceramic Composites	72
4.3.1.1	Effect of SWCNTs on the Densification Behavior of the Ceramic Composites.....	74
4.3.1.2	Microhardness of the SWCNT-YSZ Ceramic Composites.....	87
4.3.1.3	Nano Indentation of the SWCNT-YSZ Ceramic Composites.....	89
4.3.1.4	Thermal Properties of the SWCNT-YSZ Ceramic Composites.....	95
4.3.2	Processing and Preliminary Characterization of MWCNT-YSZ Ceramic Composites.....	100
4.3.2.1	Effect of MWCNTs on the Densification Behavior of the Ceramic Composites.....	102
4.3.2.2	Hardness Measurement of the MWCNT-YSZ Ceramic Composites	109
Chapter 5: CONCLUSIONS.....		112
5.1	Densification of 8mol% YSZ.....	112
5.2	Processing and Characterization of SWCNT-YSZ Ceramic Composites	112
5.3	Processing and Characterization of MWCNT-YSZ Ceramic Composites	114
Chapter 6: RECOMMENDATIONS FOR FUTURE WORK.....		115
6.1	Densification of 8mol% YSZ by SPS.....	115
6.2	Processing and Characterization of As-Sintered SWCNT-YSZ Ceramic Composites	116

6.3	Processing and Characterization of As-Sintered MWCNT-YSZ	
	Ceramic Composites	116
	Bibliography	117
	Appendix A: Grain Size Distribution Curves	129

List of Tables

Table 2.1: Sintering conditions [55]	28
Table 3.1: Composition of the YSZ powder	33
Table 3.2: SPS sintering parameters for pure YSZ.....	40
Table 4.1: Composition (wt. %) of YSZ powders by X-EDS	47
Table 4.2: Densities of the as-sintered YSZ composites	48
Table 4.3: Process parameters of the YSZ samples considered.....	51
Table 4.4: Relative density of Group 1 YSZ samples (w.r.t. theoretical density of YSZ) during SPS cycle.....	53
Table 4.5: X-EDS spectrum values of the glassy phase from Figure 4.9	58
Table 4.6: Relative density of Group 2 YSZ samples (w.r.t. theoretical density of YSZ) during SPS	64
Table 4.7: Relative density of SWCNT-YSZ composites (w.r.t. theoretical density of YSZ) during SPS cycles	76
Table 4.8: Comparison of the observed Young's modulus results with literature.....	95
Table 4.9: Composition of the second phase network as obtained from the X-EDS analysis	109

List of Figures

Figure 1.1: Flowchart summarizing the work done in this thesis project.....	4
Figure 2.1: YSZ phase diagram [17].....	6
Figure 2.2: Structure of YSZ [26].....	10
Figure 2.3: Linear compaction of samples during SPS and conventional sintering processes [31].....	12
Figure 2.4: a) Density and b) Grain size as a function of temperature for SPS and HP samples [31].....	13
Figure 2.5: SEM micrographs of as-sintered samples: a) SPS-1200-50-10; b) SPS-1200-50-10; c) SPS-1100-110-8; d) SPS-1300-70-5; e) HP-1250-25-0; f) HP-1250-25-3 and g) Conventionally sintered-1500-0-12 [31].	14
Figure 2.6: SEM images of the surfaces of: a) SPS sample and b) Conventionally sintered sample [32].....	15
Figure 2.7: a) Grain size and b) Relative density measurements for SPS and HP operations [33].	16
Figure 2.8: Schematic of the spark plasma sintering machine [30].....	17
Figure 2.9: Pulse current passing through the powder particles in an SPS process [30].....	18
Figure 2.10: Stages of necking during SPS [30].....	19
Figure 2.11: Sintering stages during SPS sintering: a) Initial neck formation; b) Expansion of necks and c) Plastic deformation and elimination of pores [30].....	20

Figure 2.12: Relative density and ionic conductivity as a function of:	
a) Sintering cycles and b) Sintering pressure [37].	21
Figure 2.13: Relative densities of the as-sintered discs as a function of:	
a) Sintering temperature and b) Hold time [41].	23
Figure 2.14: a) Molecular structure of a section of a CNT where each node here	
represents a carbon atom and the lines represents the bonds	
between them; b) Hexagonal structure of one graphite layer [42].	24
Figure 2.15: CNTs seen in the SiC matrix after hot pressing at two different sites:	
a) Site 1 and b) Site 2 [51].	26
Figure 2.16: a) Relative density and b) Grain size measurements of	
CNT-YSZ ceramic composites [54].	28
Figure 2.17: Three point bed test results for the MWCNT-YSZ ceramic composites	
sintered at two different sintering temperatures [57].	31
Figure 3.1: SEM micrographs of: a) YSZ; b) SWCNT; c) MWCNTs.	34
Figure 3.2: Impurities seen in the SWCNTs at: a) 10,000x and	
b) 200,000x magnifications.	35
Figure 3.3: Photograph of the SPS sintering machine (LLC 10-3 SPS).	37
Figure 3.4: Photographs of: a) ISOcarb sintering die and b) Sintering chamber.	38
Figure 3.5: Photographs of the as-sintered YSZ samples: a) Sample Y1;	
b) Sample Y2; c) Sample Y5 and d) Sample Y6.	41
Figure 4.1: SEM images of the YSZ powder at different magnifications showing the	
powder particle structure: a) 10,000x magnification; b) 100,000x	
magnification; c) 200,000x magnification and d) 500,000x magnification.	46

Figure 4.2: Photographs of the as-sintered YSZ samples seen to disintegrate post ejection: a) Sample Y2; b) Sample Y5 and c) Sample Y8.	49
Figure 4.3: Discoloration of the fracture planes seen in the as-sintered YSZ discs: a) Sample 2 and b) Sample 4.	50
Figure 4.4: Densification curves of the YSZ samples sintered at 1300°C (Group 1): a) Instantaneous Density vs Time; b) Instantaneous Density vs Temperature; c) Densification rate vs Time.	52
Figure 4.5: XRD analysis of the as-sintered Group 1 YSZ samples, sintered at 1300°C (T: Tetragonal, M: Monoclinic).....	54
Figure 4.6: Thickness of the as-sintered YSZ discs (Group 1).....	55
Figure 4.7: SEM images of the polished surfaces of the as-sintered Group 1 YSZ discs: a) Sample 1; b) Sample 2 and c) Sample 3.	56
Figure 4.8: SEM images of the glassy phase present along the grain boundaries of the as-sintered Group 1 YSZ discs: a) Sample 1; b) Sample 2 and c) Sample 3.....	57
Figure 4.9: X-EDS spectrum sites on the glassy phase of Sample 3.	58
Figure 4.10: Glassy phase on the grain boundaries with crack propagating through the glassy layer. Sample 1 at: a) 200x and b) 1,000x magnifications; Sample 3 at: c) 10,000x and d) 20,000x magnification.	60
Figure 4.11: SEM images of the fracture surfaces of the heat treated samples (Group 1): a) Sample 1; b) Sample 2; c) Sample 3.....	61
Figure 4.12: Grain size measurements of the samples sintered at 1300°C (Group 1).	62

Figure 4.13: Densification curves of the YSZ samples sintered under 50MPa pressure (Group 2): a) Instantaneous Density vs Time; b) Instantaneous Density vs Temperature; c) Densification rate vs Time.	64
Figure 4.14: Density of the samples sintered under 50MPa pressure (Group 2).....	65
Figure 4.15: Thickness of as-sintered YSZ discs (Group 2).....	66
Figure 4.16: XRD analysis of the as-sintered Group 2 YSZ samples, sintered under 50MPa pressure (T: Tetragonal, M: Monoclinic).....	67
Figure 4.17: Grain size measurements of the samples sintered under 50MPa pressure (Group 2).....	68
Figure 4.18: SEM images of the fracture surface of the samples of Group 2: a) Sample 4; b) Sample 5 and c) Sample 6.	69
Figure 4.19: a) Smaller grains seen along the grain boundaries of larger grains (indicated by arrows) and b) Initiation of the glassy phase along the grain boundaries (encircled) in sample 5.	70
Figure 4.20: Glassy phase covering the grains of sample 6, and crack propagation seen along the glassy phase at four different sites, a); b); c); and d).	71
Figure 4.21: SWCNTs seen along the grain boundaries: a) 0.2wt% SWCNT-YSZ; b) 0.5wt% SWCNT-YSZ and c) 1wt% SWCNT-YSZ.....	73
Figure 4.22: a) Instantaneous density vs Time; b) Instantaneous density vs Temperature; c) Densification rate vs Time and d) Sintering current vs Time plots of the SWCNT-YSZ ceramic composites.....	75
Figure 4.23: SWCNTs as seen along the grain boundaries of the as-sintered SWCNT-YSZ composites: a) 0.2wt% SWCNT-YSZ; b) 0.5wt% SWCNT-YSZ.	78

Figure 4.24: SWCNT agglomeration seen in the 1wt%SWCNT-YSZ composite:	
a) Site 1 and b) Site 2.....	79
Figure 4.25: Height of the as-sintered SWCNT-YSZ composites.....	80
Figure 4.26: SEM images of the fracture surfaces of SWCNT-YSZ ceramic composites:	
a) YSZ; b) 0.2wt% SWCNT-YSZ; c) 0.5wt% SWCNT-YSZ and	
d) 1wt% SWCNT-YSZ.....	82
Figure 4.27: Deviations measured in the grain sizes of the as-sintered composites.....	83
Figure 4.28: SEM images of 1.0 wt% SWCNT-YSZ composite showing:	
a) Faceted grains in the vicinity of the SWCNT bundles and	
b) Grains in regions free of SWCNTs.....	84
Figure 4.29: a) Specific gravity and b) Grain size measurements of the as-sintered	
SWCNT-YSZ ceramic composites.....	85
Figure 4.30: Internal structures in SWCNT-YSZ ceramic composites: a) YSZ;	
b) 0.2wt% SWCNT-YSZ; c) 0.5wt% SWCNT-YSZ and	
d) 1wt% SWCNT-YSZ.....	86
Figure 4.31: Hardness and grain size of the SWCNT-YSZ ceramic composites.	88
Figure 4.32: SWCNTs seen bridging grains in: a) 0.5wt%SWCNT-YSZ and	
b) 1wt% SWCNT-YSZ composites.	89
Figure 4.33: Nano Indentation hardness of the SWCNT-YSZ composites.....	90
Figure 4.34: Comparison of the microhardness and the NI hardness of the	
SWCNT-YSZ ceramic composites.....	91
Figure 4.35: Load-Displacement curve for the SWCNT-YSZ ceramic composites.	92
Figure 4.36: Plastic deformation measured in the composites after the indentation.	93

Figure 4.37: Young's modulus of the SWCNT-YSZ ceramic composites.....	94
Figure 4.38: Specific heat of the SWCNT-YSZ ceramic composites measured at three different temperatures.	96
Figure 4.39: Thermal conductivity of the SWCNT-YSZ ceramic composites.....	97
Figure 4.40: Thermal diffusivity of the SWCNT-YSZ ceramic composites.....	99
Figure 4.41: SEM images of MWCNT-YSZ powder blends: a) 0.2wt% MWCNT-YSZ; b) 0.5wt% MWCNT-YSZ and c) 1wt% MWCNT-YSZ.	101
Figure 4.42: Densification behavior of the MWCNT-YSZ ceramic composites: a) Instantaneous density vs Time; b) Instantaneous density vs Temperature; c) Densification rate vs Time and d) Current vs Time plots.	102
Figure 4.43: Specific gravity measurements of the MWCNT-YSZ ceramic composites.....	103
Figure 4.44: SEM images on the fracture surfaces of: a) YSZ; b) 0.2wt% MWCNT- YSZ; c) 0.5wt% MWCNT-YSZ and d) 1wt% MWCNT-YSZ ceramic composites sintered at 1300°C for 3min.	104
Figure 4.45: Grain size of the as-sintered MWCNT-YSZ ceramic composites.	105
Figure 4.46: Fusion of grains as seen in: a) 0.2wt% MWCNT-YSZ and b) 1wt% MWCNT-YSZ ceramic composites.....	106
Figure 4.47: Agglomeration of the MWCNTs in: a) 0.2wt% MWCNT-YSZ and b) 0.5wt% MWCNT-YSZ ceramic composites.	107
Figure 4.48: A secondary phase seen along the grain boundaries of the 1wt% MWCNT-YSZ composite at: a) 5000x and b) 15000x magnification.	108
Figure 4.49: A secondary phase network in 1wt% MWCNT-YSZ composite.....	108
Figure 4.50: Hardness of the MWCNT-YSZ ceramic composites.	110

Figure 4.51: a) MWCNTs seen along the grain boundaries of 0.2wt%
MWCNT-YSZ composite and b) Grain boundary pinning
effect seen in 0.5wt% MWCNT-YSZ composite. 111

Figure A.1: Grain size distribution for samples of Group 1.....129

Figure A.2: Grain size distribution for samples of Group 2.....130

Figure A.3: Grain size distribution of SWCNT-YSZ ceramic composites.....130

List of Abbreviations

BSE	Back Scattered Electron
CNT	Carbon Nanotubes
CVD	Chemical Vapor Deposition
HIP	Hot Isostatic Pressing
HP	Hot Pressing
MWCNT	Multi-Walled Carbon Nanotubes
NI	Nano Indentation
PM	Powder Metallurgy
SE	Secondary Electron
SEM	Scanning Electron Microscope
SHS	Self-propagating High Temperature Synthesis
SPS	Spark Plasma Sintering
SWCNT	Single-Walled Carbon Nanotubes
TBC	Thermal Barrier Coating
X-EDS	X-Ray Electron Dispersive Spectroscopy
XRD	X-Ray Diffraction
YSZ	Yttria Stabilized Zirconia

Acknowledgements

Firstly I would like to acknowledge my supervisor Dr. Lukas Bichler for supporting me throughout the course of this program. Without his help and continuous motivation this thesis would have been impossible. I would like to sincerely thank him for his relentless efforts and guidance to make my efforts fruitful.

I am deeply grateful to Dr. B.S. Murty for introducing me to the field of Materials Science and for accommodating me in his lab during my stay in Chennai, India. I am indebted to him for mentoring me both in my professional and personal life.

I would like to take this opportunity to thank David Arkininstall for assisting me with all the SEM analysis and also, bearing with my last minute requests for slots.

I sincerely thank N.S.Karthikselva and S.L.Pramod from IIT Madras, India for immensely helping me with my Nano Indentation experiments.

I wish to thank my colleagues, Mathew Smith, Christopher Verdon, Audrey Siebert-Timmer, Karen Robles and William Threlfall for making my work in the lab an enjoyable experience.

I am happy to have made wonderful friends in Canada, Tausif Khan and Ashish De who made my stay in Canada a memorable experience. I would also like to appreciate their patience while dealing with my weak moments.

The continuous motivation and long-distance phone calls from my best friends, Ajay Singh and Siddharth Yadav have contribute a great deal to my success in Canada.

The saying, 'Behind every successful man is a woman' is so true in my life, thanks to, Nivedita Mahesh.

Finally, I would like to thank my parents for their constant support, unconditional love and immeasurable trust in me. Without them I would not be who I am today.

I dedicate this thesis to the three pillars of support in my life:

Dr. Lukas Bichler & Dr. B.S. Murty;

My loving parents, P. Neeraja & Dr. K. U. M. Rao;

My beloved late grandfather, Thathi (P. Venkateshwara Rao).

Chapter 1: INTRODUCTION

Ceramics are non-metallic inorganic solids usually consisting of metallic and non-metallic elements. In general, ceramics have high hardness, high thermal and electrical resistivity and a high corrosion resistance. Presently, there is a great interest in using ceramics in aircraft and combustion engines in order to enable these engines to operate at higher temperatures, thus increasing their thermodynamic efficiency and reduce pollution [1].

Pollution from automobiles can be reduced via the use of oxygen sensors, which control exhaust pollution through engine management [2]. Yttria Stabilized Zirconia (YSZ) has been recognized as a candidate ceramic suitable for oxygen sensors [3].

A recent study published by the Federal Aviation Association suggests that with the two fold increase in air traffic in the next two decades, higher efficiency jet engines will be required [4]. To enhance efficiency and reduce pollution, the jet engines must operate at working temperatures, which often exceed the melting point of the engine component materials. In such cases, ceramic thermal barrier coatings (TBCs) are used; with YSZ being one of the most widely used ceramic materials [5]. Thus far, YSZ TBCs were seen to increase the efficiency of aero engines by 10 - 15% [6].

Yttria Stabilized Zirconia is an advanced ceramic with high hardness, low coefficient of friction, high Young's modulus, high chemical inertness, high corrosion resistance, high thermal resistance, high thermal shock resistance and a high ionic conductivity at elevated temperatures [7]. However, YSZ is very brittle and thus needs to be reinforced with dopants to further improve its mechanical properties. For example, WO_3 and MnO_2 additions have shown to improve the hardness, indentation fracture toughness [8] and compressive strength

[9], respectively. Similarly, addition of Carbon Nanotubes (CNTs) has been suggested to possibly enhance the mechanical properties of YSZ.

Carbon Nanotubes are allotropes of carbon with a cylindrical nano-structure. Based on the number of cylindrical layers, CNTs are classified as Single-Walled CNTs (SWCNT) and Multi-Walled CNTs (MWCNTs). CNTs are constructed to have a very high aspect ratio (length:diameter) of about 132,000,000:1 [10].

Bulk CNT-YSZ composites have been recently fabricated using powder metallurgy process called Spark Plasma Sintering (SPS), where the composite powders are compacted to high density by the simultaneous application of load and temperature. The advantage of using SPS over other sintering processes is its superior control of the grain size and the ensuing mechanical strength [11].

The aim of this work was to study the fabrication of YSZ ceramic by Spark Plasma Sintering method and study the effect of varying sintering parameters on the densification behaviour, density and microstructure of the samples. Further, novel SWCNT-YSZ and MWCNT-YSZ ceramic composites were also prepared and their densification behaviour, mechanical and thermal properties were examined.

Thus, the objectives of this thesis were classified into the following three categories:

1. Fabricate pure YSZ samples by SPS and study the effect of varying sintering parameters on the densification behavior and microstructure of the as-sintered samples.
2. Fabricate SWCNT-YSZ ceramic composites by SPS and study the effect of the SWCNTs on the densification behavior, mechanical properties (hardness and nano-

- indentation) and the thermal properties (specific heat, thermal conductivity and thermal diffusivity) of the ceramic composites.
3. Fabricate MWCNT-YSZ ceramic composites by SPS and study the effect of the MWCNTs on the densification behavior of the ceramic composites and compare the mechanical properties of the MWCNT-YSZ ceramic composites with that of the SWCNT-YSZ ceramic composites.

Figure 1.1 shows the scope of the experiments performed in this research.

The thesis document has been structured as follows:

Chapter 2 summarizes available literature on Zirconia - based ceramics, and existing fabrication processes.

Chapter 3 summarizes the different experiments performed in this thesis

Chapter 4 provides an in-depth discussion of the results obtained from the experiments performed.

Chapter 5 summarizes the conclusions of the work presented in this thesis, and

Chapter 6 provides suggestions for the future work.

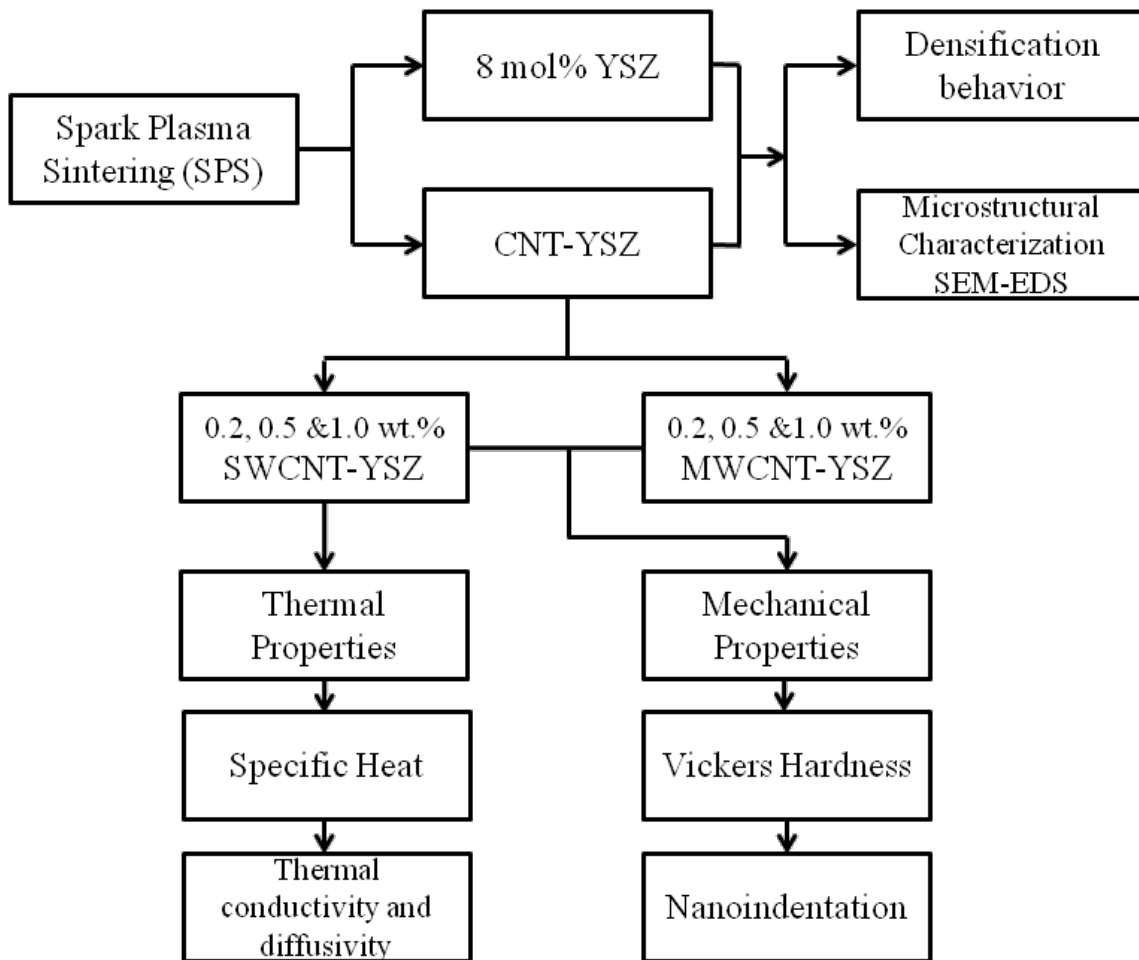


Figure 1.1: Flowchart summarizing the work done in this thesis project.

Chapter 2: LITERATURE REVIEW

This chapter provides an overview of previous studies conducted on zirconia-based ceramic composites, their properties and fabrication methods.

2.1 Zirconia

Zirconia (ZrO_2) is a polycrystalline oxide of the transition metal Zirconium. ZrO_2 has high hardness, low coefficient of friction, high elastic modulus, chemical inertness and when compared to other ceramics, it has one of the lowest thermal conductivities. These properties make it an attractive material for use as a thermal insulator at elevated temperatures [7]. Zirconia undergoes two phase transformations at elevated temperature, as shown in the phase diagram in Figure 2.1. Zirconia exhibits a monoclinic structure from room temperature upto 1170°C [6] with a density of 5.56g/cm^3 [12]. Above this temperature, the monoclinic zirconia transforms into a denser tetragonal zirconia, which is accompanied by a $\sim 5\%$ decrease in volume [13] and the density increases to 6.10 g/cm^3 [12]. With further heating above 2370°C , tetragonal zirconia transforms into a denser cubic zirconia [13] with a cubic calcium fluoride lattice structure [14] and a density of $\sim 6.27\text{ g/cm}^3$ [12]. These phase transformations in Zirconia upon heating can also be observed during cooling of the ceramic; however the tetragonal to monoclinic phase transformation is reported to be accompanied by a volumetric increase of $\sim 3\text{-}4\%$ [13]. Bansal *et al.* [15] studied the kinetics of phase transformations in Zirconia and observed a large hysteresis. During the monoclinic to tetragonal phase transformation at $\sim 1170^\circ\text{C}$, the tetragonal phase grows within the monoclinic matrix. As a result, the tetragonal phase due to its lower volume experiences tension [15]. In contrast, during the cooling cycle phase transformation ($\sim 950 - 850^\circ\text{C}$), the monoclinic phase grows

inside of the tetragonal matrix which subsequently experiences compression [15]. Bailey [16] reported that the tetragonal to monoclinic phase transformation was martensitic in nature and also observed the hysteresis behavior during the transformation. Bansal *et al.* [15] reported that during the cooling cycle, at $\sim 950^\circ\text{C}$, platelets formed in the zirconia ceramic. The growth of these platelets was considered to be diffusionless, since at constant temperature these platelets were stable, thus confirming the athermal nature of the transformation. They also suggested that the formation of these platelets was similar to the martensitic phase transformation [15].

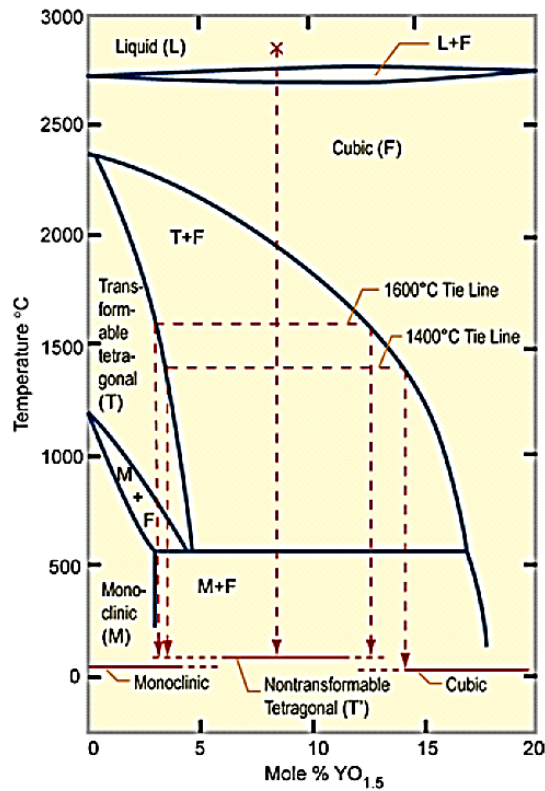


Figure 2.1: YSZ phase diagram [17].

2.1.1 Transformation Toughening of Zirconia

The martensitic tetragonal to monoclinic phase transformation in the zirconia ceramics can be induced by two methods: 1) by cooling and 2) by external loading under isothermal conditions [18]. According to Basu [19], thermally induced transformations control the amount of the tetragonal phase that can be retained, while stress induced transformation enhances the toughness of the ceramic. It was observed that martensitic phase transformation in zirconia ceramics occurs at a high speed and involves plastic deformation of the transformed volume, as the tensile stress region around a metastable tetragonal zirconia phase transforms it into a stable monoclinic phase [20]. This transformation is accompanied by a volume expansion compressing the plastically deformed region, which reduces the effect of any stress concentrations or micro cracks resulting in increased toughness of the ceramic [20].

2.1.2 Thermodynamics of Phase Transformations

The total change in the Gibbs free energy associated with any phase change can be described by Equation 2-1, where ΔG is the total change in the free energy of a solid particle, V is the volume of the solid material, A is the surface area of the material, ΔG_v is the volumetric free energy change associated with the phase change and $\Delta\gamma$ is the change in the surface free energy of the material [21]:

$$\Delta G = V\Delta G_v + A\Delta\gamma \quad \text{Equation 2-1}$$

The change in the volumetric free energy, during a tetragonal to monoclinic phase transformation in ZrO_2 ceramics can be assumed to be the sum of the chemical free energy change associated with the chemical changes that occur during the phase transformation and

the strain free energy change associated with the shear and dilatational energy changes during the phase transformation [22]. Thus, Equation 2-1 can be re-written as [22] :

$$\Delta G_{t \rightarrow m} = V(\Delta G_{chemical} + \Delta G_{strain}) + A\Delta\gamma \quad \text{Equation 2-2}$$

The equilibrium temperature between the tetragonal and the monoclinic phases, T_o , is when the $\Delta G_{chemical} = 0$. But the temperature when this phase transformation starts, M_s , is given when $\Delta G_{t \rightarrow m} = 0$.

The martensitic transformation is considered to be stress induced [16]. Considering this phenomenon, Jin [20] defined a critical transformation stress, given by Equation 2-3:

$$\sigma_c = \frac{(-\Delta G_{chemical} + \Delta G_{strain} + \frac{A}{V}\Delta\gamma)}{\varepsilon^t} \quad \text{Equation 2-3}$$

In the above equation, ε^t is the resultant dilatational strain associated with the transformation. Jin [20] defined the sum of the changes in the surface free energy and the strain energy as $\Delta G_{barrier}$. Therefore the above equation can be rewritten as:

$$\sigma_c = \frac{(-\Delta G_{chemical} + \Delta G_{barrier})}{\varepsilon^t} \quad \text{Equation 2-4}$$

From Equation 2-4, it was observed that the total free energy change can be manipulated by the addition of dopants in order to change the chemical free energy [20] and stabilize a desired phase.

Stabilization of zirconia can be achieved via doping with oxides. Depending on the amount of the oxide added, different phases of ZrO_2 can be stabilized to room temperature [23]. The most commonly used stabilizers for ZrO_2 are MgO, CaO, Y_2O_3 and CeO [24].

2.2 Yttria Stabilized Zirconia

Yttria Stabilized Zirconia (YSZ) is a zirconia based oxide, where yttria (Y_2O_3) is added to zirconia to structurally stabilize the tetragonal or the cubic phase at room temperature [25]. Along with structurally stabilizing the zirconia ceramic, the addition of yttria to zirconia maintains the charge neutrality by generating oxygen vacancies in the ceramic [25]. The stabilization is achieved by replacing the Zr^{4+} ions from the zirconia cubic structure with bigger Y^{3+} ions resulting in a Cubic – Fluorite structure, as shown in Figure 2.2 [26]. Three O^{2-} ions from Y_2O_3 replace four O^{2-} ions in ZrO_2 , thus creating a vacancy, which enables the YSZ to conduct O^{2-} ions. This conduction of ions is controlled by the vacancy mobility, which increases with the increase in temperature. Therefore, YSZ has good ionic conductivity at elevated temperatures, which also makes it a good electrolyte for Solid Oxide Fuel Cells [27]. The ionic conductivity of YSZ also increases with the increase in the concentration of dopants. In the case of YSZ, the maximum ionic conductivity has been obtained at 8 mol% Y_2O_3 concentrations [25].

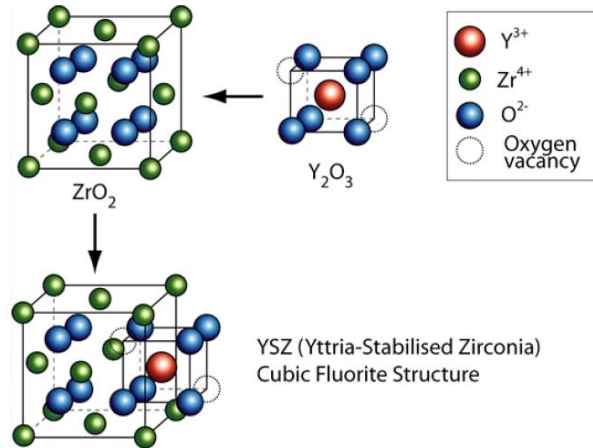


Figure 2.2: Structure of YSZ [26].

Further, the addition of Yttria to Zirconia is also known to improve the mechanical, chemical and electrical properties of the ceramic [17].

2.3 Fabrication of YSZ Ceramic Composites

Currently, there are several ways of fabricating YSZ coatings and bulk components. Plasma spraying of YSZ on metallic substrates has been used for the fabrication of YSZ thermal barrier coatings [28]. However, plasma spraying results in a large number of detrimental pores and cracks that negatively affect the mechanical and thermal properties of the ceramic [29].

A common approach for the fabrication of bulk YSZ components is by sintering. Hot Isostatic Pressing (HIP) and Hot Pressing (HP) processes have been used to fabricate YSZ components, but the major limitation of these techniques is their complicated setup. An alternative powder metallurgy (PM) technique is Spark Plasma Sintering (SPS), which enables pressure assisted rapid sintering and sinter-bonding of powders at low temperatures [30].

Dahl *et al.* [31] studied the densification behaviour and the properties of nanocrystalline 8mol% YSZ powders sintered by conventional sintering, hot pressing and spark plasma sintering. For the SPS experiments, sintering temperature and pressure was varied from 1100°C to 1300°C and 50 to 110MPa, respectively, with the dwell time ranging from 0 to 10 minutes. The heating rate was maintained at 100°C/min and a cooling rate of >360°C/min was imposed. For performing HP, the uncompact powders were loaded in graphite dies and initially heated to 600°C at the rate of 600°C/hr. At this temperature, a uniaxial load of 25MPa was applied and then the powders were heated to the sintering temperatures ranging from 1150°C to 1300°C at the rate of 300°C/hr. The samples were dwelled at these conditions for 0 to 6hrs and cooled at a rate of 600°C/hr. The green compacts for conventional sintering were prepared by uniaxial compaction with a load of 64MPa, which was followed by cold isostatic pressing with a load of 20MPa. This provided the samples a green compact density of ~43%. These green compacts were sintered at the following conditions: (a) 1150°C to 1300°C for 1 hour with a heating rate of 300°C/hr and (b) 1500°C for 12 hours with a heating and a cooling rate of 200°C/hr [31].

The experiments revealed that conventional sintering and hot pressing processes were more time consuming as compared to the SPS process. Densification during the SPS was higher than the conventional sintering process, with the SPS samples reaching >96% density within minutes, whereas conventionally sintered samples required hours to attain their final densities, as seen in Figure 2.3 [31].

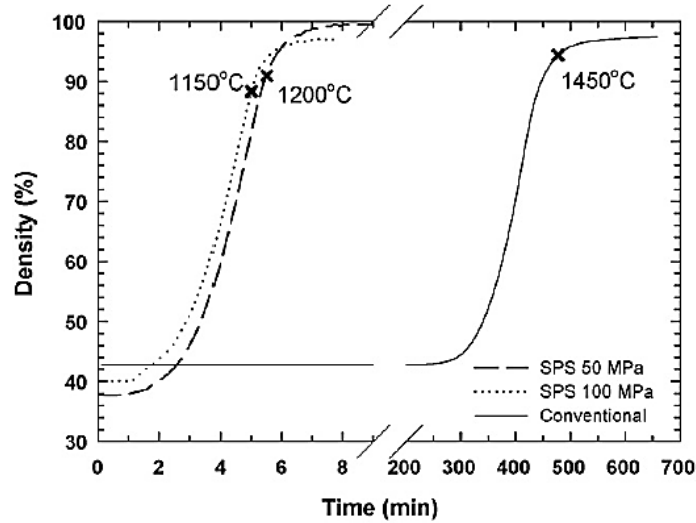


Figure 2.3: Linear compaction of samples during SPS and conventional sintering processes [31].

Higher relative density of the as-sintered SPS samples was seen at lower temperatures as compared to the samples sintered by HP and conventional sintering. From Figure 2.4a [31], it was seen that at 1150°C, the SPS sintered samples had a relative density of 96%, whereas HP samples had a density of ~79% with conventionally sintered samples having a density of only ~54% [31].

The microstructure analysis of the samples revealed that SPS and HP methods were able to control the grain growth during the sintering process, as seen in Figure 2.4b. The samples fabricated by conventional sintering exhibited larger grains with enclosed pores whereas the SPS process yielded homogenous microstructures with a uniform grain size distribution, as seen in Figure 2.5. For all methods, the grain size was seen to increase with an increase in dwell time and sintering temperature. The grain growth with increasing dwell time during HP was comparable to that of SPS [31].

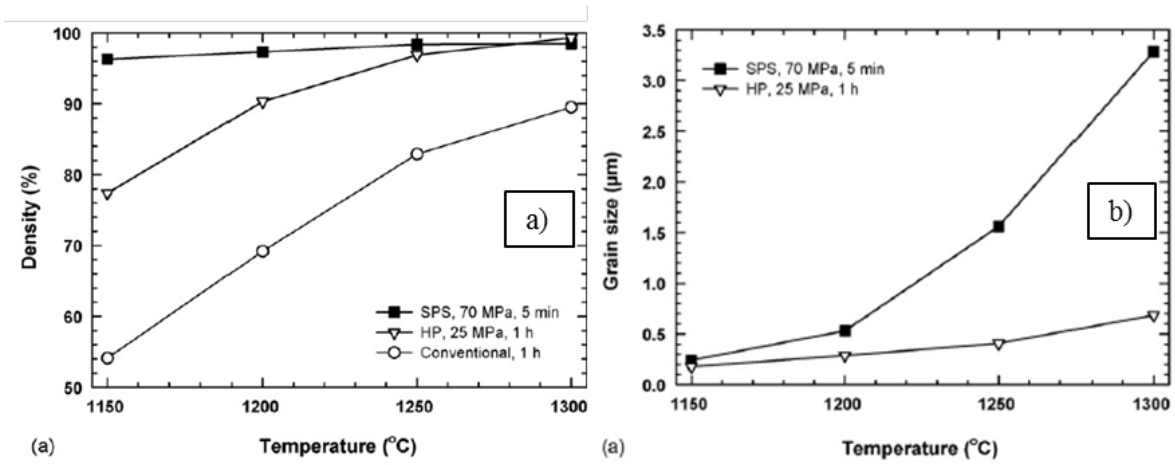


Figure 2.4: a) Density and b) Grain size as a function of temperature for SPS and HP samples [31].

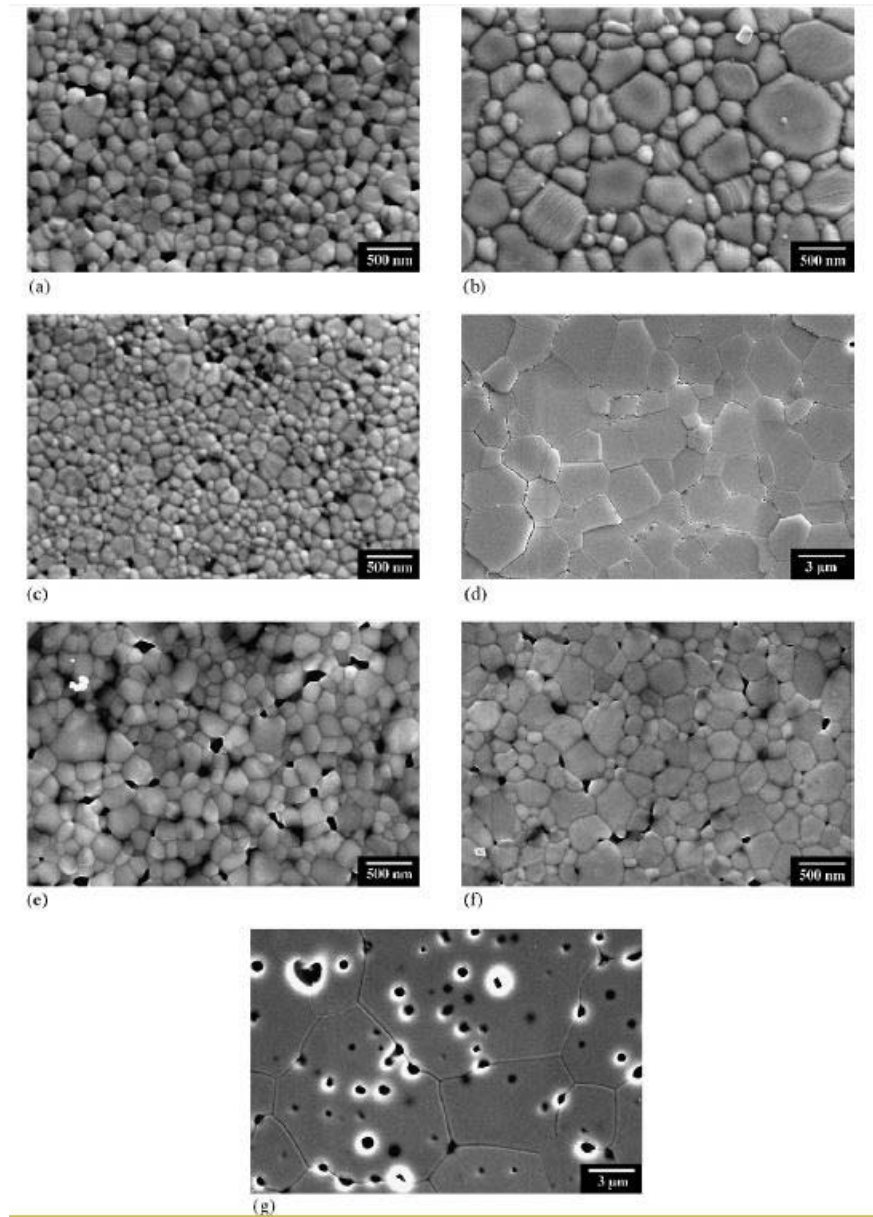


Figure 2.5: SEM micrographs of as-sintered samples: a) SPS-1200-50-10; b) SPS-1200-50-10; c) SPS-1100-110-8; d) SPS-1300-70-5; e) HP-1250-25-0; f) HP-1250-25-3 and g) Conventionally sintered-1500-0-12 [31].

Bangchao *et al.* [32] compared SPS sintered and conventionally sintered commercially available 8mol% YSZ ceramics with powder particle size starting at 0.1 μ m. The SPS samples were sintered at a sintering temperature of 1350 $^{\circ}$ C with a load of 28MPa for 10

minutes and cooled at a rate of 160°C/min. For the conventionally sintered samples, the powders were compacted with a load of 140MPa and then sintered in an electric furnace at 1450°C for 4hrs. The relative density of the SPS as-sintered discs was 99%, whereas for the conventionally sintered sample the density was 97%. The microstructural analysis of the samples revealed that the samples fabricated by SPS had smaller grains with an average grain size of 0.8µm, while the conventionally sintered samples had grains with an average grain size of 3µm, as seen in Figure 2.6 [32].

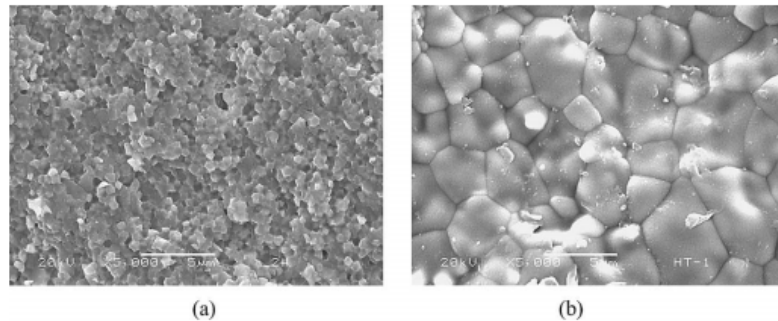


Figure 2.6: SEM images of the surfaces of: a) SPS sample and b) Conventionally sintered sample [32].

Granger *et al.* [33] performed spark plasma sintering and hot pressing of YSZ with ~5.5wt.% Y₂O₃ at sintering temperatures ranging from 950-1200°C. The grain size and relative density of the as-sintered products was comparable, as seen in Figure 2.7 [33].

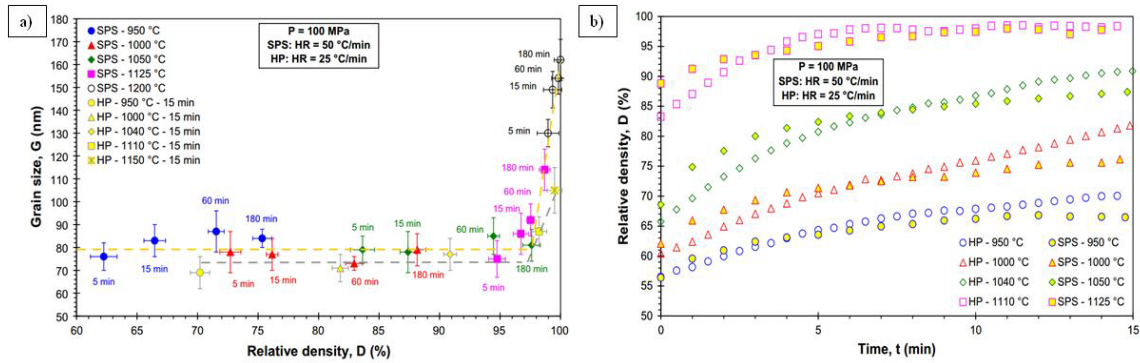


Figure 2.7: a) Grain size and b) Relative density measurements for SPS and HP operations [33].

The relative density results in Figure 2.7a suggest that for a given temperature, the density of samples prepared by SPS and the HP process were similar. For sintering temperatures ranging from 950°C to 1050°C, the final density of the HP samples was slightly higher than that of the SPS samples, as seen in Figure 2.7b [33].

2.4 Spark Plasma Sintering

The spark plasma sintering process is based on fusion of powder particles by an electric discharge [30]. The pulse energizing method produces (a) spark plasma, (b) spark impact pressure, (c) Joule heating and (d) electric field diffusion effect [30]. Unlike in conventional sintering processes, SPS enables rapid and homogenous heating of the powder particles similar to self-propagating high temperature synthesis (SHS) and microwave sintering [30]. Figure 2.8 shows a schematic of a typical spark plasma sintering machine.

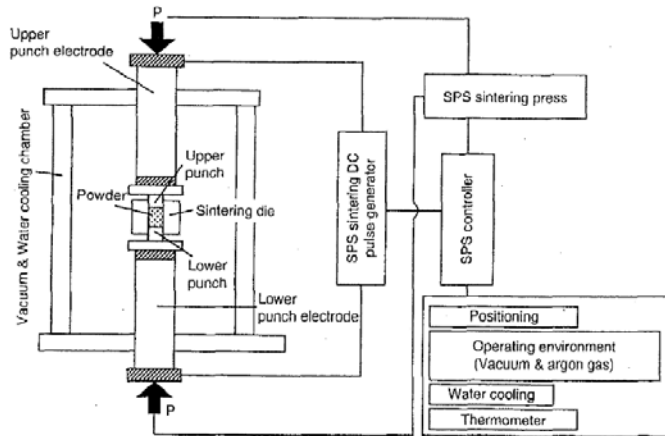


Figure 2.8: Schematic of the spark plasma sintering machine [30].

The SPS machine has two rams which also act as electrodes. A graphite sintering die is placed between the rams. The upper ram is connected to a hydraulic press that controls its movement and imposes the required load during sintering. Typically, sintering is carried out either in a vacuum or an inert atmosphere (e.g. Ar, He). As per the sintering program, the DC pulse generators supply the voltage and current to the sintering die and heat-up the powders within the die.

The current flowing through the gaps between the powder particles creates an electric spark discharge. Figure 2.9 shows the pulse current flowing through the powder particles and the formation of the discharge [30]. The frequency of the On – Off pulse current disperses the Joule’s heating and spark discharge effect homogeneously throughout the powder interparticle voids, ensuring homogeneity and uniformity in the temperature profile within the powders [34].

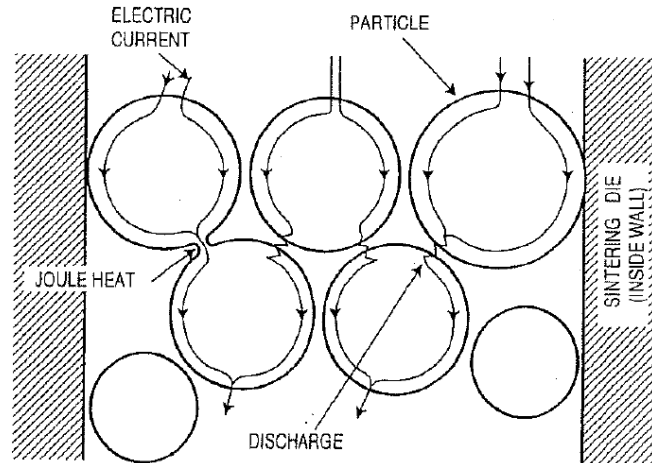


Figure 2.9: Pulse current passing through the powder particles in an SPS process [30].

It is believed that a momentary increase in the temperature causes localized surface melting of the powders [34]. Due to the On – Off pulsating nature of the current, the surfaces of the powder particles are drawn together to form necks. The external applied uniaxial pressure during the sintering and the continuous Joule’s heating helps in the formation and growth of the necks [34]. The different stages of the formation of necks have been summarized by Tokita [30], as shown in the Figure 2.10.

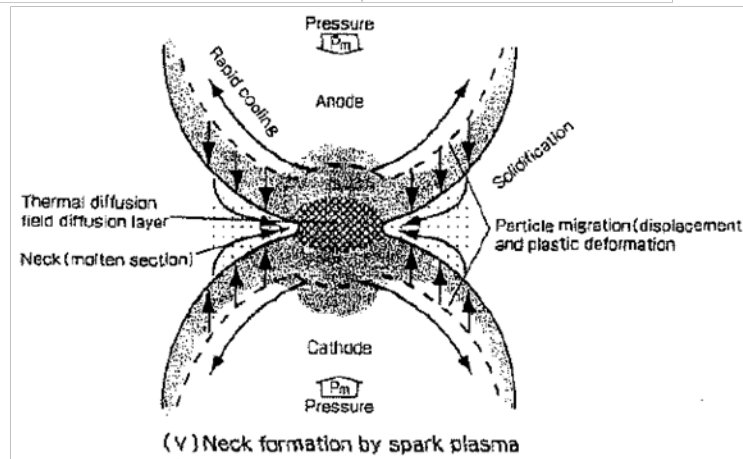
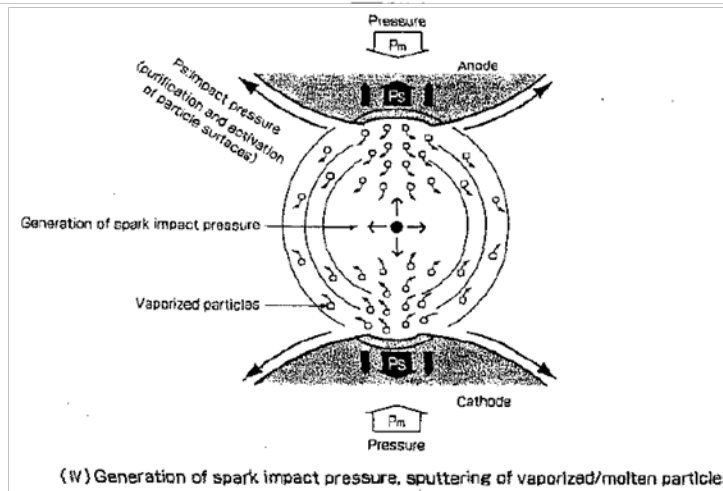
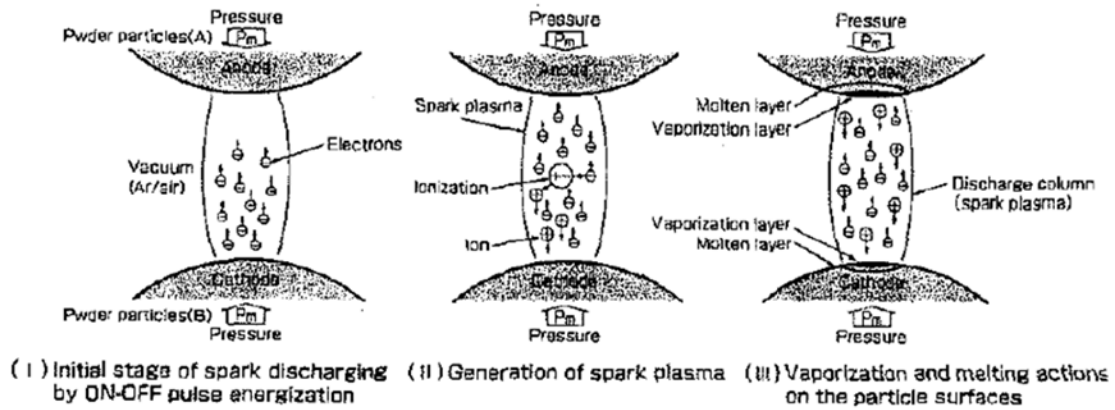


Figure 2.10: Stages of necking during SPS [30].

Apart from aiding the formation and development of the necks during the initial stages of sintering, the external pressure has been reported to have significant effect on the

densification of the powders during the sintering process [34]. The external pressure not only retards and restricts the powder grain growth during sintering, but also promotes particle rearrangement, which enhances densification and homogenous diffusion during sintering [34].

Figure 2.11 shows the different stages of the sintering process during spark plasma sintering process. Figure 2.11a shows the formation of a few necks during the initial stage of sintering. As the pressure increases, particle rearrangement was observed and the number of necks increased accompanied by an expansion of the existing necks (Figure 2.11b). With further progress in sintering, there was a plastic flow of the material along the grain boundaries. This plastic flow eliminated the pores between the fused grain boundaries, resulting in a highly dense material (Figure 2.11c) [30].

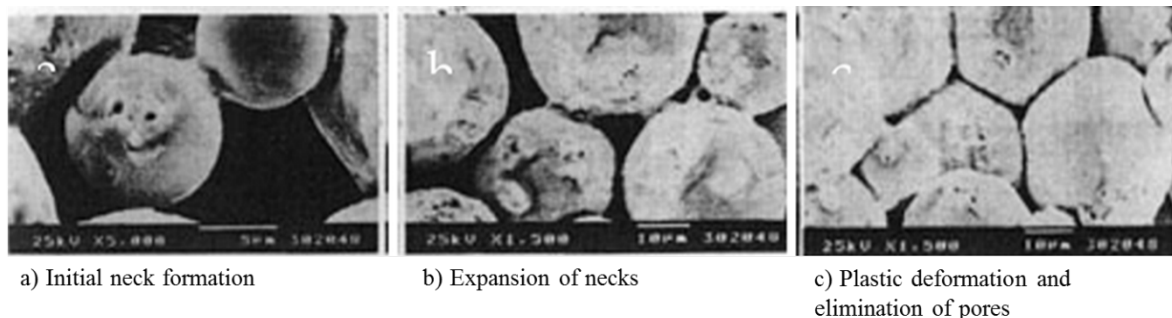


Figure 2.11: Sintering stages during SPS sintering: a) Initial neck formation; b) Expansion of necks and c) Plastic deformation and elimination of pores [30].

The sintering pressure has been confirmed to be a fundamental parameter affecting the SPS performance and the microstructure of the sintered materials. Grasso *et al.* [35] showed that the applied pressure affected the bulk electric and thermal fields in the sintered powders

during processing. The temperature difference between the punch-die powder assembly setup decreased with the increase in the applied pressure [36].

2.5 Spark Plasma Sintering of YSZ

Chen *et al.* [37] investigated the microstructure of YSZ ceramic prepared by the SPS process. Their investigation aimed at producing high density ceramic through process cycling, i.e. controlled arrest or repeat of sintering temperature/ pressure/ time during processing. They found that the relative density of the ceramic samples initially increased with the increase in the number of sintering cycles. After three cycles, a plateau in the density was observed, as seen in Figure 2.12a, with the relative density of the as-sintered samples constant at ~96 to 97%. As seen in Figure 2.12b, an increase in the sintering pressure from 3.5MPa to 23MPa increased the density of the samples from 93.5% to 99.1%. The dependence of the relative density on the temperature was also studied and the results suggest an increase in density with temperature. It was noted that the maximum density of 99.1% was achieved on the fourth consecutive sintering cycle at 1400°C and 23MPa for 3 minutes [37].

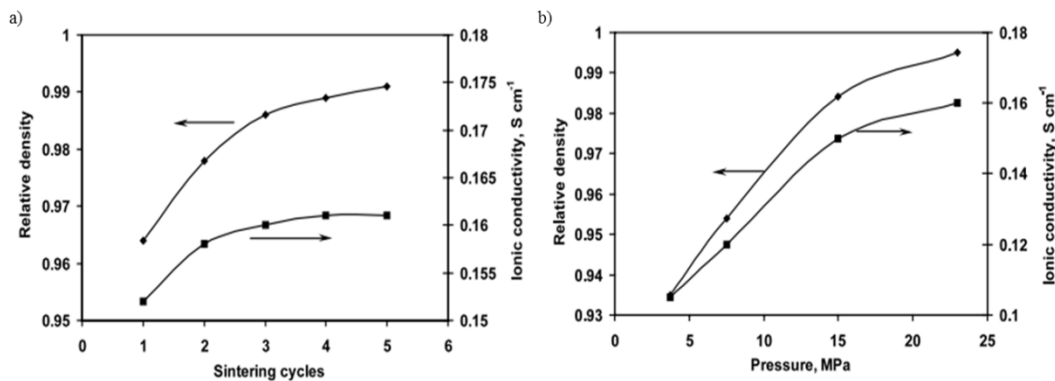


Figure 2.12: Relative density and ionic conductivity as a function of: a) Sintering cycles and b) Sintering pressure [37].

A similar study was conducted by Chaim *et al.* [38] who examined the densification of YSZ processed via SPS. Different heating rates, temperature ranges and pressures were studied in order to determine the densification characteristics of YSZ. A high density (~99%) was achieved at 1400°C, 100MPa for 5 minutes. On the basis of the densification plots obtained, the powders started densifying at approximately 650°C under a pressure of 100MPa and continued densifying up to 900°C with the highest rate of densification seen at 750°C. Chaim *et al.*'s [39] studies also suggested that at faster heating rate, the grain growth increased and lead to a decrease in the mechanical properties of the ceramic. Also, increasing the sintering temperature was seen to increase the grain size. Sintering YSZ above 1400°C adversely affected the relative density of the samples [38].

Tamburini *et al.* [40] fabricated 8mol% YSZ ceramics by high pressure spark plasma sintering carried out between 930-1350°C with a pressure of 35-1000MPa for 5 minutes. The sintering dwell time was kept constant at 5minutes with a heating rate of 200°C/min. The as-sintered discs reached densities as high as 98% with grain size of ~10nm [40].

Takeuchi *et al.* [41] studied the mechanical properties of 8mol% YSZ, fabricated by spark plasma sintering and compared it to conventionally sintered samples. All sintering was carried out at 30MPa pressure at temperatures between 1100-1300°C with a heating rate of 160°C/min. The dwell time at sintering temperature was varied between 1 to 30 minutes. The samples fabricated by conventional sintering were compressed by a load of 190MPa and sintered at 1200-1600°C for 2 hours. For both manufacturing routes, the densities of the as-sintered discs increased with the sintering temperature. In general, the densities of the SPS materials exceeded the conventionally sintered samples, as seen in Figure 2.13.

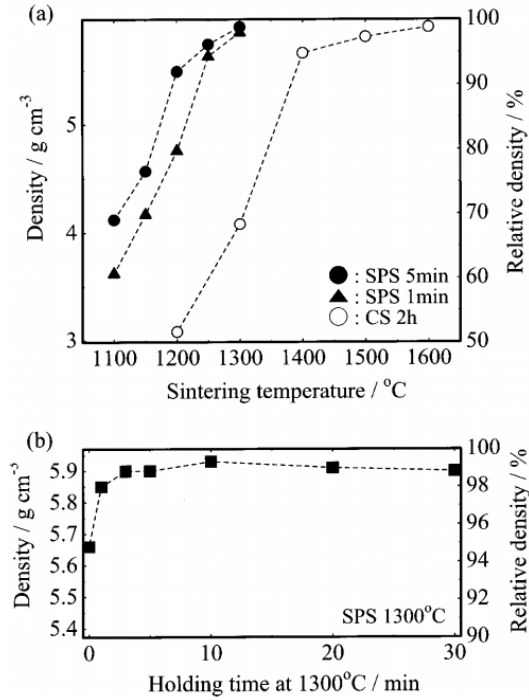


Figure 2.13: Relative densities of the as-sintered discs as a function of: a) Sintering temperature and b) Hold time [41].

Performing three point bend test on the sintered discs, Takeuchi *et al.* [41] observed that the SPS sintered discs (sintered at 1300 $^{\circ}\text{C}$ for 5 to 10 minutes) had a strength of 400MPa, whereas the conventionally sintered discs had a strength of 250MPa. This significant increase in strength was attributed to the small grain size of the SPS sintered discs [41].

The above works suggested that Spark Plasma Sintering is capable of producing high density YSZ ceramic composites. However, YSZ remains a brittle material, with negligible plasticity, which makes it unsuitable for many engineering structural applications. A promising additive to significantly enhance the mechanical, electrical and thermal properties of ceramics are carbon nanotubes (CNTs). Lately, a considerable amount of work has been done on the processing of CNT containing composites [39].

2.6 Carbon Nanotubes

Carbon nanotubes are carbon atoms arranged in a cylindrical molecule. A unique feature of the CNT structure is its periodic hexagonal pattern, as seen in Figure 2.14a. This structure results from the sp^2 hybridization, where one s-orbital and two p-orbitals combine to form three hybrid sp^2 -orbitals at 120° to each other [42].

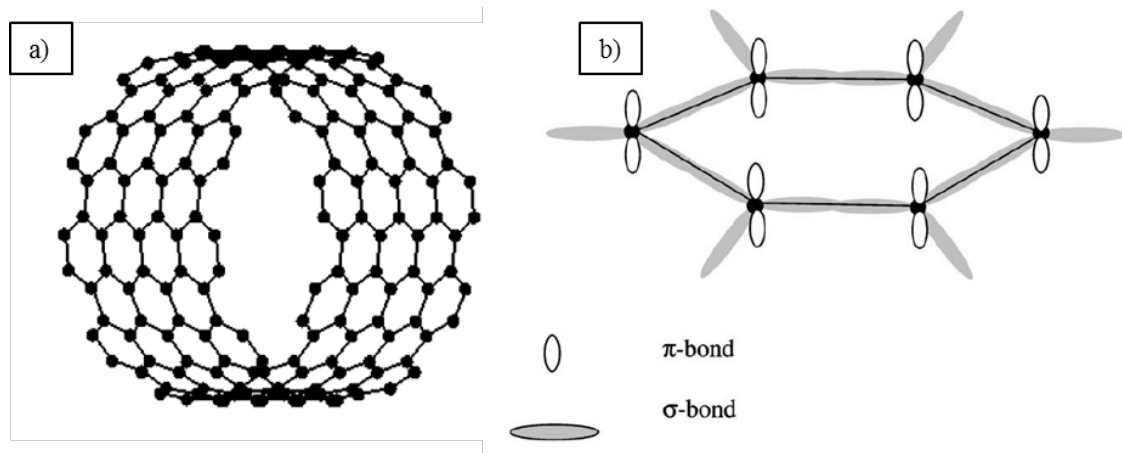


Figure 2.14: a) Molecular structure of a section of a CNT where each node here represents a carbon atom and the lines represents the bonds between them; b) Hexagonal structure of one graphite layer [42].

The covalent σ -bond is a strong chemical bond responsible for the high mechanical properties of the CNTs. The π -bond is a relatively weaker bond that contributes to the interaction between the CNT bundles [42].

CNTs can be classified as Single-Walled CNTs (SWCNTs), Double-Walled CNTs (DWCNTs) and Multi-Walled CNTs (MWCNTs). The density of the CNTs is highest in the case of SWCNT with an outer diameter less than 2nm. As the diameter increases and the number of walls increase, the density of the CNTs decreases [43].

The mechanical performance of the CNTs also depends on their structure. For example, Lourie *et al.* [44] estimated the compressive strength of the CNTs using micro-Raman spectroscopy. They reported that the SWCNTs had a Young's modulus of 2.8-3.6TPa and the MWCNTs had a Young's modulus of 1.7-2.4TPa [44]. Yu *et al.* [45] conducted direct tensile testing on the SWCNTs and MWCNTs. Young's modulus of the SWCNTs ranged from 320 to 1470GPa, while the MWCNTs had a Young's modulus ranging from 270-950GPa [45]. This is particularly relevant to ceramics, which generally tend to have a poor ductility and toughness.

Inglis [46] and Griffith [47] studied the effect of flaws on the strength of brittle materials. It was seen that the removal of flaws from brittle materials resulted in the enhancement of their strengths [46, 47]. According to Griffith [47], the toughness of a brittle material can only be improved by reducing the density of the flaws or by introducing second phases such as whiskers, platelets, particulates and fibres at the matrix grain boundaries. In this regard, addition of Carbon nanotubes to ceramics has shown a great promise [48].

2.6.1 Fabrication and Characterization of CNT-Ceramic Composites

Incorporation of CNTs to a ceramic matrix significantly enhances the fracture toughness and other mechanical properties of the ceramic composites via grain boundary pinning [48]. To achieve maximum effect, the CNTs must be homogeneously dispersed in the ceramic matrix, since agglomeration of the CNTs naturally occurs due to the high Van der Waals forces of attraction between the individual CNTs [49]. Further caution needs to be taken to prevent the CNTs from being damaged during fabrication (i.e., CNTs may revert to graphite at temperatures above 1150°C) [50].

Ma *et al.* [51] used nano-sized SiC powder matrix mixed with 10wt% CNTs to fabricate a SiC-CNT ceramic composite. The composite powder was hot pressed at 2000°C, with 25MPa pressure for 1hour in Ar atmosphere. It was observed that at these process conditions the CNTs were retained and not damaged, as seen in Figure 2.15. In terms of the mechanical properties, addition of the 10wt% CNTs increased the fracture toughness by ~10% [51].

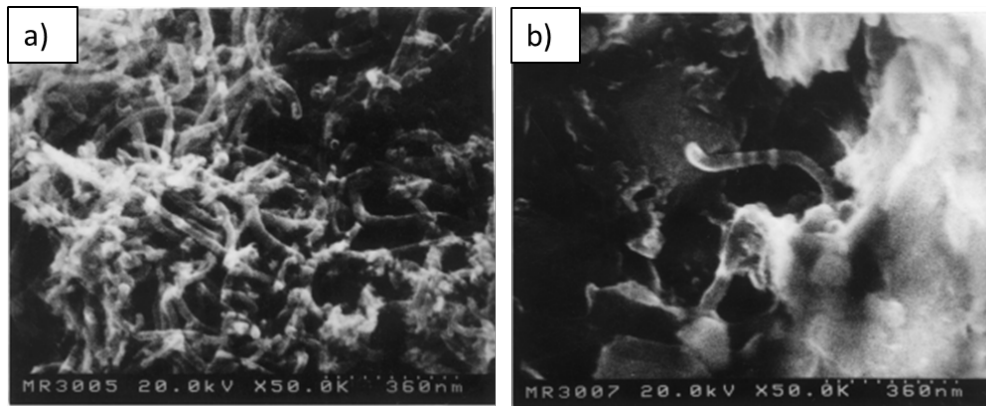


Figure 2.15: CNTs seen in the SiC matrix after hot pressing at two different sites:

a) Site 1 and b) Site 2 [51].

Subhranshu *et al.* [48] reported that CNTs could be incorporated into ceramic composite matrix using a carrier (e.g., a catalyst) for nanotube growth (e.g., Fe, Ni, Co) using the Chemical Vapor Deposition (CVD) process. This approach was seen to produce a uniform distribution of the CNTs in the ceramic matrix as long as carbon containing gases (e.g., C₂H₂ or CH₄) did not affect the mass-transfer gradients in the powders [48].

Hurst [52] conducted studies on the enhancement of the high temperature fracture toughness of CNT reinforced Alumina and Zirconia composites. Tape casting and hot pressing were used for the fabrication of the composites and reported that in tape cast 5wt% CNT-Al₂O₃, the CNTs deflected cracks into CNT-free grain boundary regions. In the case of the hot

pressed composite, grain size reduction due to the presence of CNTs was observed and resulted in enhanced strength of the ceramic. In the case of the tape cast zirconia composites, a similar result was observed [52].

Yamamoto *et al.* [53] worked on SPS processing of MWCNT reinforced Alumina composites. The CNT- Al_2O_3 composites were sintered at 1500°C, with a sintering pressure of 20MPa for 10 minutes. Based on XRD results, the authors concluded that alumina CNT composites can be sintered using SPS. SEM analysis confirmed that the CNTs were located in the intergranular regions and acted as restriction for the matrix grain growth [53].

2.6.2 Fabrication and Characterization of CNT-YSZ Ceramic Composites

Literature suggests that the addition of the CNTs to the YSZ ceramic matrix enhances the mechanical properties of the resulting composites. Milsom *et al.* [54] studied the effect of CNTs on the sintering behaviour of YSZ by spark plasma sintering. 0.5-2vol% CNT were added to YSZ and sintered at temperatures between 1150 - 1400°C, 16MPa pressure with heating and cooling rates of 200°C/min and 150°C/min, respectively. The green density of the as-sintered compacts was seen to increase with the increase in the CNT content from 48.5% (for pure YSZ) to 53.4% (for 2vol% CNT-YSZ). The authors suggested that the CNTs aided in the particle rearrangement by acting as lubricants. The final relative density of the as-sintered samples increased with the increase in the sintering temperature and increasing CNT content, as seen in Figure 2.16a. The grain size increased with the increase in the sintering temperature, but slightly decreased with the increase in the CNT content, as seen in Figure 2.16b. [54].

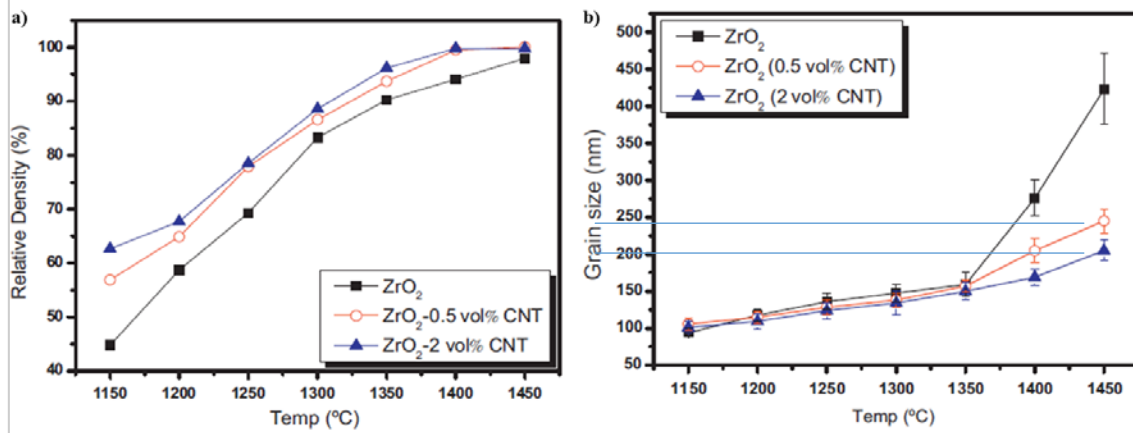


Figure 2.16: a) Relative density and b) Grain size measurements of CNT-YSZ ceramic composites [54].

Calculation of the activation energy for sintering of the powder particles revealed that increasing the content of CNTs decreased the activation energy for sintering [54].

Martin *et al.* [55] studied the processing and characterization of SWCNT-YSZ ceramic composites by spark plasma sintering. The effect of adding 1 and 5wt% CNTs on the processing and characterization of the composites was investigated. The ceramic composites were spark plasma sintered with a constant heating rate of 100°C/min. Table 2.1 shows the combinations of the sintering parameters [55]:

Table 2.1: Sintering conditions [55].

Run no.	Temperature (°C)	Pressure (MPa)	Sintering time (min)
1	1250	50	5
2	1100	50	20
3	1250	75	5

It was observed that all the samples had attained almost full density (>98%) except for the 5% CNT-YSZ composite which reached only 92.9% density. For all samples, the CNTs were successfully retained in the YSZ. SEM analysis and grain size measurements revealed that for the composites sintered at 1250°C, the grain size decreased with the increase in the CNT content. However, the grain size of the CNT-YSZ composites remained smaller than the grain size of plain YSZ sintered at the same condition. This was attributed to the presence of the CNTs at the grain boundaries [55].

Mehdi *et al.* [56] studied the processing and performance of YSZ reinforced with MWCNTs. Commercially available 3 mol% YSZ (70nm particle size) was used as the matrix into which 0, 0.5, 1.5, 3 and 5wt% MWCNTs were blended. The ceramic composites were processed via SPS at 1250 - 1350°C, sintering pressure of 50MPa and a constant heating rate of 50°C/min. It was seen that for plain YSZ and 0.5, 1.5wt% CNT-YSZ composites, a sintering temperature of 1250°C was sufficient to yield an ~98% dense composite. With additional doping of CNTs, the density of the as-sintered composites decreased. SEM analysis of the as-sintered composites revealed that most of the CNTs were intact and did not disintegrate during the processing. The CNTs were seen to be homogeneously distributed throughout the samples even for high CNT concentrations of 5wt%, surrounding most of the YSZ grains. The addition of the CNTs lead to the reduction in the matrix grain size [56]. Addition of CNTs to the YSZ matrix was seen to significantly enhance the mechanical properties of the resulting composites. The Young's modulus of the composites increased from 198GPa for YSZ to 258GPa for 5wt% CNT-YSZ composite. Similarly the indentation fracture toughness of the composites increased by 5.52 MPam^{1/2} with the addition of 5wt% CNTs to the YSZ

matrix. The Vickers hardness of the composites increased from 12.1 to 12.8GPa with 5wt% CNT addition [56].

Similar results were obtained by Datye *et al.* [57] who studied the mechanical properties and microstructure in spark plasma sintered direct *in-situ* grown MWCNT – YSZ ceramic composites [57]. According to the authors, *ex-situ* mixing of the MWCNTs and YSZ leads to non-homogenous dispersion of the MWCNTs in the YSZ matrix. Datye *et al.* used $\text{Co}(\text{NO}_3)_2 \cdot 6\text{H}_2\text{O}$ catalyst to grow the MWCNTs in the YSZ matrix and then Spark Plasma Sintered the powders at 1400 and 1600°C for 4minutes. The addition of the MWCNTs slightly reduced the density of the samples from 6.05 to 5.89 g/cm³. The MWCNTs also reduced the grain size from 1µm for the pure YSZ sample to 0.3µm for 4wt% MWCNT-YSZ composite. Three point bend test results suggested that the flexural strength of the composites increased with the increase in the MWCNT concentration, as shown in Figure 2.17. This trend was attributed to the finer grain size of the MWCNT-YSZ composites, and also a successful distribution of MWCNTs on the YSZ grain boundaries [57].

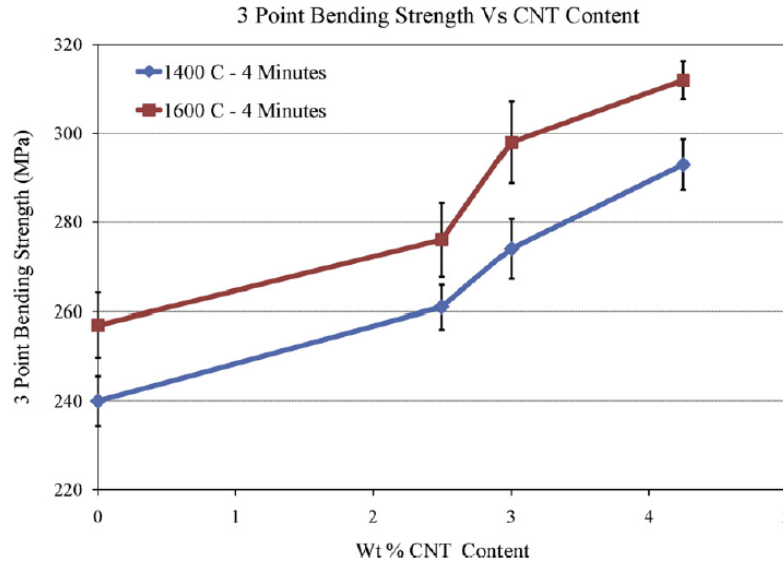


Figure 2.17: Three point bed test results for the MWCNT-YSZ ceramic composites sintered at two different sintering temperatures [57].

Shin *et al.* [58] quantified the mechanical and electrical properties of SWCNT reinforced 3mol% YSZ ceramic composites fabricated by Spark Plasma Sintering [58]. HRTEM images of the mixed powders showed that the initial powders were spherical and had a size of ~100nm. The CNTs were seen to be well dispersed in the YSZ matrix and no agglomeration was noticed. The mixed powders were then spark plasma sintered with a heating rate of 100°C/min at 1350 and 1450°C for 5minutes. XRD analysis of the as-sintered composites were all matching to the tetragonal zirconia peak indicating that there was no phase transformation as a result of the sintering process. It was observed that upto 1wt% CNT content, the density of the as-sintered composite was $\geq 98\%$ theoretical density (6.01 g/cm^3). As the CNT content further increased, the density of the composites decreased, thus indicating that the CNTs hindered the densification during the sintering process [58].

In this present work, the effect of both SWCNTs and MWCNTs on the densification behaviour and certain properties of spark plasma sintered YSZ ceramic composites have been investigated.

Chapter 3: EXPERIMENTAL PROCEDURE

In this research, fundamental studies on SPS processing of YSZ composites were carried out. In the first phase of the research, the effect of sintering parameters on the densification behaviour of 8mol% YSZ ceramics was studied. In the second phase of the research, the effect of addition of Carbon Nanotubes to YSZ was studied. Multi and Single Walled CNTs were added at varying concentration levels, and the effect on the densification behaviour and mechanical properties of the as-sintered ceramic composites was studied.

3.1 Precursor Powders

Commercially available high purity (99.9%) powder of 8 mol% Ytria Stabilized Zirconia was obtained from Inframat Advanced Materials, USA. Figure 3.1a shows that the raw powder had a non-homogenous particle size and shape distribution. Chemical analysis of the powders via SEM-X-EDS confirmed that the composition of the powders was consistent with that of YSZ, as shown in Table 3.1.

Table 3.1: Composition of the YSZ powder.

Powder	Composition (%)				
	Zr	O	Y	Hf	Cl
YSZ – actual	63.40	24.58	9.93	1.63	0.46
YSZ - theoretical	68.10	25.59	6.29	—	—

Single Wall Carbon Nanotubes (SWCNTs) were obtained from NRC-SIMS, Montreal, Quebec, while Mutli Wall Carbon Nanotubes (MWCNTs) were obtained from Sigma

Aldrich. The SWCNTs were double laser generated carbon nanotubes without any surfactants or additives. SEM micrographs of the raw CNTs are shown in Figure 3.1b and c.

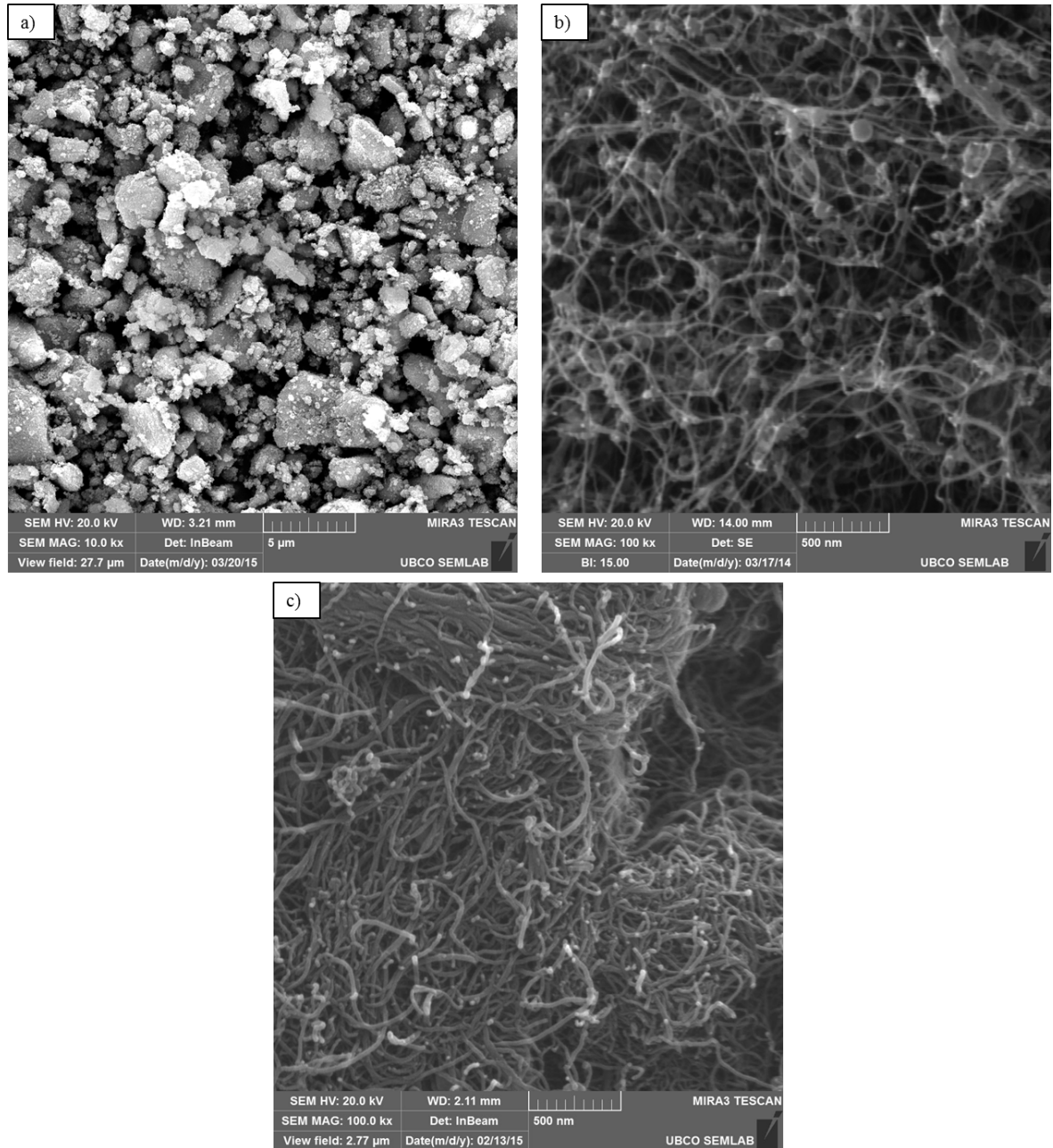


Figure 3.1: SEM micrographs of: a) YSZ; b) SWCNT; c) MWCNTs.

The SWCNTs were analysed under high resolution magnification and their diameter was measured to be ~20nm. The SEM analysis also revealed the presence of impurities in the

form of $\sim 1\mu\text{m}$ thick Al rich tubes in few sites of the SWCNT powders, as seen in the Figure 3.2. No impurities were found from the SEM images of MWCNT powders. The MWCNTs had an average diameter of $\sim 25\text{nm}$.

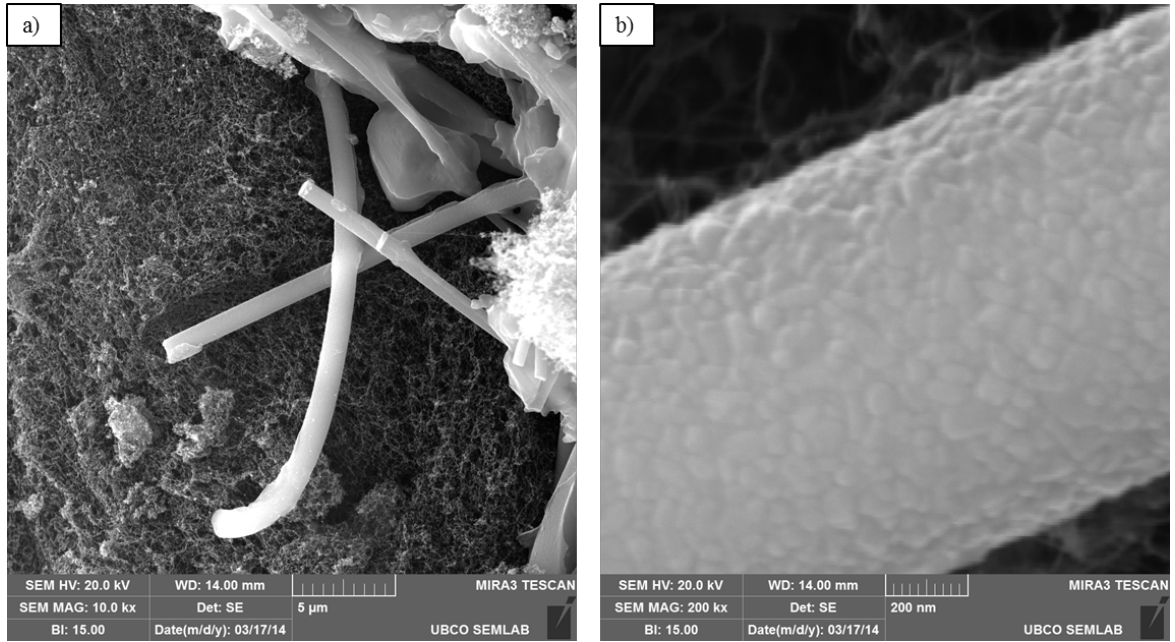


Figure 3.2: Impurities seen in the SWCNTs at: a) 10,000x and b) 200,000x magnifications.

3.2 Powder Blending

The 8 mol% YSZ matrix was blended with CNT powders to yield 0.2, 0.5 and 1wt% CNT-YSZ powder blends for both SWCNT-YSZ and MWCNT-YSZ blends.

The blending of SWCNT-YSZ powders was done at NRC-SIMS, Montreal. The powder blends were bath and tip sonicated and mechanically mixed to ensure homogenous distribution of the SWCNTs in the matrix. For instance, the mixing procedure for preparing the 0.2wt% SWCNT-YSZ powder blend involved the following steps: 0.2g of the loose raw SWCNT powder was added to 1L of MeOH. The solution was sonicated and then 99.8g of

YSZ powder was added during mechanical stirring. The mixture was further stirred and again bath sonicated for one hour. The mixture was then heated and stirred on a hot plate at 60°C to allow the MeOH to evaporate. As the solution turned into a slurry, it was manually mixed with a spatula until it formed a fully dry solid. This dry mass was then baked at 150°C for 2 hours followed by further baking at 200°C for another 2 hours followed by slow cooling to room temperature in order to completely remove MeOH residue or any moisture.

The MWCNT-YSZ powders were blended at UBC, Kelowna. During mixing of the MWCNT-YSZ powders, sonication and mechanical stirring were used. No additional surfactants or additives were added to the powders. The mixing procedure for blending the 0.2wt% MWCNT-YSZ powders was: 0.2g of the raw dry MWCNT powder was added to 0.2L MeOH (at a CNT to MeOH ratio of 1g/L). This suspension was manually mixed using a spatula for 2 minutes and bath sonicated for 3 hours. To this suspension, 99.8g of YSZ was added while mechanically stirring the solution. The mixture was stirred in a closed beaker using a magnetic stirrer for 4 hours and then heated on a hot plate to 60°C, while continuing the mixing until a slurry formed. The slurry was then manually mixed with a spatula until dry, followed by baking at 150°C for an hour to completely remove MeOH residue or any moisture. This dry mass was then ground with a mortar and pestle for ~1 minute.

3.3 Spark Plasma Sintering of Powder Blends

The consolidation of the powder blends to create solid compacts was done at the University of British Columbia, Okanagan campus using a Thermal Technologies LLC 10-3 Spark Plasma Sintering system shown in Figure 3.3.

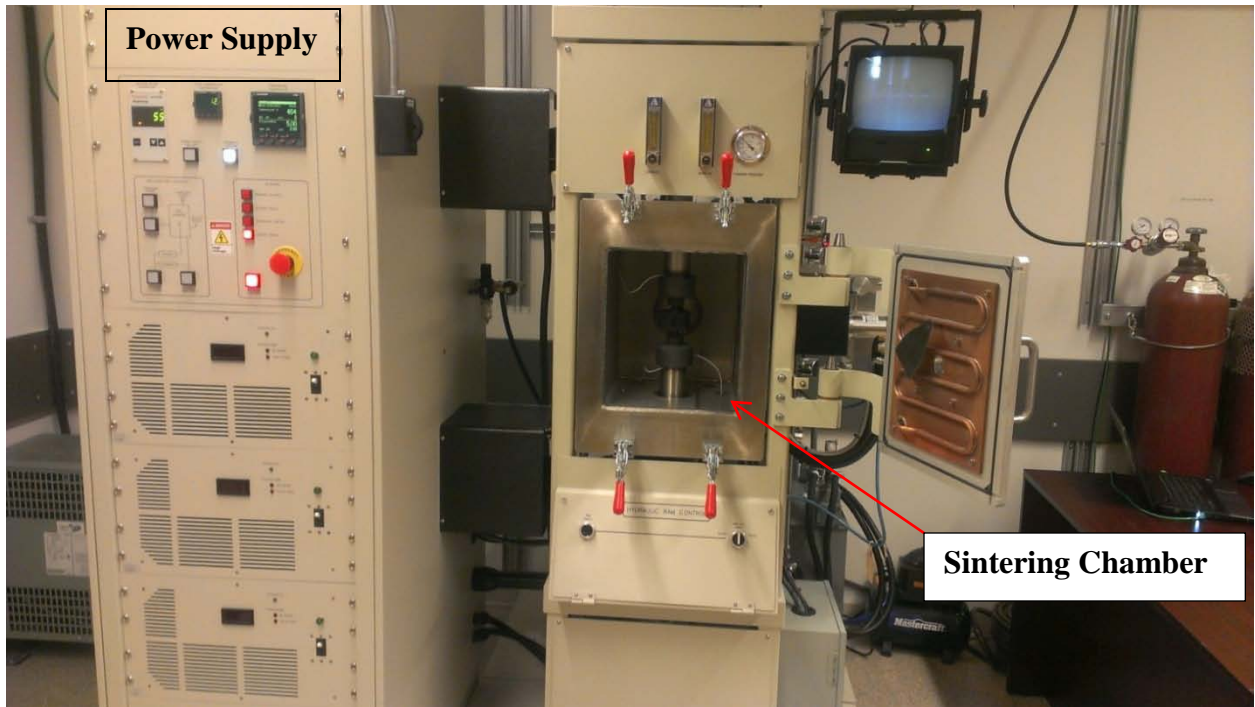


Figure 3.3: Photograph of the SPS sintering machine (LLC 10-3 SPS).

The 10-3SPS system consists of a sintering chamber and a control unit connected to a laptop data acquisition unit. The sintering chamber is connected to a vacuum pump, air flow vent, and a water cooling system. An Argon (Ar) cylinder provided inert atmosphere during sintering of all specimens. The sintering temperature, sintering pressure, heating rate, cooling rate, dwell time and the pressure loading and unloading rates were programmed using the laptop loaded with Eurotherm software.

ISOCarb graphite tooling with interior diameter of 20mm was used for all the experiments. Graphoil sheets of 1.27mm thickness were used to line the inner surfaces of the die and the punch prior to pouring the powders into the die. A carbon wool sleeve was placed over the loaded die to provide thermal insulation. The assembled die was then placed into the SPS chamber, as seen in Figure 3.4b.

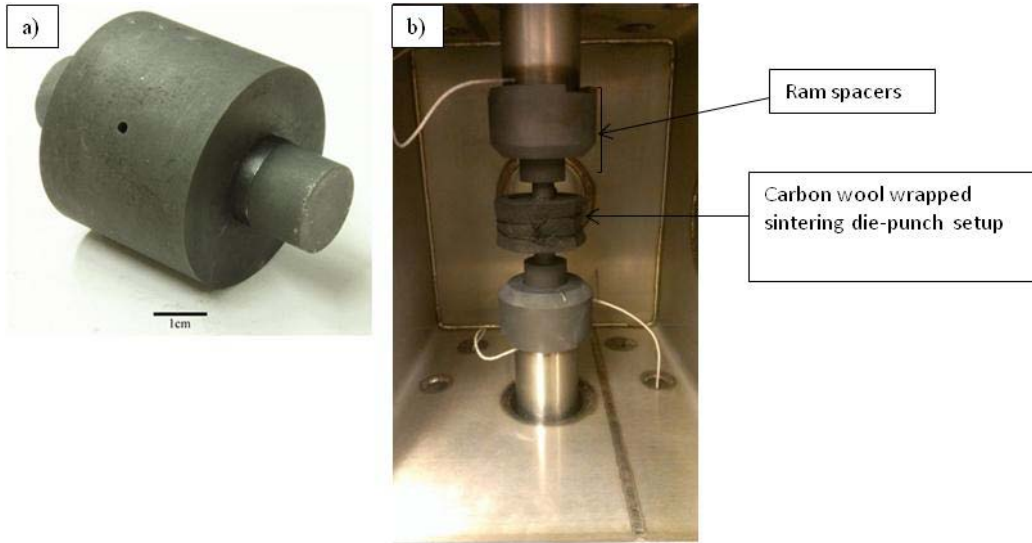


Figure 3.4: Photographs of: a) ISOcarb sintering die and b) Sintering chamber.

Once the die was placed into the SPS chamber, a preload of 5MPa was applied to precompact the powder in the die to ensure uniform powder density. The SPS chamber doors were closed and the vacuum pump was turned on to achieve at least 2×10^{-2} Torr vacuum prior to back-filling the chamber with Ar. Then, the SPS program was executed.

The densification behaviour of the powders during the sintering cycle was studied by analyzing the instantaneous density of the compacts as a function of the ram position and the theoretical density of YSZ, as per Equation 3-1:

$$D = \left(\frac{L_f}{L}\right) D_f \quad \text{Equation 3-1}$$

Where, D was the instantaneous density, L_f was the final thickness of the as-sintered disc, L was the instantaneous thickness of the compact which was measured with respect to the position of the rams during the sintering runs and D_f was the theoretical density of YSZ. In this equation the theoretical density was 6.01g/cm^3 , as per the manufacturer material data sheet [59].

3.3.1 Spark Plasma Sintering of Pure 8 mol% YSZ Ceramics.

Sintering experiments were carried out to study the influence of SPS process parameters on the properties of the YSZ ceramic. For all the experiments $\sim 7.000 \pm 0.005$ g of the YSZ powder was used for the fabrication of the samples. A number of test samples were fabricated and used for optimization purposes. The sintering parameters studied in this thesis are summarized in the Table 3.2.

Table 3.2: SPS sintering parameters for pure YSZ

Sample No.	Heating cycle				Cooling cycle		
	600 °C	1000 °C	1300 °C	1400 °C	800 °C	600 °C	Cooling rate
Y1	3mins 0MPa	3mins 30MPa	3mins 30MPa	——	0mins 0MPa	0mins 0MPa	Ambient cooling
Y2	3mins 0MPa	3mins 30MPa	——	3mins; 30MPa	0mins 0MPa	0mins 0MPa	Ambient cooling
Y3	3mins 0MPa	——	3mins 30MPa	——	0mins 0MPa	0mins 0MPa	Ambient cooling
Y4	——	3mins; 30MPa	3mins 30MPa	——	0mins 0MPa	0mins 0MPa	Ambient cooling
Y5	3mins 0MPa	——	5mins 30MPa	——	0mins 0MPa	0mins 0MPa	Ambient cooling
Y6	3mins 0MPa	——	1min 30MPa	——	0mins 0MPa	0mins 0MPa	Ambient cooling
Y7	3mins 0MPa	——	1mins 30MPa	——	0mins 0MPa	0mins 0MPa	100°C/min
Y8	——	——	3mins 30MPa	——	0mins 0MPa	0mins 0MPa	100°C/min
Y9	3mins 0MPa	——	3mins 30MPa	——	0mins 0MPa	0mins 0MPa	100°C/min
Y10	3mins 0MPa	——	3mins 30MPa	——	0mins 0MPa	0mins 0MPa	Ambient cooling
Y11	3mins 0MPa	——	——	5mins 30MPa	0mins 0MPa	0mins 0MPa	Ambient cooling
Y12	3mins 0MPa	——	——	3mins 50MPa	0mins 0MPa	0mins 0MPa	100°C/min
Y13	3mins 0MPa	——	——	7mins 50MPa	0mins 0MPa	0mins 0MPa	100°C/min
Y14	3mins 0MPa	——	3mins 50MPa	——	0mins 0MPa	0mins 0MPa	100°C/min
Y15	3mins 0MPa	——	3mins 30MPa	——	0mins 0MPa	0mins 0MPa	100°C/min
Y16	3mins 0MPa	——	3mins 30MPa	——	5mins 0MPa	3mins 0MPa	1300 °C to 800°C @ 50 °C/min. 800 °C to 600°C @ 100 °C/min

A number of repeats of these samples were made at each test condition in order to validate the repeatability of the sintering process. It was observed that the SPS process produced repeat samples of consistent density and integrity. Figure 3.5 shows the photographs of some of the as-sintered discs. It was seen that most of the samples fractured upon ejection from the sintering dies.

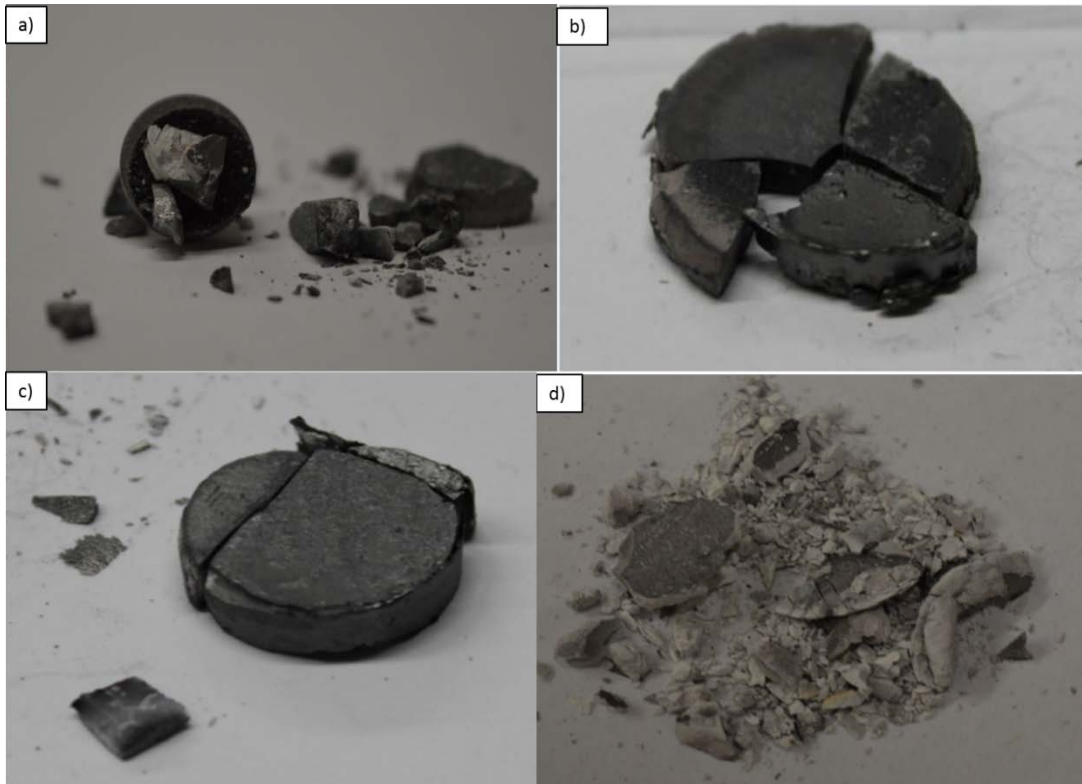


Figure 3.5: Photographs of the as-sintered YSZ samples: a) Sample Y1; b) Sample Y2; c) Sample Y5 and d) Sample Y6.

3.3.2 SW/MWCNT-YSZ Ceramic Composites

Based on the observations of the YSZ samples fabricated from the first phase of the research, the sintering parameters for the CNT-YSZ composites were determined. Again, 7.000 +/- 0.005g of the powder blends were used and loaded into the ISOCarb die and preloaded to

5MPa. Then, the samples were sintered at 1300°C and 1400°C with a sintering pressure of 30MPa for a 5 minutes dwell time. The heating and cooling rates for all the test runs were maintained at 100°C/min and 170°C/min, respectively.

3.4 Sample Polishing and Preparation

The as-sintered samples were polished to allow microstructure analysis and hardness testing. The first rough polishing was achieved with SiC papers of different grades: 120, 240, 360, 400 and 600 grit. Then diamond paste polishing using 9µm, 6µm and 1µm suspensions and a synthetic diamond extender was done.

For enhanced grain visibility, the samples were thermally etched for 1 hour in an MHI furnace at temperatures 50°C below the sintering temperature. The thermal etching was done in an ambient atmosphere. For all the samples, the heating rate and the cooling rate were maintained at 10°C/min.

3.5 Specific Gravity Measurement

The density of the as-sintered samples was measured by the Archimedes principle. The weight of the sample was measured in air and after immersion into deionized distilled water at room temperature. The specific gravity was calculated using Equation 3-2:

$$\text{Specific Gravity} = \frac{\text{weight in air}}{(\text{weight in air} - \text{weight in water})} \quad \text{Equation 3-2}$$

3.6 Hardness Measurement

The hardness of the samples was measured using a SXHV – 1000TA Micro Vickers hardness tester. The polished surfaces of the samples were used for the measurement. The hardness

measurement of the samples was in accordance with the ASTM C1327-08 standard [60]. All the hardness measurements were taken under a constant load of 9.87N with a dwell period of 10 seconds. A minimum of 10 readings for each sample were taken and averaged. Also, a calibration block was used prior the measurements to validate the instrument accuracy.

3.7 Microstructure Characterization

Scanning Electron Microscopy (SEM) was used to characterize the microstructure of the raw powders and as-sintered composites. The SEM analysis was done using a Tescan Mira3 XMU SEM with Oxford X-max X-ray Energy Dispersive Spectroscopy (X-EDS) detector. Prior to placing the samples on the sample holder platform of the SEM, 5nm of platinum-palladium (Pt-Pd) alloy was coated onto the sample surface using Cressington 208HR Sputter Coater. Imaging was done using secondary electron (SE) and backscattered electron (BSE) mode. The working distance was set to 14mm, and the beam voltage was 20kV. The SEM images were later used to perform grain size measurement via the linear intercept method using Buehler Omnimet image analysis software.

3.8 Thermal Analysis

The thermal diffusivity, thermal conductivity and the specific heat of the samples were determined in accordance with the ASTM E1461 – 13 standard [61]. The testing of the samples for thermal diffusivity was conducted at three different temperatures of 300°C, 600°C and 1300°C, using a NETZSCH 427 instrument. According to the ASTM standard [61] procedure, the material was subjected to a high intensity radiation energy for a short period of time. The propagation of the thermal energy through the sample was then measured. The measurement of the thermal properties was carried out at commercial

laboratories (Netzsch, Boston, MA, USA) by a licensed technician. The raw data was analyzed by the author.

3.9 Nanoindentation Testing

Selected composites were subjected to nanoindentation (NI) evaluation to determine the Young's modulus and the stiffness of the matrix of the composite materials. These experiments were performed at IIT Madras, India. The indentation experiments were conducted by the author using a Hysitron TI 950 nanoindentation tester. The machine used a Berkovich diamond indenter, with a tip radius <200nm. The testing was performed in an automation mode. The NI instrument was equipped with a 200x magnification optical microscope. With the help of this microscope, the surface was scanned and indentations were made on the surface of the sample. A minimum of 8 measurements were made for each sample. The loading and unloading curves were plotted and the machine automatically calculated the hardness and the Young's modulus of the material based on the depth of the indentation and the area of the indentation.

3.10 X-Ray Diffraction

To determine any phase evolution occurring during the SPS process, X-Ray diffraction was carried out at UBC Vancouver. Bruker Advance D8 diffractometer with Bragg – Brentano set-up was used. The diffraction peaks were measured in the 2θ range of 20° to 90° . The step size was set to 0.02° at a rate of 20s per step with Cu – $K\alpha$ radiation. The diffraction peaks obtained from the XRD were analyzed using X'Pert Highscore analysis software. The indexing was carried out with respect to the JCPDS and ICSD databases.

Chapter 4: RESULTS AND DISCUSSIONS

The results obtained from the experimental studies described in Chapter 3 are presented in this chapter along with an in-depth discussion of the observations.

4.1 Characterization of YSZ Precursor Powder

The SEM imaging of the YSZ powders revealed that the powders were irregularly shaped as seen in Figure 4.1. The average size of the particles was $0.47 \pm 0.05 \mu\text{m}$. At higher magnifications, it was observed that the particles had sub-granular structure with a sub-grain size of $\sim 35.5 \pm 11.7 \text{nm}$, as shown in Figure 4.1b to Figure 4.1d.

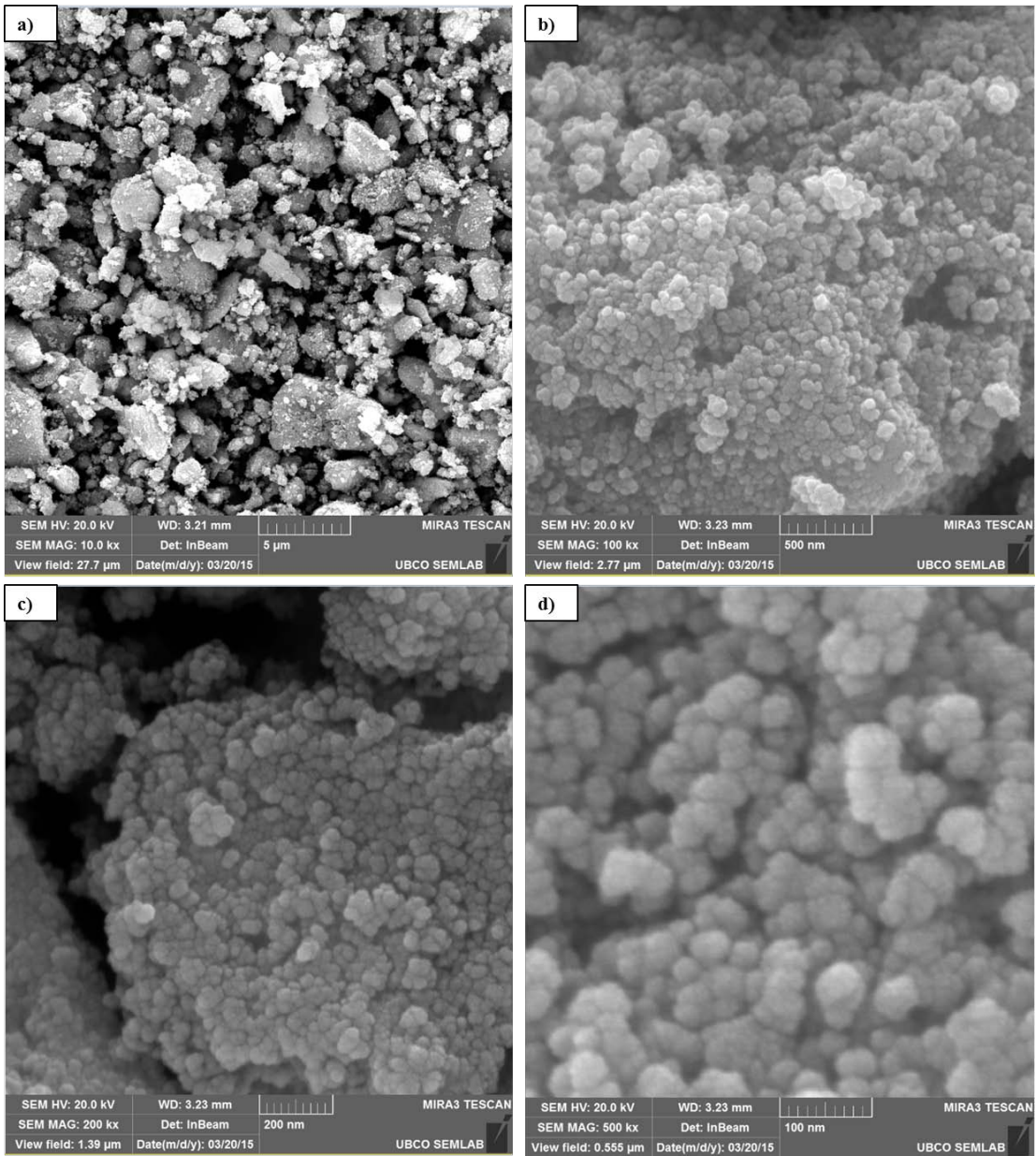


Figure 4.1: SEM images of the YSZ powder at different magnifications showing the powder particle structure: a) 10,000x magnification; b) 100,000x magnification; c) 200,000x magnification and d) 500,000x magnification.

X-EDS results indicated the presence of small amounts of impurities in the powders in the form of Cl and Hf, as seen in Table 4.1. These impurities could be a by-product of the coprecipitation method used for making YSZ powders.

Table 4.1: Composition (wt. %) of YSZ powders by X-EDS.

Powder	Zr	O	Y	Hf	Cl
YSZ	63.40	24.58	9.93	1.63	0.46

4.2 Densification of 8mol% YSZ

As mentioned in the experimental procedure chapter, a number of sintering runs with different sintering parameters were performed in order to determine the optimum sintering process parameters to fabricate high density YSZ ceramic discs. It was seen that the samples sintered at high temperatures and for a long dwell time had disintegrated immediately after ejection from the sintering die. This could be due to the high thermal gradients leading to high residual stresses built up during the sintering process [62, 63].

The final density and integrity of the as-sintered discs is summarized in Table 4.2. The densities of the repeats were within $\pm 5\%$ deviation from the average reported values. Photographs of some of the disintegrated samples are shown in Figure 4.2. Since several of the as-sintered discs crumbled on further handling, further examination and characterization of such samples was not possible.

Table 4.2: Densities of the as-sintered YSZ composites.

Sample No.	Heating cycle				Cooling cycle			Specific gravity (%)	Integrity
	600 °C	1000 °C	1300 °C	1400 °C	800 °C	600 °C	Cooling rate		
Y1	3mins 0MPa	3mins 30MPa	3mins 30MPa	————	0mins 0MPa	0mins 0MPa	Ambient cooling	96.50	Solid
Y2	3mins 0MPa	3mins 30MPa	————	3mins; 30MPa	0mins 0MPa	0mins 0MPa	Ambient cooling	97.33	Fractured
Y3	3mins 0MPa	————	3mins 30MPa	————	0mins 0MPa	0mins 0MPa	Ambient cooling	96.83	Partially Solid
Y4	————	3mins; 30MPa	3mins 30MPa	————	0mins 0MPa	0mins 0MPa	Ambient cooling	97.43	Partially Solid
Y5	3mins 0MPa	————	5mins 30MPa	————	0mins 0MPa	0mins 0MPa	Ambient cooling	96.33	Fractured
Y6	3mins 0MPa	————	1min 30MPa	————	0mins 0MPa	0mins 0MPa	Ambient cooling	96.67	Fractured
Y7	3mins 0MPa	————	1mins 30MPa	————	0mins 0MPa	0mins 0MPa	100 °C/min	96.83	Solid initially
Y8	————	————	3mins 30MPa	————	0mins 0MPa	0mins 0MPa	100 °C/min	96.68	Fractured
Y9	3mins 0MPa	————	3mins 30MPa	————	0mins 0MPa	0mins 0MPa	100 °C/min	98.18	Fractured
Y10	3mins 0MPa	————	3mins 40MPa	————	0mins 0MPa	0mins 0MPa	Ambient cooling	97.18	Fractured
Y11	3mins 0MPa	————	————	5mins 30MPa	0mins 0MPa	0mins 0MPa	Ambient cooling	97.83	Fractured
Y12	3mins 0MPa	————	————	3mins 50MPa	0mins 0MPa	0mins 0MPa	100 °C/min	99.66	Partially Solid
Y13	3mins 0MPa	————	————	7mins 50MPa	0mins 0MPa	0mins 0MPa	100 °C/min	87.55	Partially Solid
Y14	3mins 0MPa	————	3mins 50MPa	————	0mins 0MPa	0mins 0MPa	100 °C/min	99.78	Partially Solid
Y15	3mins 0MPa	————	3mins 30MPa	————	0mins 0MPa	0mins 0MPa	100 °C/min	————	Fractured
Y16	3mins 0MPa	————	3mins 30MPa	————	5mins 0MPa	3mins 0MPa	1300 °C to 800°C @ 50 °C/min; 800°C to 600°C @ 100°C/min	————	Fractured

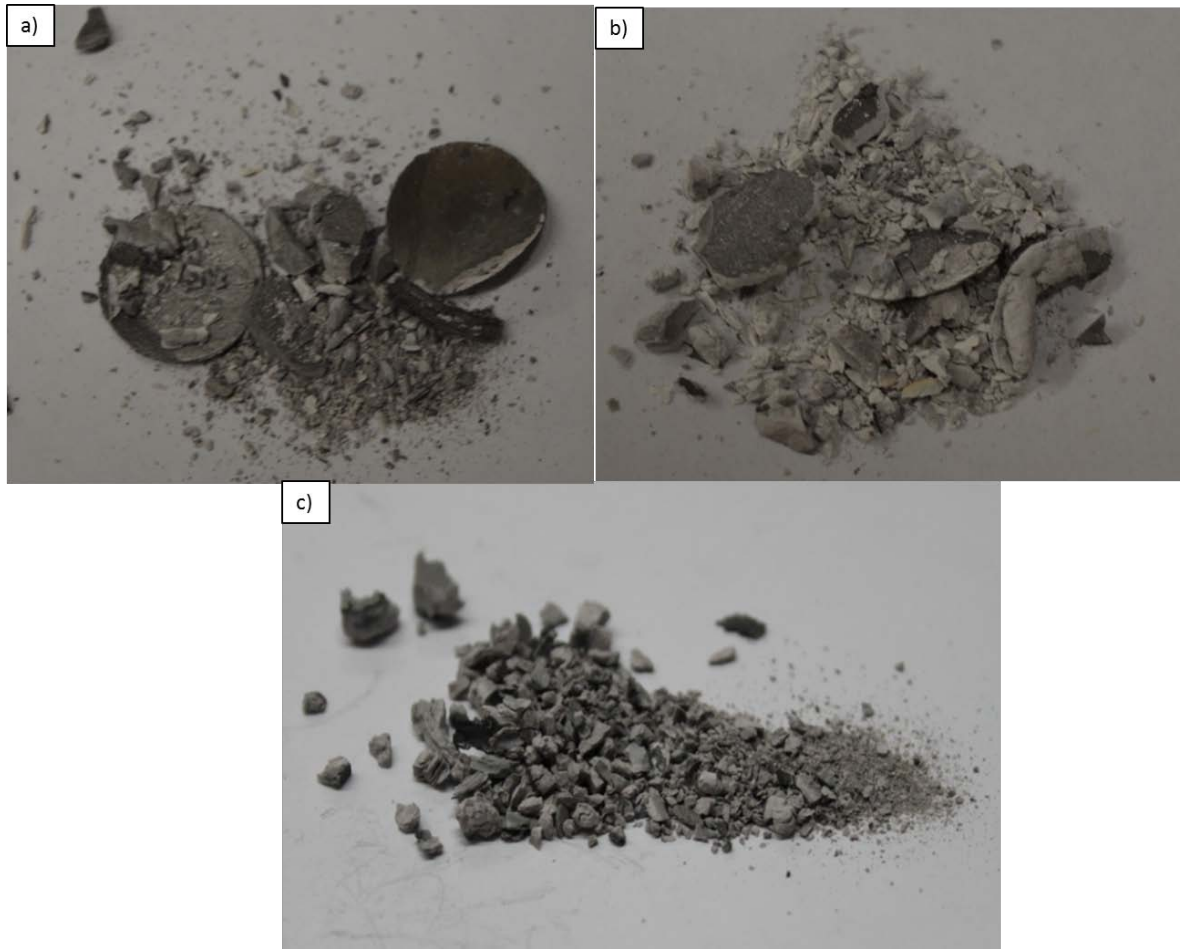


Figure 4.2: Photographs of the as-sintered YSZ samples seen to disintegrate post ejection:

a) Sample Y2; b) Sample Y5 and c) Sample Y8.

The fracture planes of some of the samples revealed a discoloration through the thickness of the samples, with the samples being grey/black near the outer surfaces, as seen in Figure 4.3. This was assumed to be carbon contamination from the graphite tooling which occurred during the sintering process. Tamburini *et al.* [64] reported that discoloration of YSZ discs during SPS processing can also be related to the stoichiometric changes (e.g., variation of O_2 level) of the ceramic as a result of elevated temperature exposure. In the present work, the variation of oxygen concentration could not be confirmed due to the inability of SEM-X-EDS to quantify O_2 .

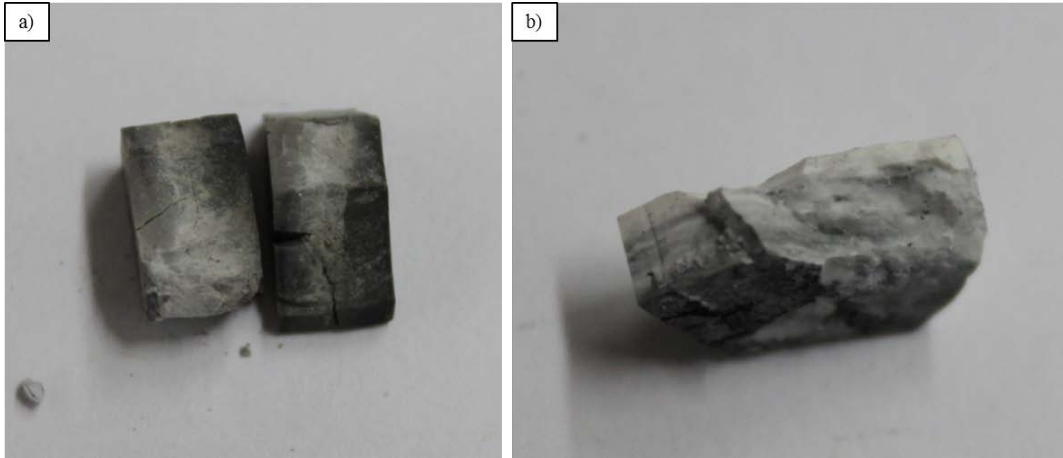


Figure 4.3: Discoloration of the fracture planes seen in the as-sintered YSZ discs: a) Sample 2 and b) Sample 4.

Several samples retained their integrity after ejection from the sintering dies. Six samples, sintered at varying sintering parameters were therefore chosen for subsequent study of the effect of SPS process parameters on the densification behaviour of YSZ. The six samples considered have been further classified into two groups. The first group (Group 1) of three samples were sintered at 1300°C and 30MPa with a cooling rate of 170°C/min. The second group (Group 2) of three samples was sintered at 1400°C and higher pressure of 50MPa, and cooled at a lower cooling rate of 100°C/min. The following table summarizes the processing parameters of the six samples considered. For each of the parameter conditions listed in Table 4.3, three or four repeats were made. It was seen that for all the repeats of the samples were highly comparable.

Table 4.3: Process parameters of the YSZ samples considered.

Sample No.		Heating Cycle				Cooling Cycle
		600°C	1000°C	1300°C	1400°C	Cooling Rate
Group 1	Sample 1	3mins; 0MPa	3mins; 30MPa	3mins; 30MPa	—	Ambient cooling
	Sample 2	3mins; 30MPa	—	3mins; 30MPa	—	Ambient cooling
	Sample 3	—	3mins; 30MPa	3mins; 30MPa	—	Ambient cooling
Group 2	Sample 4	3mins; 0MPa	—	—	3mins; 50MPa	100°C/min
	Sample 5	3mins; 0MPa	—	—	7mins; 50MPa	100°C/min
	Sample 6	3mins; 0MPa	—	3mins; 50MPa	—	100°C/min

The instantaneous density of these samples during the sintering process was calculated from the ram position and the theoretical density of YSZ as was described in Section 3.3.2 and is discussed in the following sections.

4.2.1 Densification of Samples Sintered at 1300°C (Group 1)

Figure 4.4 shows the densification behaviour of the YSZ samples sintered at 1300°C. Samples 1 and 3 had an intermediate 3 minute dwell at 1000°C. Sample 2 was heated directly to 1300°C and densified at a fast rate.

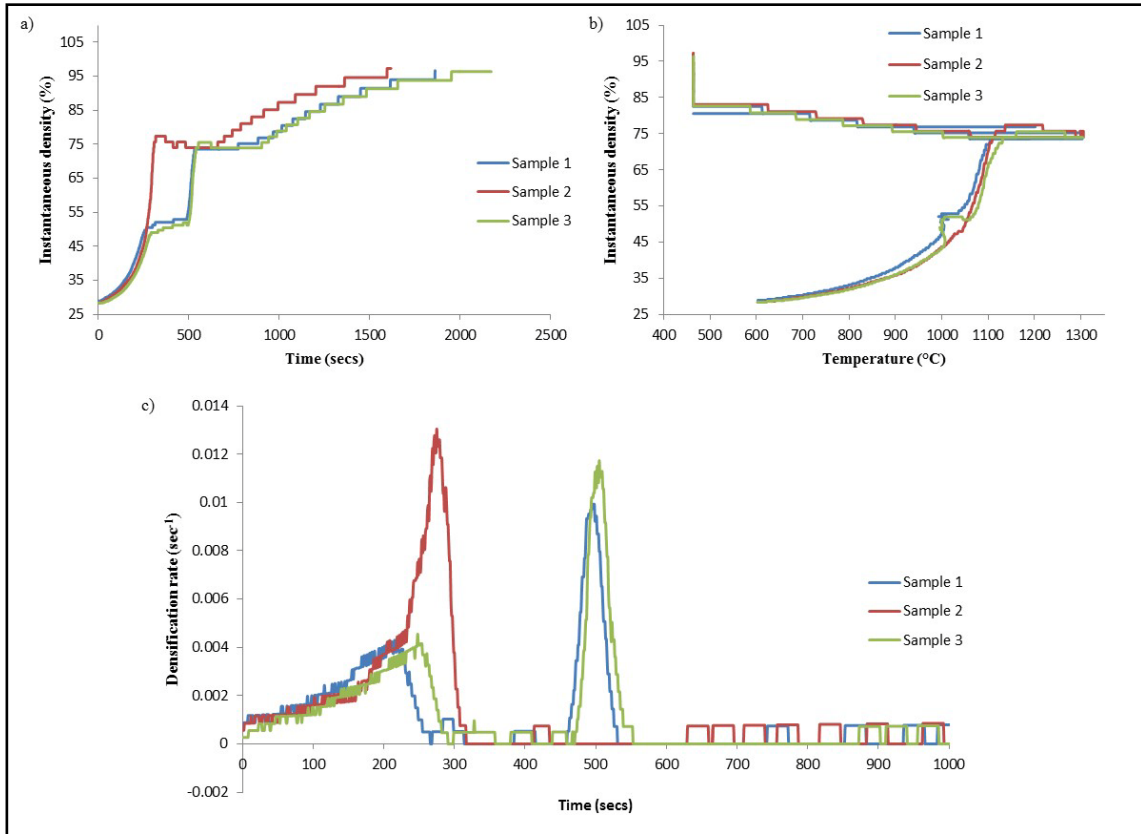


Figure 4.4: Densification curves of the YSZ samples sintered at 1300°C (Group 1): a) Instantaneous Density vs Time; b) Instantaneous Density vs Temperature; c) Densification rate vs Time.

All samples attained $\sim 75.6 \pm 2.5\%$ density at the end of the sintering dwell time. Additional densification of the samples during the cooling cycle was seen in the instantaneous density vs temperature plots (Figure 4.4b) and Table 4.4.

Table 4.4: Relative density of Group 1 YSZ samples (w.r.t. theoretical density of YSZ) during SPS cycle.

Sample No.	Density at the end of sintering dwell time (%)	Density at room temperature (%)	Increase in Density during cooling (%)
Sample 1	73	96	23
Sample 2	79	97	18
Sample 3	75	96	21

From Table 4.4, it can be seen that all the samples densified during the cooling cycle to a comparable extent. As the instantaneous density of the samples is estimated as a function of the ram position, the increase in the density of the samples during the cooling was possibly a consequence of: a) volumetric shrinkage of the samples during the cooling from high temperature to room temperature; or b) phase transformation in the YSZ matrix e.g. from tetragonal to monoclinic phase.

The XRD results in Figure 4.5, revealed that a phase transformation from tetragonal to monoclinic during the sintering process indeed occurred. For all three samples, a peak at 85° diffraction angle was observed and was associated with the monoclinic ZrO₂ lattice. For samples 1 and 3, which were dwelled at 1000°C, higher intensity monoclinic phase peaks was seen as compared to sample 2. Thus, a phase transformation from tetragonal to monoclinic during the sintering process likely occurred and contributed to the ceramic's volumetric change.

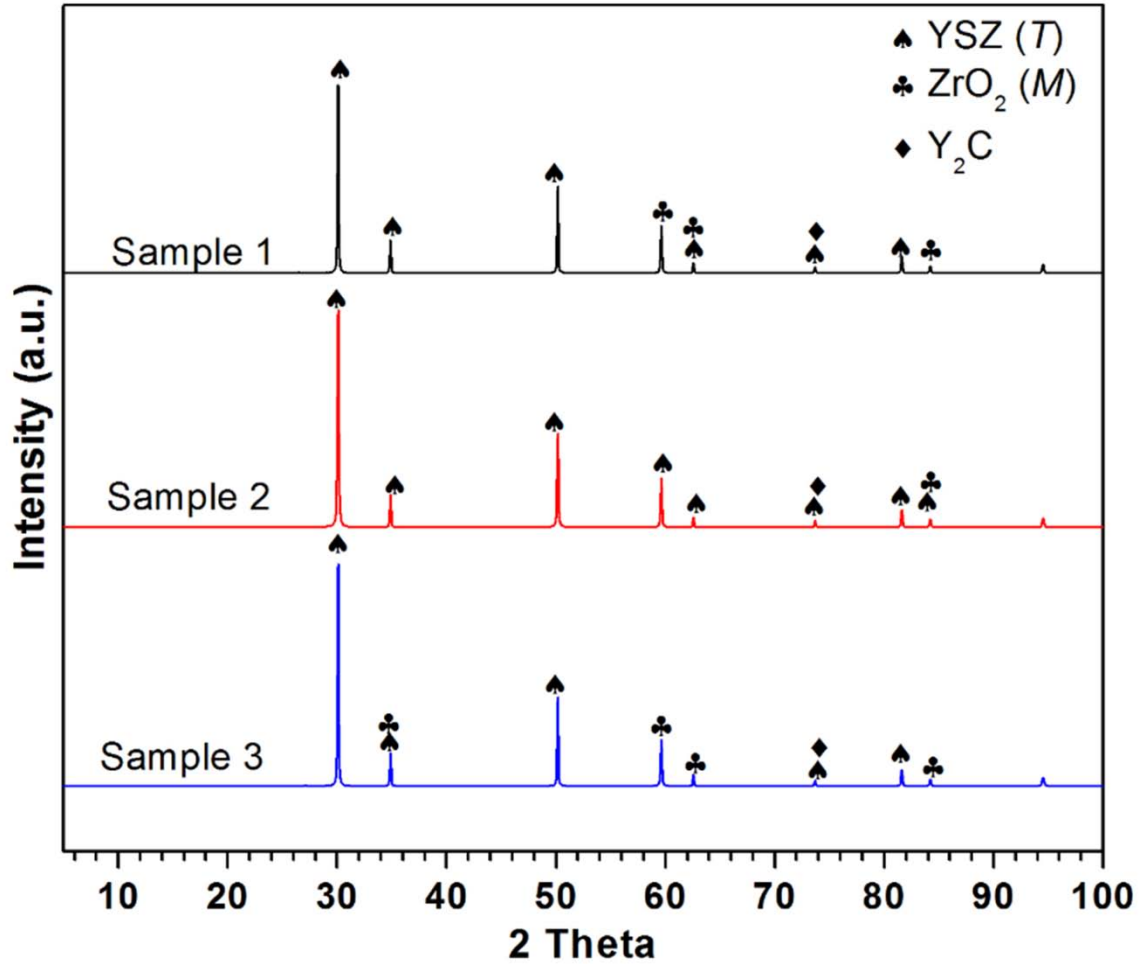


Figure 4.5: XRD analysis of the as-sintered Group 1 YSZ samples, sintered at 1300°C
(T: Tetragonal, M: Monoclinic).

Granger *et al.* [65] reported that the densification of YSZ occurs by a combination of grain boundary sliding due to particle rearrangement and subsequent lattice diffusion/grain growth. This can be seen in the double peak nature of the densification rate curves, as observed in Figure 4.4c. For samples 1 and 3, the two peaks were seen to be very distinct and were separated by ~200 second time delay. The first peak was seen to initiate at ~ 600°C, while the second peak at ~1000°C, which is consistent with the work of Tamburini *et al.* [64] who reported that the densification by particle rearrangement in YSZ occurs at low temperatures

(~600°C), while the densification by diffusion/grain growth is active above 800°C. In contrast, for sample 2, the two densification rate peaks overlapped, suggesting the simultaneous occurrence of the two processes (particle rearrangement and diffusion) may have initiated.

Figure 4.6 shows the thickness measurements of the YSZ samples. Sample 2 had the lowest thickness in comparison to samples 1 and 3. Comparing the density of the samples (see Table 4.4) with their corresponding thickness, it can be seen that the samples 1 and 3, had the same density (96%) and a similar thickness (~3.54mm). On the contrary, sample 2 had a relatively higher density (97%) corresponding to a lower thickness.

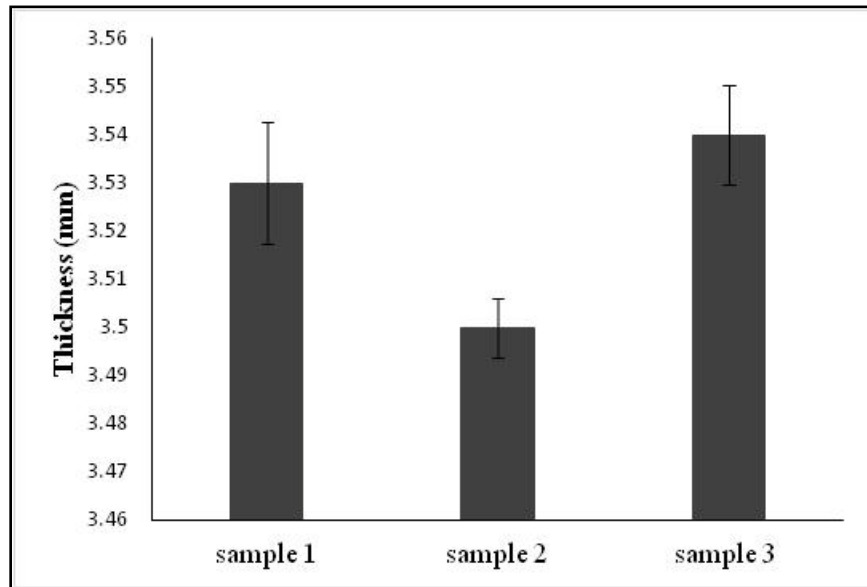


Figure 4.6: Thickness of the as-sintered YSZ discs (Group 1).

To further analyze the effect of the sintering parameters on the densification behaviour of the samples, grain size and microstructural analysis via SEM was carried out. The SEM images of the as-sintered discs, on the surfaces of the samples revealed that the grains were covered by a thick glassy phase, as shown in Figure 4.7. This glassy phase was present in the bulk of

the sample as well. The grain structure was not clearly visible because of the presence of the glassy layer, as can be seen in Figure 4.8. This glassy phase seemed to be amorphous in nature.

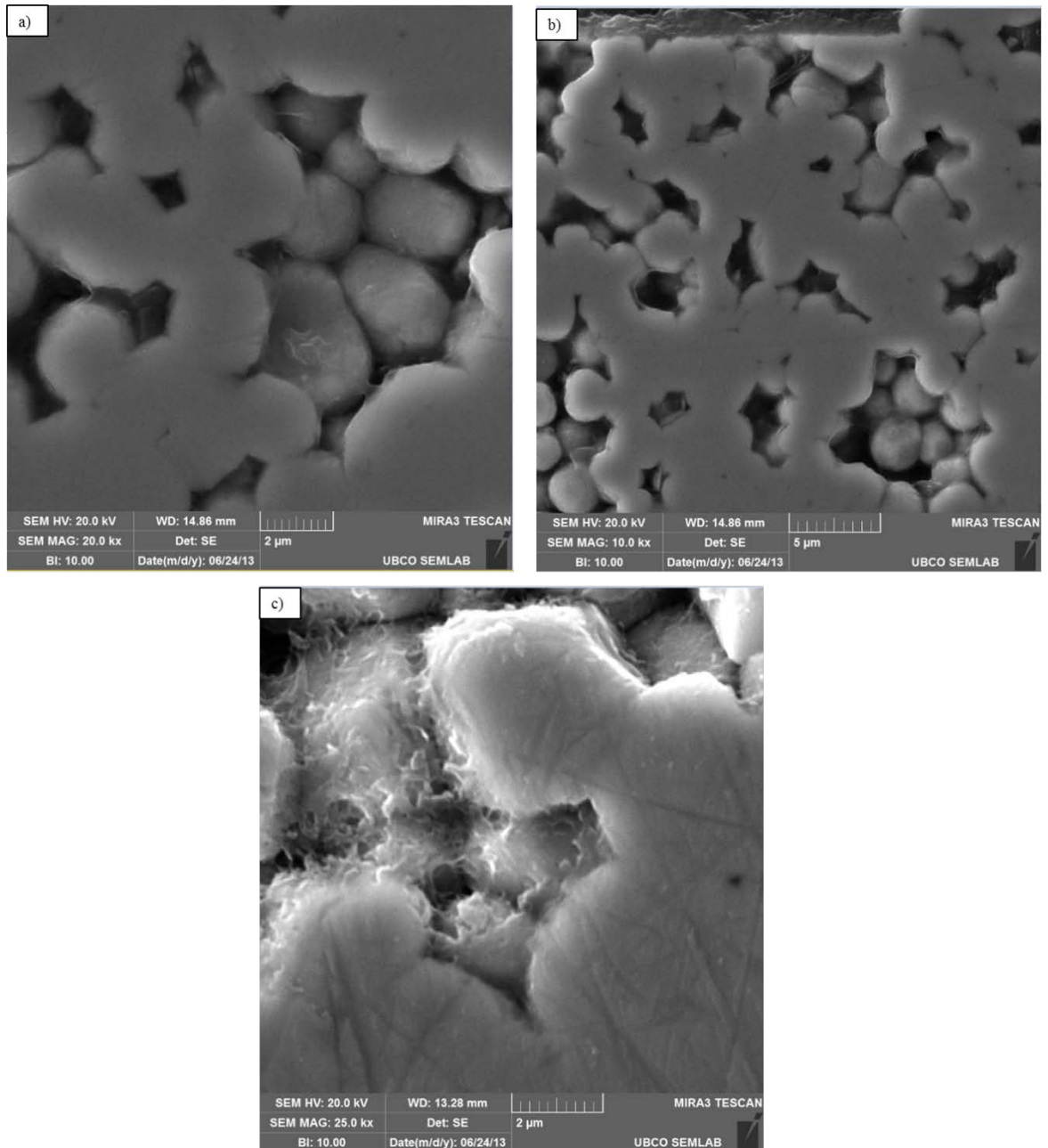


Figure 4.7: SEM images of the polished surfaces of the as-sintered Group 1 YSZ discs: a) Sample 1; b) Sample 2 and c) Sample 3.

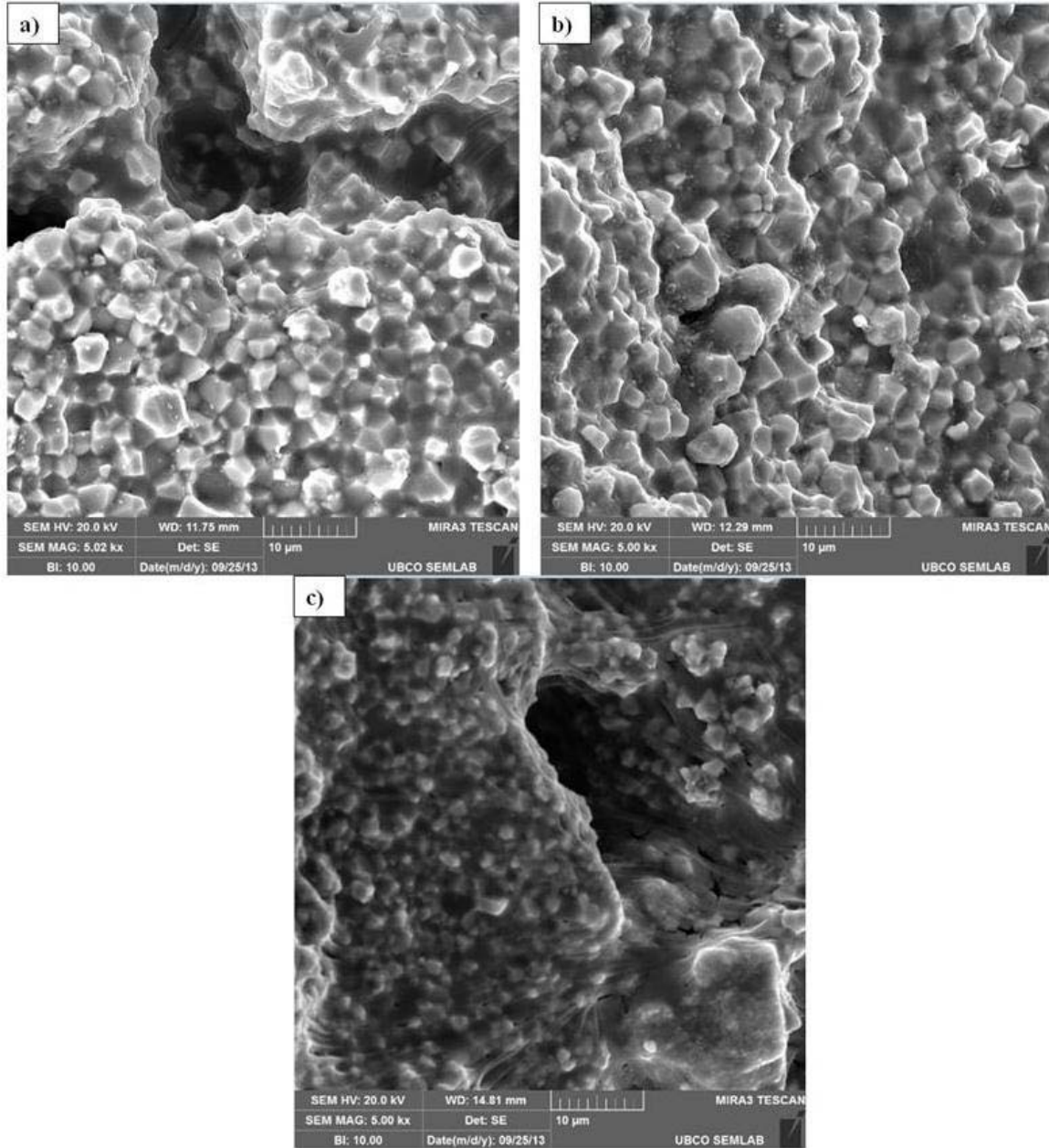


Figure 4.8: SEM images of the glassy phase present along the grain boundaries of the as-sintered Group 1 YSZ discs: a) Sample 1; b) Sample 2 and c) Sample 3.

The glassy phase along the grain boundaries of all YSZ samples likely contributed to the fragmentation of all as-sintered samples, as seen in macro images in Figure 4.8. X-EDS

chemical analysis was performed on the glassy phase, as shown in Figure 4.9 which revealed a high concentration of Cl and Y (Table 4.5).

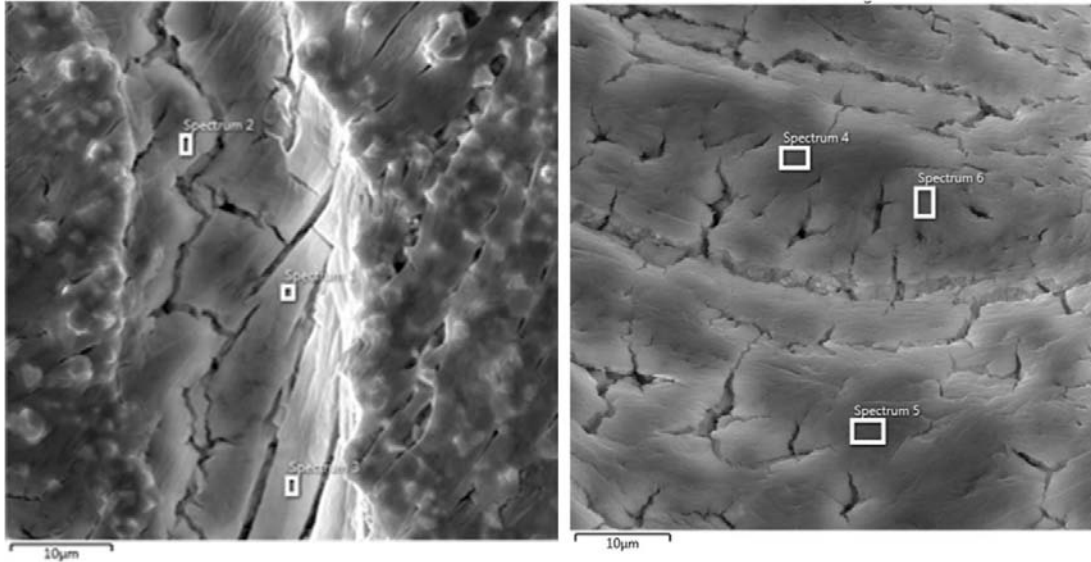


Figure 4.9: X-EDS spectrum sites on the glassy phase of Sample 3.

Table 4.5: X-EDS spectrum values of the glassy phase from Figure 4.9.

Element	Concentration (wt%)						Average
	Site 1	Site 2	Site 3	Site 4	Site 5	Site 6	
Y	39.1±1.7	36.8±1.7	38.1±1.9	36.9±0.3	37.0±0.3	40.3±0.3	38.0±1.03
Cl	29.0±1.3	31.5±1.4	29.7±1.5	34.9±0.3	34.7±0.3	39.4±0.3	33.2±0.85
C	24.9±3.3	23.1±3.4	24.8±3.6	28.2±0.4	28.3±0.4	20.3±0.4	24.9±1.9
O	7.1±0.5	8.6±0.5	7.4±0.5	0	0	0	7.7±0.5

As can be seen from the Table 4.5, the glassy phase was depleted in zirconia and rich in yttria and chlorine, carbon and oxygen. Small traces of Cl were also found in the raw powders (Table 4.1). These results suggest that possibly an Yttrium Chloride (YCl) phase may have

formed during the sintering process. Roesler *et al.* [66] reported that in most sintering practices, sintering aids are added to the powders to facilitate the fusion of the grains. These sintering aids often contribute to the formation of an amorphous glassy phase at the grain boundaries. Since the glassy phase likely had a lower softening temperature compared to the matrix grains, cracking and failure of the ceramic was observed [66].

The glassy phase in this work was seen to have similar traits to the sintering aids used in conventional sintering. The melting point of YCl is 721°C, with a density of 2.6g/cm³ [67], while the density of YSZ is 6.01 g/cm³. This suggests that thermally induced buoyancy flow of the YCl salt to the surface layers of the YSZ grains may have occurred. The cracks were seen to propagate through the glassy phase, as seen in Figure 4.10.

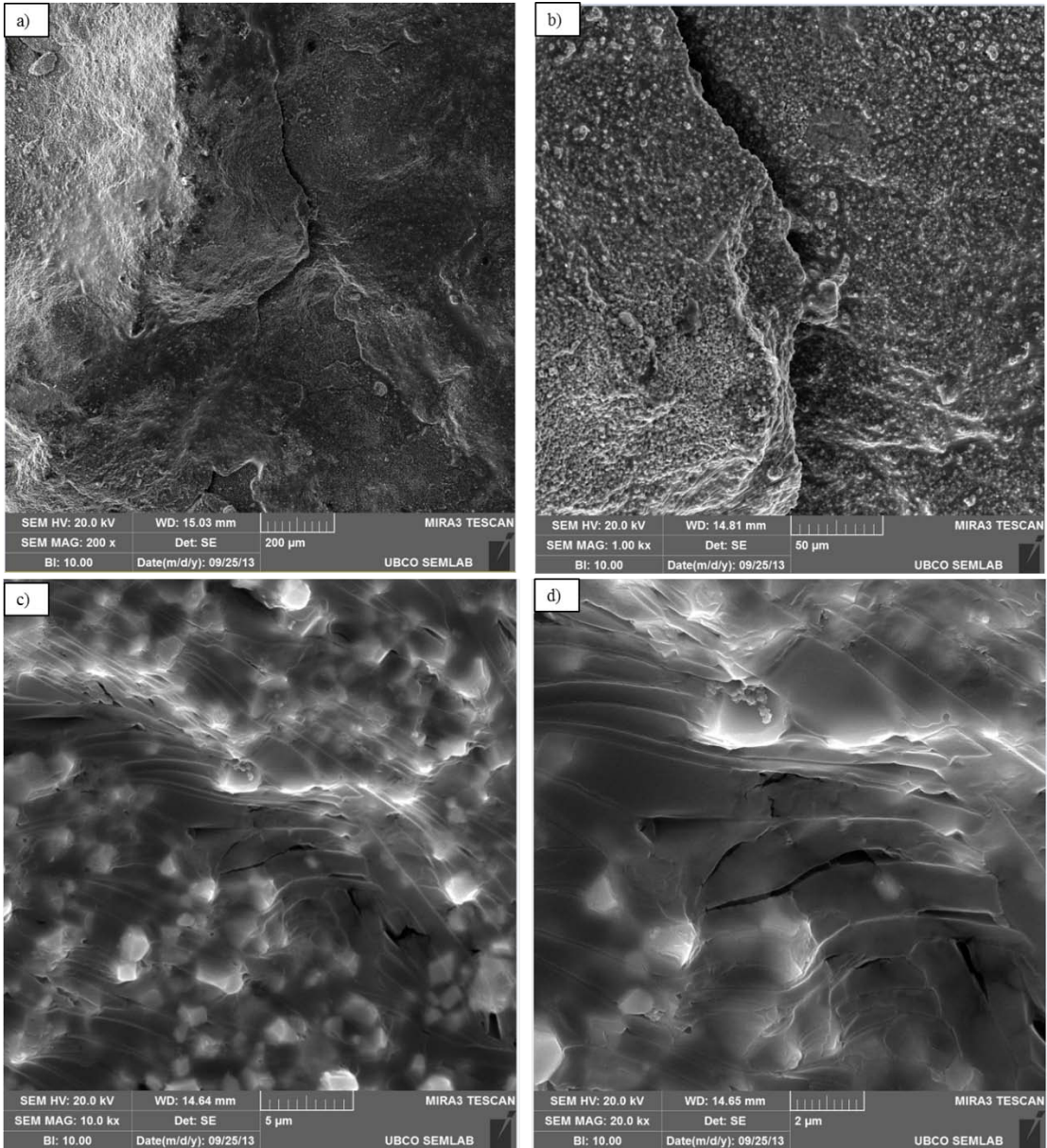


Figure 4.10: Glassy phase on the grain boundaries with crack propagating through the glassy layer. Sample 1 at: a) 200x and b) 1,000x magnifications; Sample 3 at: c) 10,000x and d) 20,000x magnification.

In order to reveal the grain structure of the ceramic, the samples were heat treated to 50°C below the sintering temperature and dwelled for 1 hour (in ambient atmosphere). The grain structure of the heat treated samples 1, 2 and 3 can be seen in Figure 4.11.

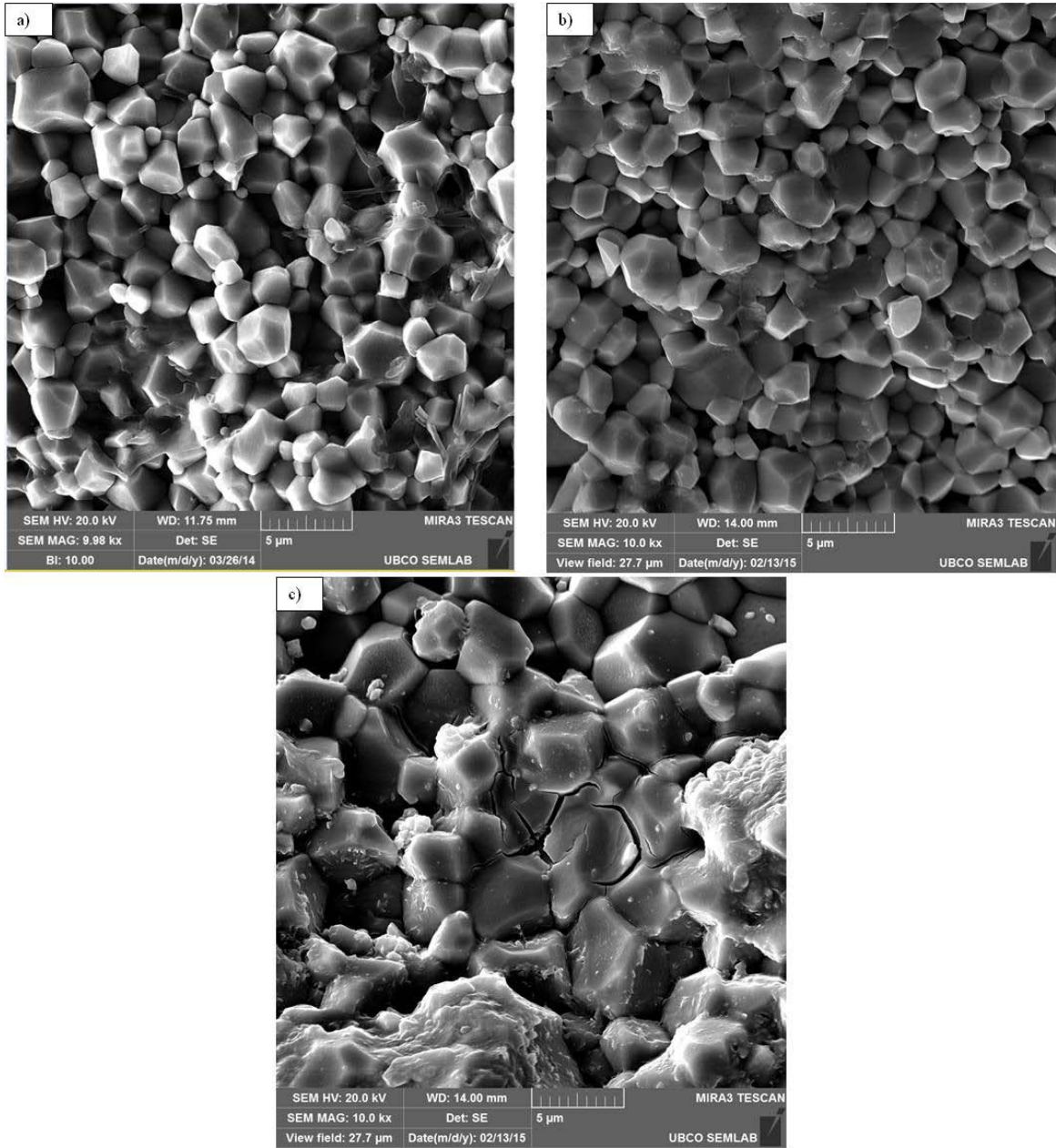


Figure 4.11: SEM images of the fracture surfaces of the heat treated samples (Group 1):

a) Sample 1; b) Sample 2; c) Sample 3.

The grain size measurements revealed that sample 2 had the smallest grains with an average grain size of $\sim 1.5\mu\text{m}$, as shown in Figure 4.12. As discussed earlier, during the densification process, sample 2 underwent simultaneous particle rearrangement and grain

growth/diffusion. Due to this simultaneous effect, the particles in sample 2 restricted each other's growth and thus were closely packed. Also, the grains in this sample grew more uniformly, which can be seen from the lower standard deviation in the grain size measurements, compared to that of samples 1 and 3.

For samples 1 and 3, the particle rearrangement was followed by grain growth leading to non-homogenous powder particle size distribution and non-homogenous grain growth, as can be seen from the higher standard deviations in Figure 4.12 and also microstructure observation.

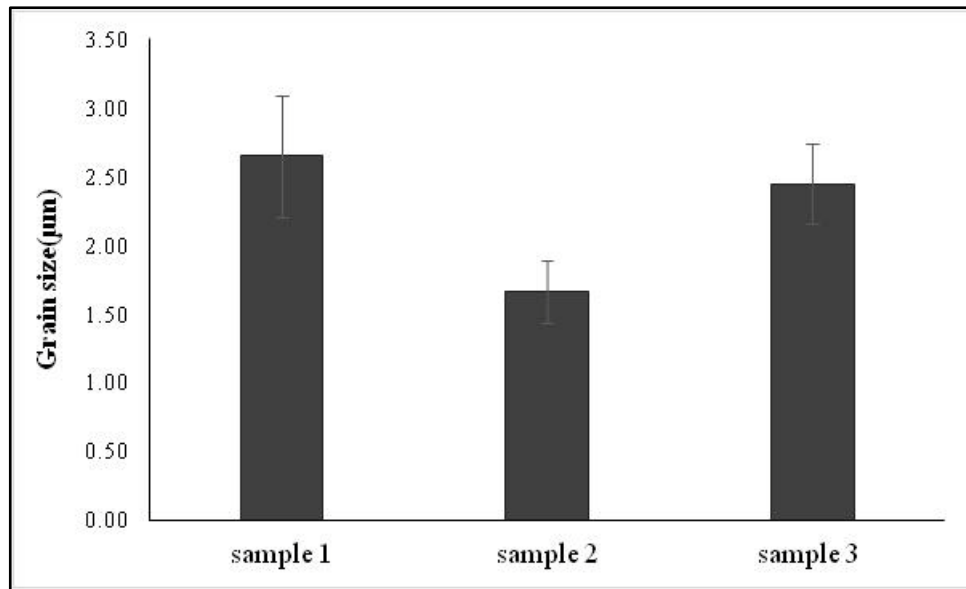


Figure 4.12: Grain size measurements of the samples sintered at 1300°C (Group 1).

4.2.2 Densification of Samples Sintered Under 50MPa Pressure (Group 2)

All the samples of this group were initially dwelled at 600°C for 3minutes, before dwelling at their respective sintering temperatures. Also, the effect of slow cooling on the densification of the samples was investigated in this group of samples.

Figure 4.13 shows the densification curves of the samples sintered at 1400°C (samples 4 and 5) and 1300°C (sample 6) under 50MPa load. The samples had an initial green density of ~28%. As can be seen from Figure 4.13a, sample 6 had a lower density compared to samples 4 and 5, which was contributed to the lower sintering temperature. It was seen that elevating the sintering temperatures lead to an increase in the density of the samples. Similar to the samples of group 1, sample 6 also had an instantaneous density of ~75% at the end of the sintering dwell time, while samples 4 and 5 had a higher density of ~85% (see Table 4.6). This indicates that the increase in the pressure from 30 to 50MPa had a lower effect on the densification of the samples, while increasing the sintering temperature had a significant effect on the densification.

An increase in the density of the samples was seen during the cooling cycle as seen in Figure 4.13b and Table 4.6. Unlike the samples in group 1, the samples in group 2 were cooled at a controlled rate of 100°C/min. It can be seen from Table 4.6 that the increase in the density of the samples under controlled slower cooling rate was only marginally lower than that seen under ambient cooling rate condition.

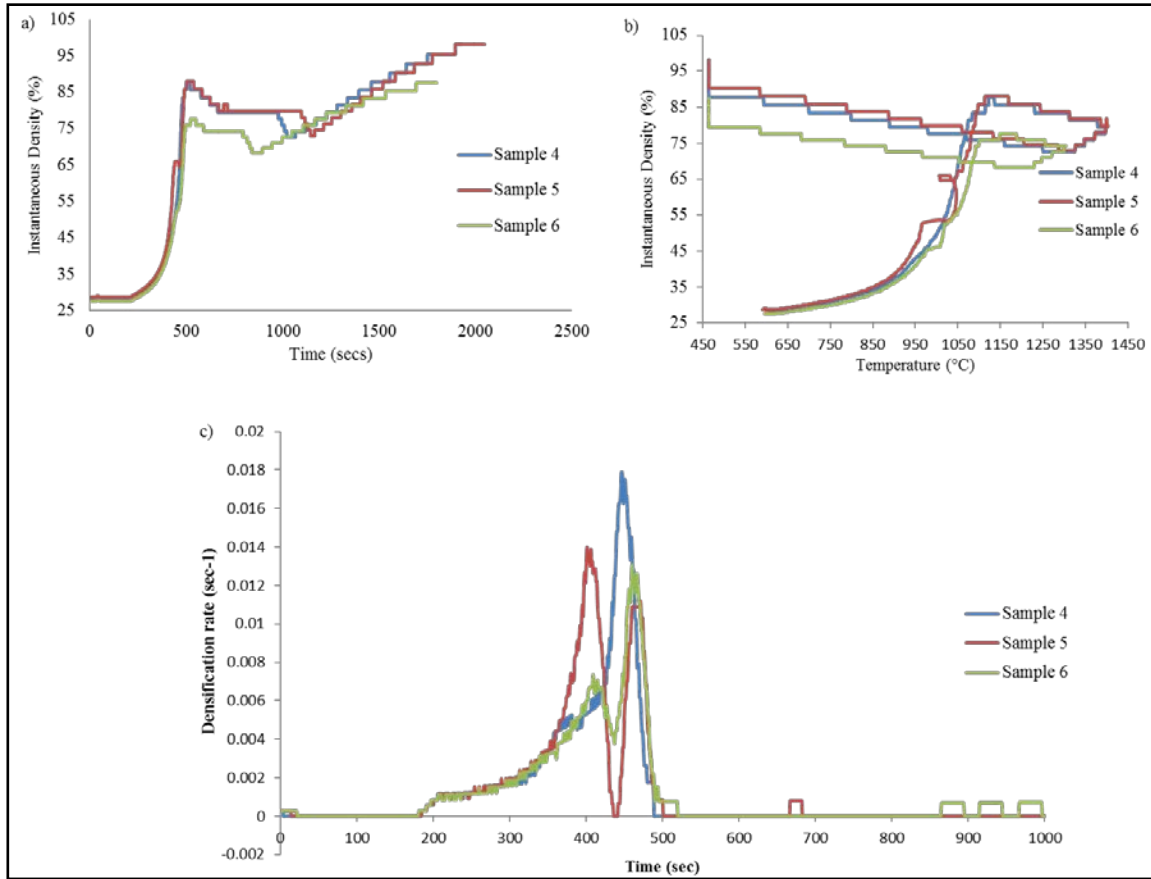


Figure 4.13: Densification curves of the YSZ samples sintered under 50MPa pressure (Group 2):

a) Instantaneous Density vs Time; b) Instantaneous Density vs Temperature;

c) Densification rate vs Time.

Table 4.6: Relative density of Group 2 YSZ samples (w.r.t. theoretical density of YSZ) during SPS.

Sample number	Density at end of sintering dwell time (%)	Density at the end of the cooling (%)	Increase in density during cooling (%)
Sample 4	83	98	15
Sample 5	81	98	17
Sample 6	73	87	15

Figure 4.13c shows the densification rate curves for the samples. It was seen that for sample 4, the particle rearrangement and the grain growth peaks occurred simultaneously unlike for sample 5 and 6. Similar to sample 2, in sample 4 the grains were more closely packed thereby resulting in a relatively higher density and lower thickness of the disc, as shown in Figure 4.14 and Figure 4.15

Figure 4.14 shows the final (room temperature) density of the as-sintered materials. Samples 4 and 5 had the same density of 98% theoretical density (5.89g/cm^3). Sample 4 was dwelled at the sintering temperature (1400°C) for 3 minutes, while sample 5 was dwelled for 7 minutes at the sintering temperature of 1400°C . However, sample 5 was seen to have the same final density of 98%TD as sample 4. Therefore, the extended dwell time for sample 5 did not show any influence on the final density of the sample. This is in accordance to the results reported by Tamburini *et al.* [64].

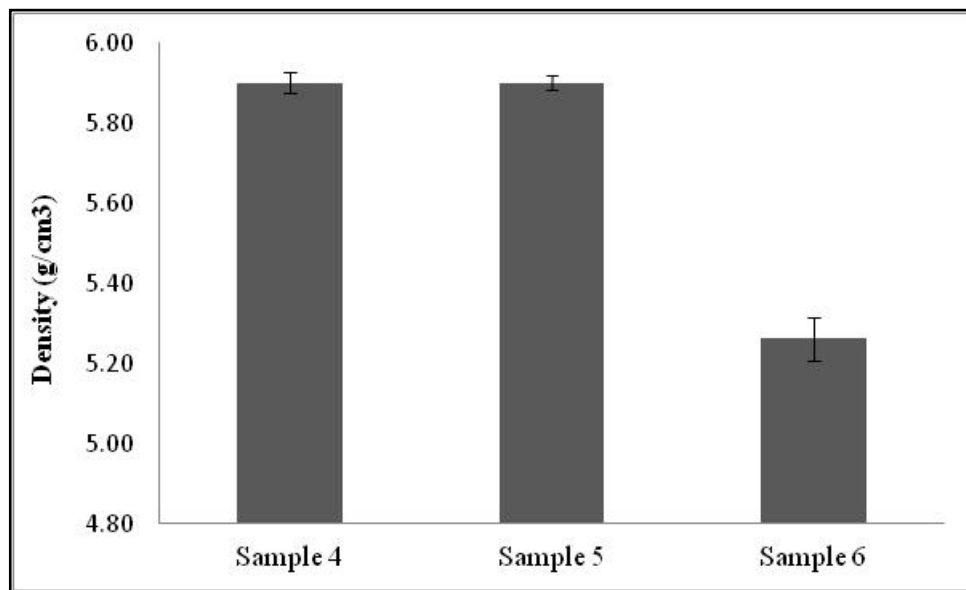


Figure 4.14: Density of the samples sintered under 50MPa pressure (Group 2).

The thickness measurements of the samples revealed that sample 6 had a higher thickness than samples 4 and 5, as seen in Figure 4.15. The instantaneous density curves also depict that sample 6 had the lowest density at the end of the sintering dwell time.

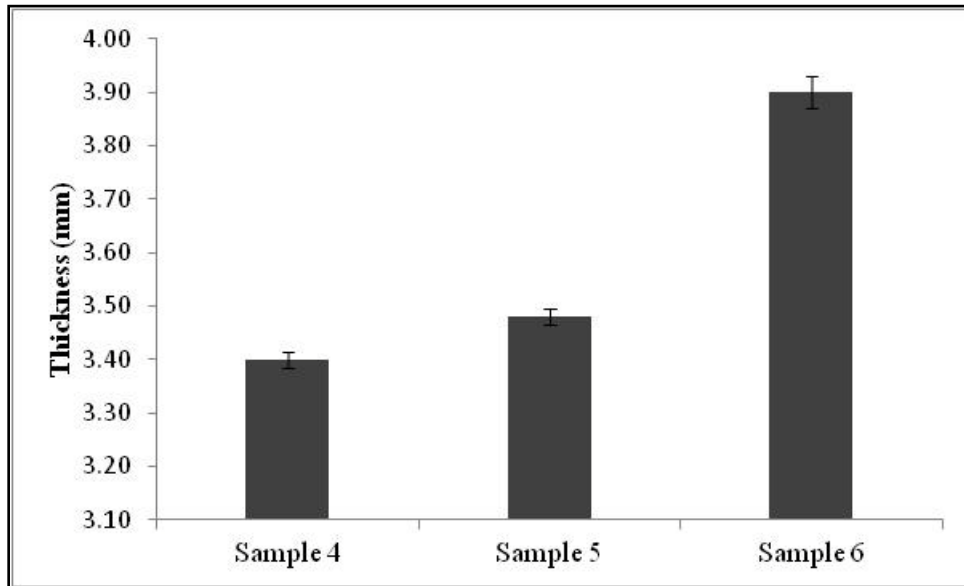


Figure 4.15: Thickness measurements of the as-sintered YSZ samples (Group 2).

XRD analysis revealed tetragonal to monoclinic transformations occurred for Group 2 samples as well, as seen in Figure 4.16. It was seen that sample 6 had the maximum amount of monoclinic phase, which could be one of the underlying reasons for the increased thickness and low density of the sample.

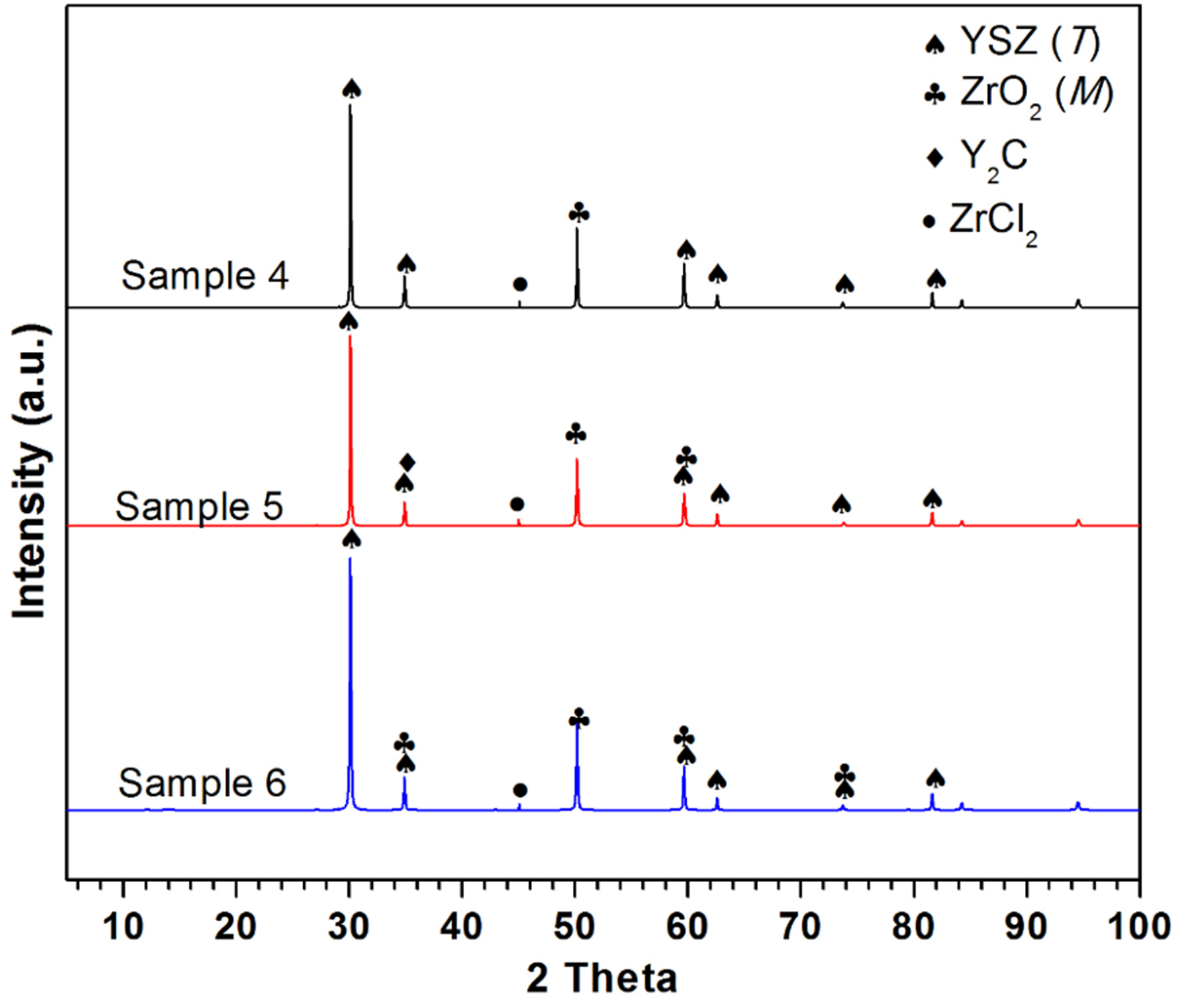


Figure 4.16: XRD analysis of the as-sintered Group 2 YSZ samples, sintered under 50MPa pressure (T: Tetragonal, M: Monoclinic).

The grain size measurements of the samples (Figure 4.17) revealed that the sample 6 had the largest grains and sample 5 had the smallest grains. Comparing the densification rate curve (Figure 4.13) with the grain size measurement of sample 5, it is seen that the low grain size of the sample 5 was a result of the higher particle rearrangement peak.

From the SEM images shown in Figure 4.18, it was observed that sample 4, which was dwelled for 3 minutes, did not exhibit any glassy phase along the grain boundaries. However,

increasing the dwell time to 7 minutes in sample 5, formation of the glassy phase along the grain boundaries was observed.

The standard deviation of the grain size measurements for sample 5 was greater than that of sample 4. This grain size variation could be indication of the formation of new grains, as shown in Figure 4.19a (marked with arrows).

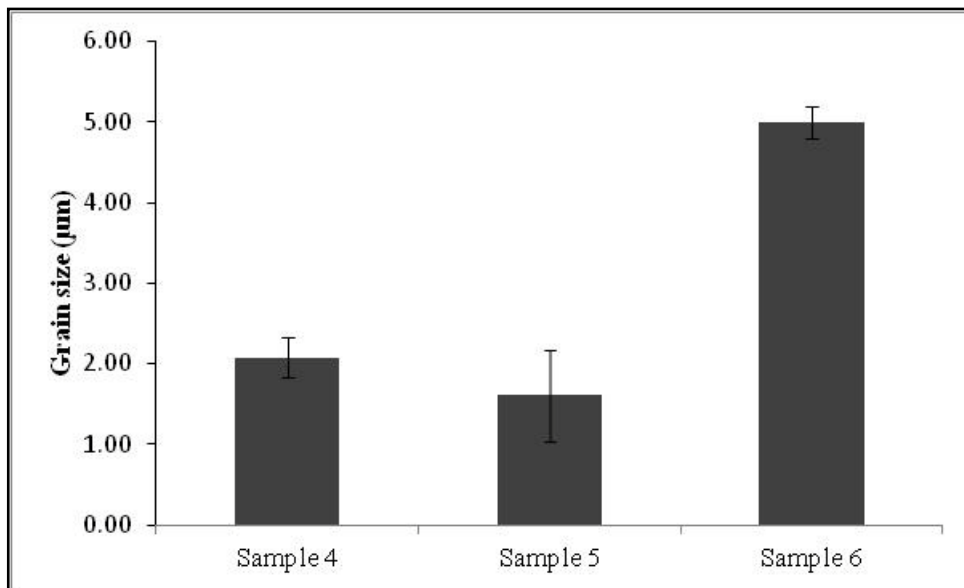


Figure 4.17: Grain size measurements of the samples sintered under 50MPa pressure (Group 2).

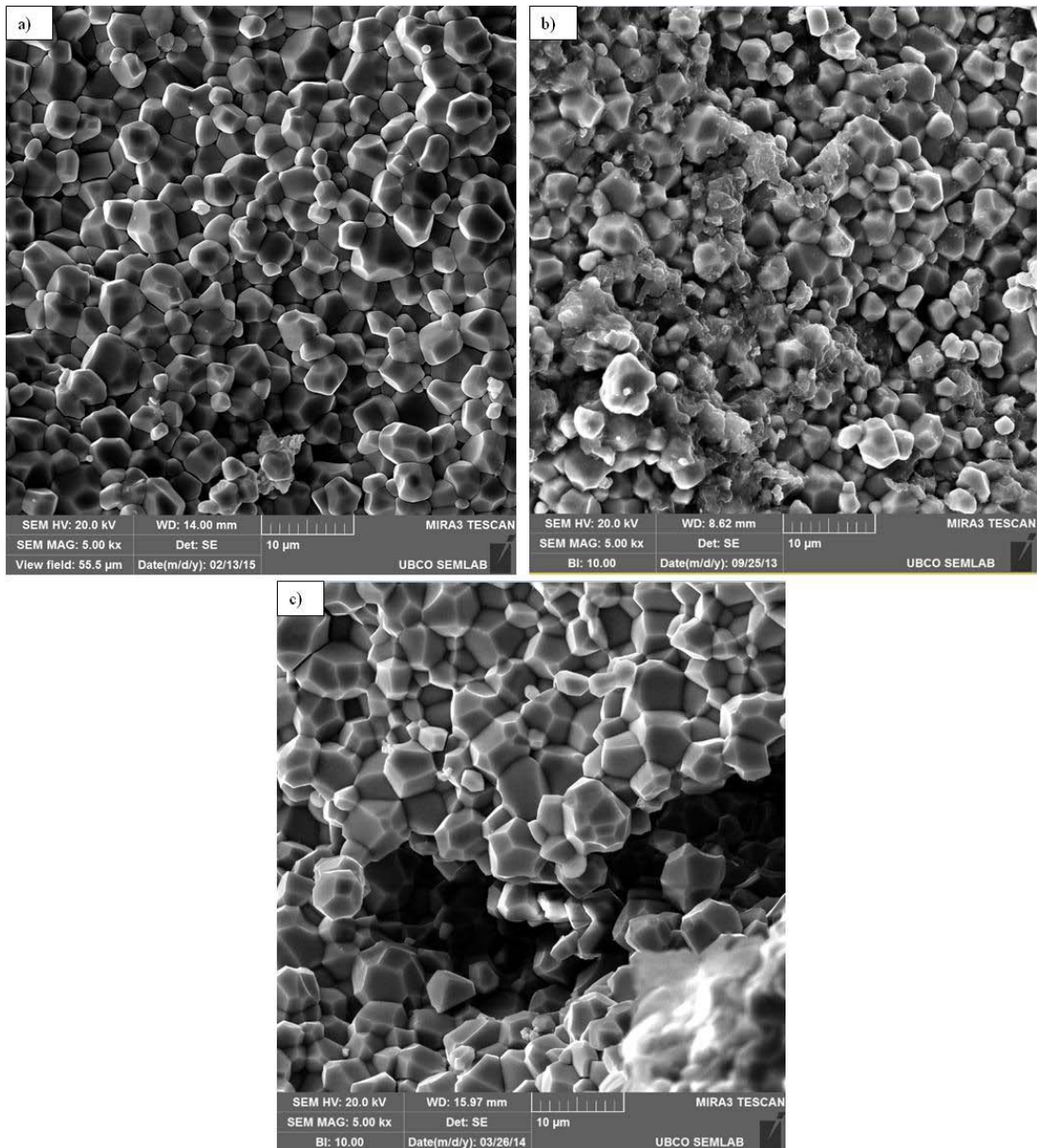


Figure 4.18: SEM images of the fracture surface of the samples (Group 2):

a) Sample 4; b) Sample 5 and c) Sample 6.

Figure 4.19a reveals that the small grains formed at the grain boundaries of larger grains, and these new grains were smaller than the starting powder particles. Thus, these grains possibly formed during the sintering process.

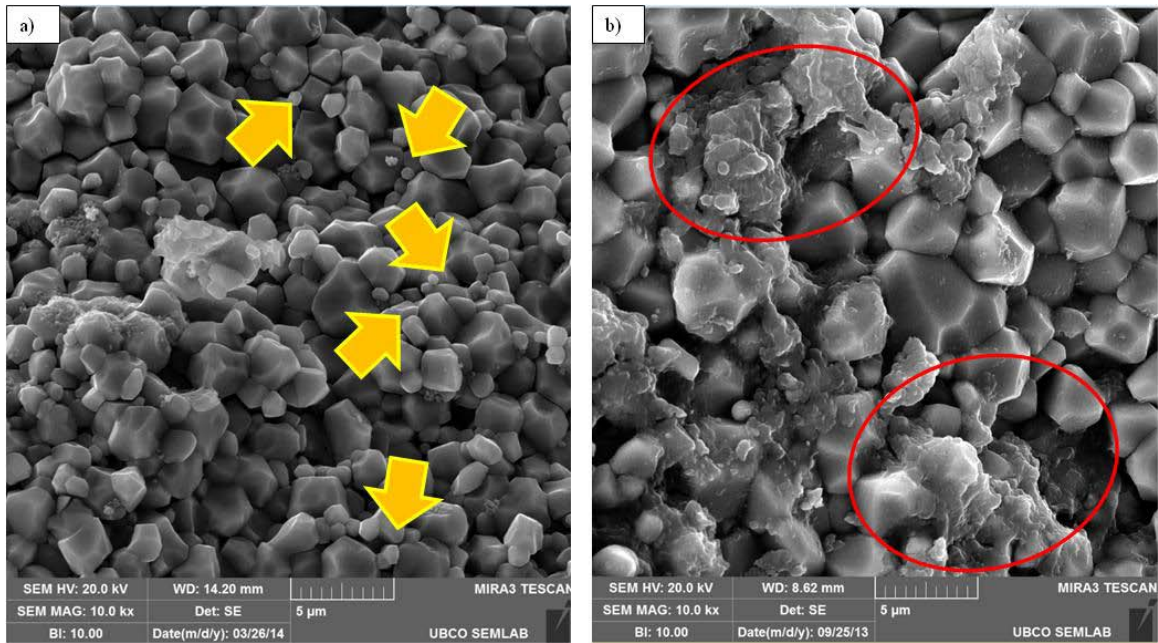


Figure 4.19: a) Smaller grains seen along the grain boundaries of larger grains (indicated by arrows) and b) Initiation of the glassy phase along the grain boundaries (encircled) in sample 5.

In Figure 4.19b, it can be seen that the grains of sample 5 are faceted, and, the surfaces seem to have a molten appearance. Since the melting point of YSZ (~2500°C, as seen in Figure 2.1) is greater than the sintering temperature, there was a possible occurrence of glassy phase formation.

For sample 6, it was seen that a thin, but consistent film of a glassy phase was covering the grains. Similar to the observations seen in group 1 samples, the X-EDS of the glassy phase indicated the presence of Yttria, Chlorine, Carbon and Oxygen. At some sites the grains could not be seen due to the thick and opaque nature of the glassy phase. The disintegration of the samples was along the glassy phase. As reported by Roesler *et al.* [66], crack propagation in ceramic materials was seen to relate to the presence of amorphous films (i.e., a glassy phase), as seen in Figure 4.20.

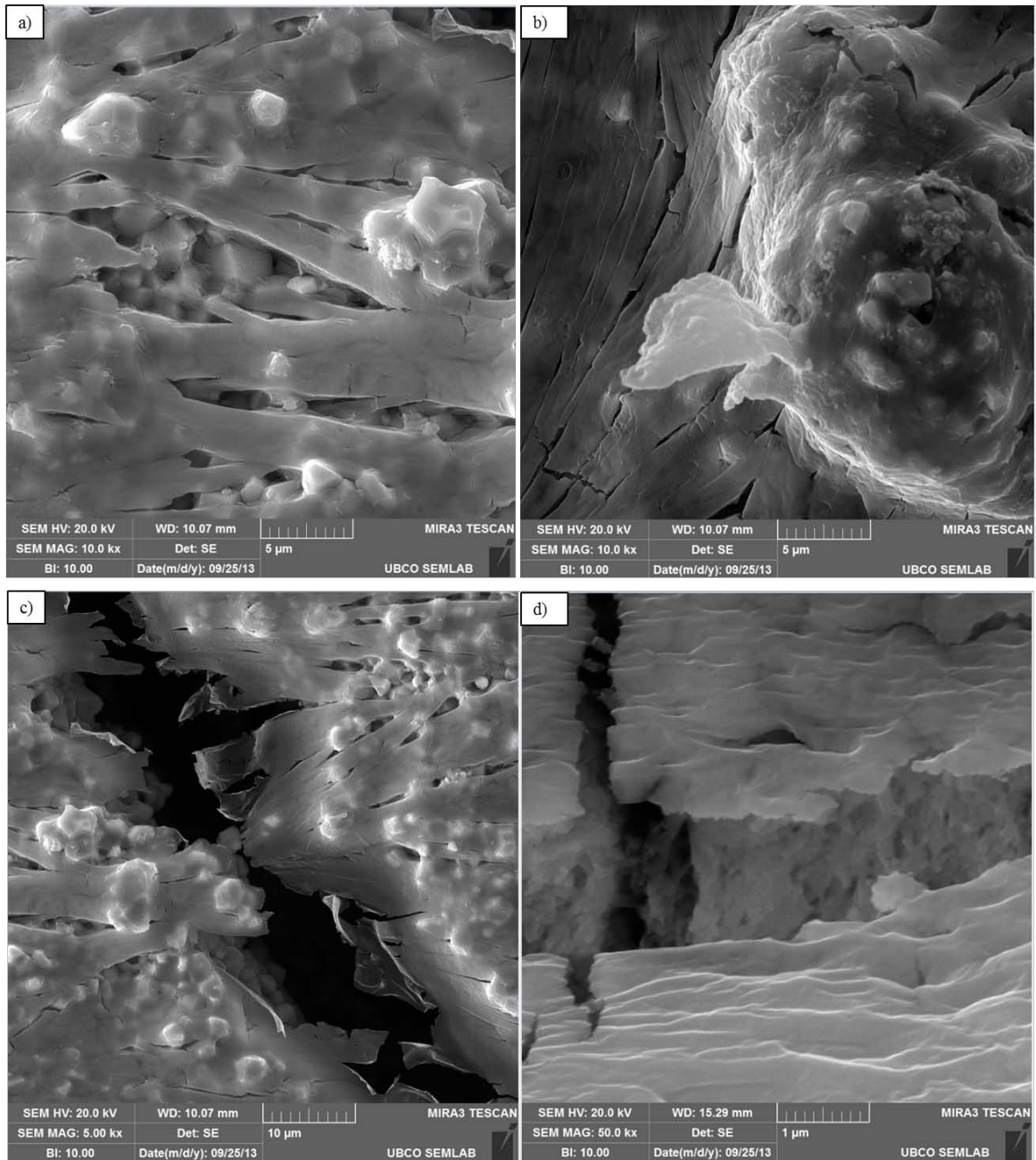


Figure 4.20: Glassy phase covering the grains of sample 6, and crack propagation seen along the glassy phase at four different sites, a); b); c); and d).

4.3 Processing and Characterization of CNT-YSZ Ceramic Composites

4.3.1 Synthesis and Densification Behaviour of the SWCNT-YSZ Ceramic Composites

All sintering experiments were carried out in Ar atmosphere to prevent damage to the SWCNTs during processing based on the work with plain YSZ (Section 4.2.). All sintering experiments were performed at 30MPa pressure and a 5 minutes dwell time at 1300°C. A heating rate of 100°C/min to 1300°C, and a cooling rate of 170°C/min after sintering were imposed for all experiments. These sintering parameters were selected based on the observations of the work done in Section 4.2.

Examining the grain boundary regions of the SWCNT-YSZ ceramic composites, it was seen that the SWCNTs were present exclusively at the grain boundaries. The width measurement on the SWCNTs before and after sintering revealed that the width of the SWCNTs increased from 20 to 25 ± 2.08 nm and no damage to the SWCNTs was observed. The SWCNTs along the grain boundaries are shown in Figure 4.21.

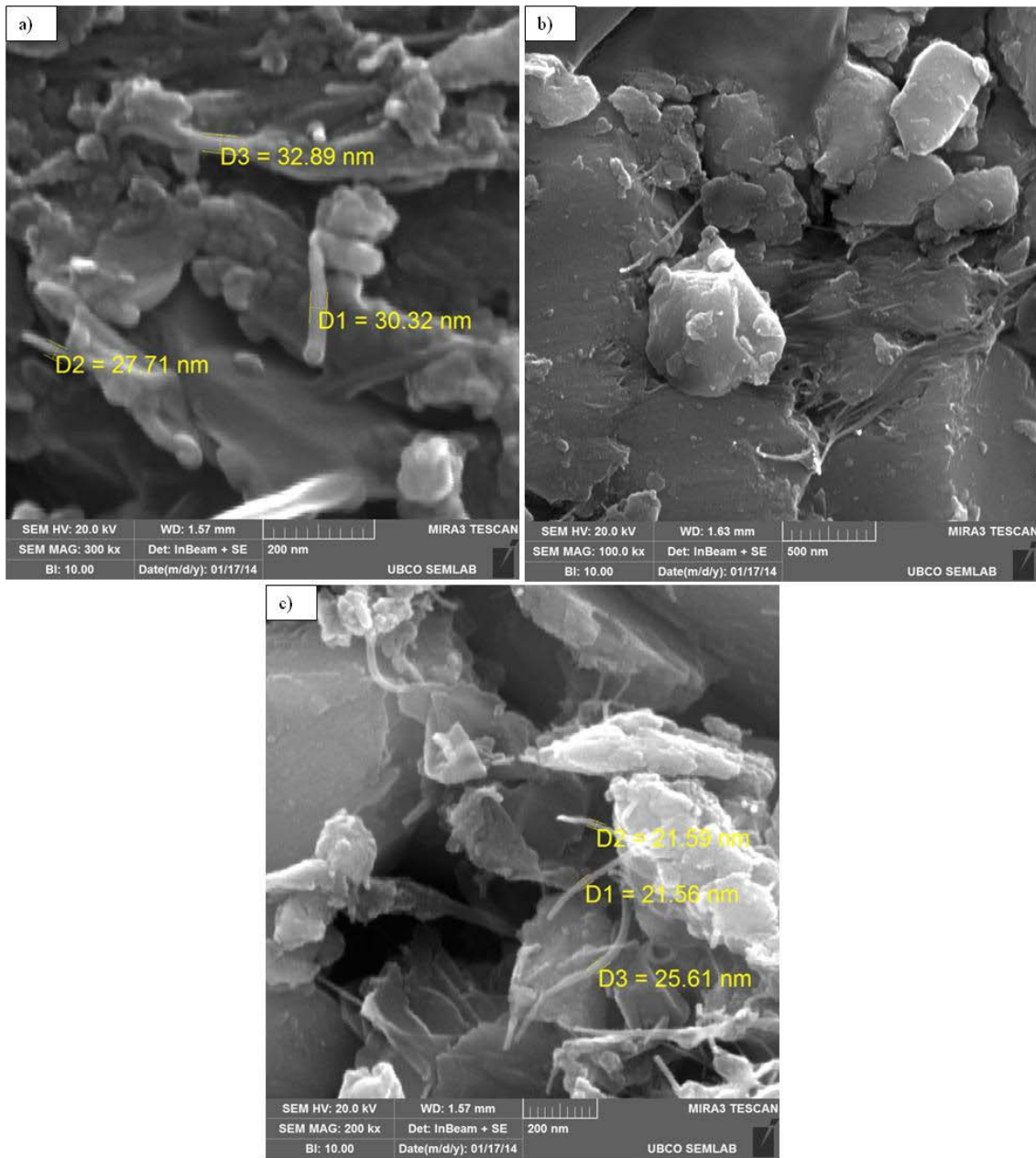


Figure 4.21: SWCNTs seen along the grain boundaries: a) 0.2wt% SWCNT-YSZ; b) 0.5wt% SWCNT-YSZ and c) 1wt% SWCNT-YSZ.

4.3.1.1 Effect of SWCNTs on the Densification Behavior of the Ceramic Composites

Figure 4.22 shows the densification plots of the SWCNT-YSZ ceramic composites. As can be seen from Figure 4.22a, the SWCNT containing powder blends had a lower green density than the plain YSZ after the 5MPa preload, since at $t = 0$ seconds the density of the green compacts progressively decreased from 37% (for pure YSZ) to 25% (for 1wt% SWCNT-YSZ). Thus, the addition of SWCNTs to the YSZ powder was seen to hinder compaction of the raw powders. Interestingly, the relative densities of the 0.2 and 0.5wt% SWCNT-YSZ composites were similar (33 – 35%). As can be seen in the Figure 4.22a and b, the densification behaviour of these two composites was also similar. In these two composites, the SWCNTs appeared to be well dispersed along the YSZ powder grain boundaries. In contrast, at the high doping level (1wt% SWCNT-YSZ), homogeneous dispersion of the SWCNTs was difficult and often resulted in the formation of agglomerates at the grain boundaries.

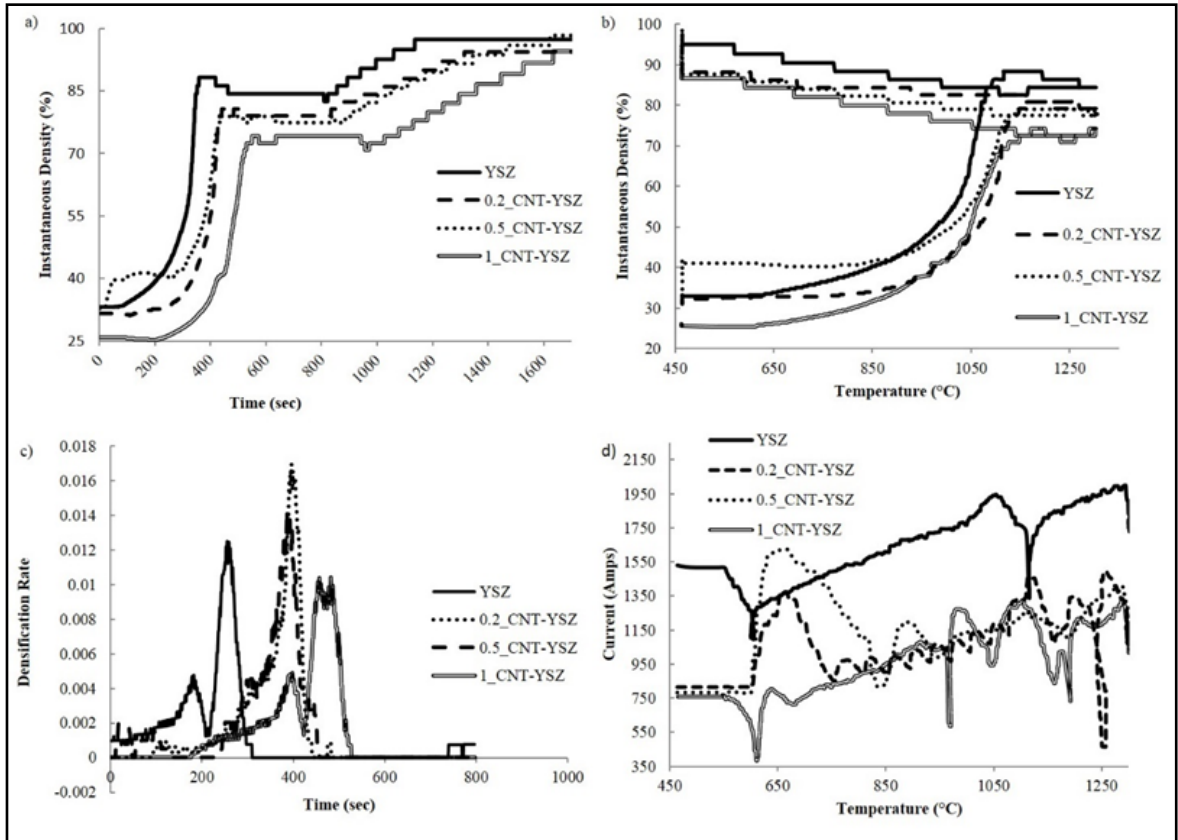


Figure 4.22: a) Instantaneous density vs Time; b) Instantaneous density vs Temperature; c) Densification rate vs Time and d) Sintering current vs Time plots of the SWCNT-YSZ ceramic composites.

Table 4.7 provides a summary of the density of the composite materials at the end of the sintering cycle (i.e., at the end of the 5 minute hold time at 1300°C and prior to cooling), as well as the density of the as-sintered disc after ejection from the SPS machine. From Table 4.7 and Figure 4.22b, it can be seen that the composites had an increase in the density during cooling. It can be also seen from Figure 4.22 and Table 4.7 that SWCNTs have significantly decreased the density of the composites during sintering; however, the final (as-sintered) density was comparable for all composites.

Table 4.7: Relative density of SWCNT-YSZ composites (w.r.t. theoretical density of YSZ) during SPS cycles.

Sample	Density at the end of dwell time (%)	Final (as-sintered) density (%)	% increase in density during cooling
YSZ	84	97	13
0.2 wt% SWCNT-YSZ	78	94	16
0.5 wt% SWCNT-YSZ	77	98	21
1 wt% SWCNT-YSZ	71	95	24

Thus, the results suggest that additional densification of SWCNT-YSZ composites occurred during the cooling cycle. This densification was possibly influenced by two factors: 1) Volumetric shrinkage of the YSZ matrix due to the thermal contraction of the ceramic composite with decreasing temperature when cooling from 1300°C to the room temperature, and/or 2) Possible phase transformations in the YSZ matrix. As it was discussed in sections 4.2.1 and 4.2.2, the XRD analysis of the as-sintered YSZ samples revealed the occurrence of tetragonal to monoclinic phase transformation, which would also take place with the CNT-YSZ composites.

Once the SPS experiment was initiated ($t = 0$ sec), Figures 4.22a-c clearly illustrate that the rate of densification was significantly delayed as SWCNTs were added to YSZ. In Figure 4.22c, it was seen that the addition of SWCNTs shifted the densification rate peaks of the

SWCNT-YSZ composites to the right, indicating a delay in densification. For the 0.2 and 0.5wt% SWCNT-YSZ composites, the densification peaks appear at the same time, but the difference in the height of the peaks indicate hindrance to densification. For the 1wt% SWCNT-YSZ composite, the densification peak further shifted to the right, indicating further delay in densification.

Since all specimens were sintered under identical process parameters (i.e., the duration of the SPS experiment was constant), a delay in the densification of the SWCNT-YSZ composites likely contributed to the observed lower density of the SWCNT-YSZ composites. Although the density during the dwell period (at 1300°C) monotonically decreased with the addition of SWCNTs, the densification rate leading up to the sintering temperature varied for the different SWCNT composites. The 0.2 and 0.5wt% SWCNT-YSZ composites densified at a higher rate than the 1.0wt% SWCNT-YSZ sample, which can be seen from the height of the densification rate peaks of the composites in Figure 4.22c. It was also seen in Figure 4.22c that the plain YSZ densification rate exhibited two distinct peaks upon heating to the sintering temperature, corresponding to: 1) Powder particle rearrangement during heating, and 2) Powder densification due to particle growth. In the case of the 0.2 and 0.5wt% SWCNT-YSZ composites, the first densification step was not observed, suggesting that particle rearrangement was likely not significant. This could be the consequence of the presence of the well distributed SWCNTs along the grain boundaries, which would hinder the grain boundary movement and rearrangement. SWCNTs seen along the grain boundaries at the fracture surfaces of the as-sintered composites are shown in Figure 4.23.

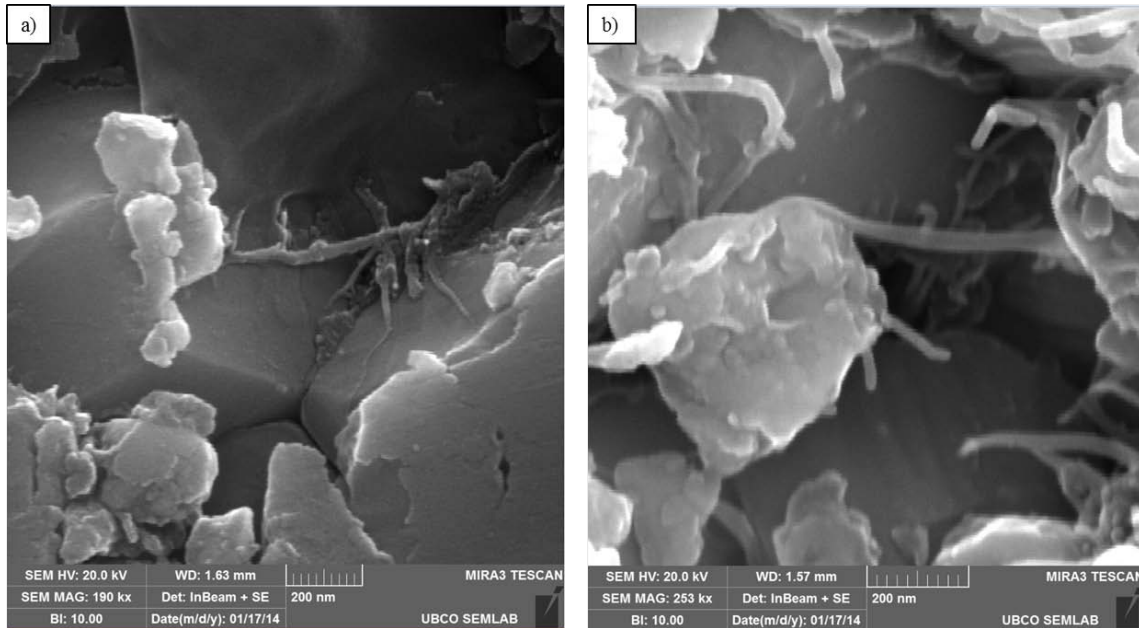


*Figure 4.23: SWCNTs as seen along the grain boundaries of the as-sintered SWCNT-YSZ composites:
a) 0.2wt% SWCNT-YSZ; b) 0.5wt% SWCNT-YSZ.*

In contrast, in case of the 1.0wt% SWCNT-YSZ composite, the first densification peak reappeared, suggesting that some powder particle rearrangement occurred. This rearrangement was correlated to the rearrangement of the matrix YSZ grains, which were free of SWCNTs because addition of 1wt% SWCNT to YSZ led to the formation of SWCNT clusters, as shown in Figure 4.24. Clustering of SWCNTs has been reported in other studies as well [49] and is believed to be related to the very high attractive Van Der Waals forces acting on the SWCNTs. Therefore, at high SWCNT doping levels, homogenous dispersion of SWCNTs was difficult, leading to non-uniform densification during SPS processing.

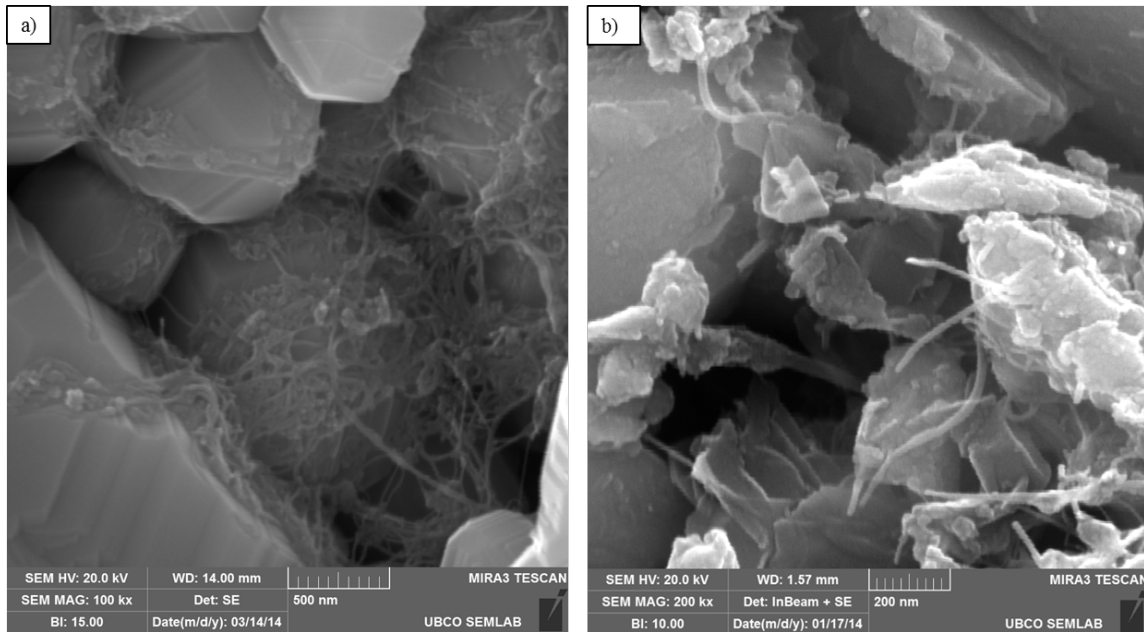


Figure 4.24: SWCNT agglomeration seen in the 1wt%SWCNT-YSZ composite:

a) Site 1 and b) Site 2.

Figure 4.25 shows the height of the as-sintered composite discs. It can be seen that the height increased with the addition of the SWCNTs. This reinforces the fact that the SWCNTs hindered grain boundary sliding, thus having a detrimental effect on the compaction of the powders.

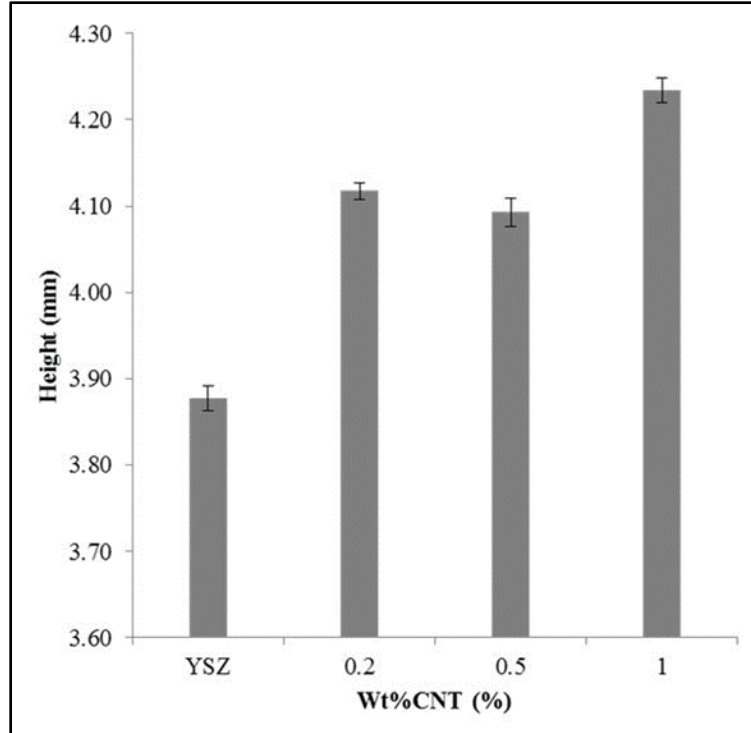


Figure 4.25: Height of the as-sintered SWCNT-YSZ composites.

Figure 4.22d shows the evolution of sintering current during the sintering experiments. During SPS, DC current is supplied until the sample temperature (measured using a pyrometer) reaches a predetermined value. As the programmed temperature profile was the same for all experiments, Figure 4.22d suggests that the addition of SWCNTs to the YSZ affected the heat input (i.e., current) to the powder samples during SPS processing. The heat required to cause the temperature to rise in the powder is given by Equation 4-1 [68]:

$$Q = m * c_p * \Delta T \quad \text{Equation 4-1}$$

where m was the mass, c_p was the specific heat and ΔT was the temperature rise. The mass of the samples was kept constant for all experiments. The thermal conductivity experiments (section 4.3.1.3; Figure 4.38) revealed that the specific heat, c_p , of the ceramic composites

did not change considerably with the addition on the SWCNTs up to an addition of 1wt% SWCNT-YSZ. The change in temperature, ΔT , was the same since the initial and the final sintering temperatures were identical for all the samples. Thus, the heat required to attain the sintering temperature for all the samples was comparable. However, in SPS an electric source is used to heat up the powders. The heat input, Q , resulting from electric current, i , is also influenced by the electrical resistance, R , of the material and is governed by Equation 4-2 [68]:

$$Q = i^2 R t \qquad \qquad \qquad \text{Equation 4-2}$$

where t was the time. From the curves in Figure 4.22d, it was observed that the current input into the samples during the SPS run decreased with the increasing concentration of SWCNTs. Therefore, it can be concluded that the addition of SWCNTs increased the electrical resistance of the composites possibly due to the presence of voids at the grain triple-points, resulting from insufficient packing, rearrangement and growth of YSZ matrix powder particles during densification, as seen in Figure 4.26.

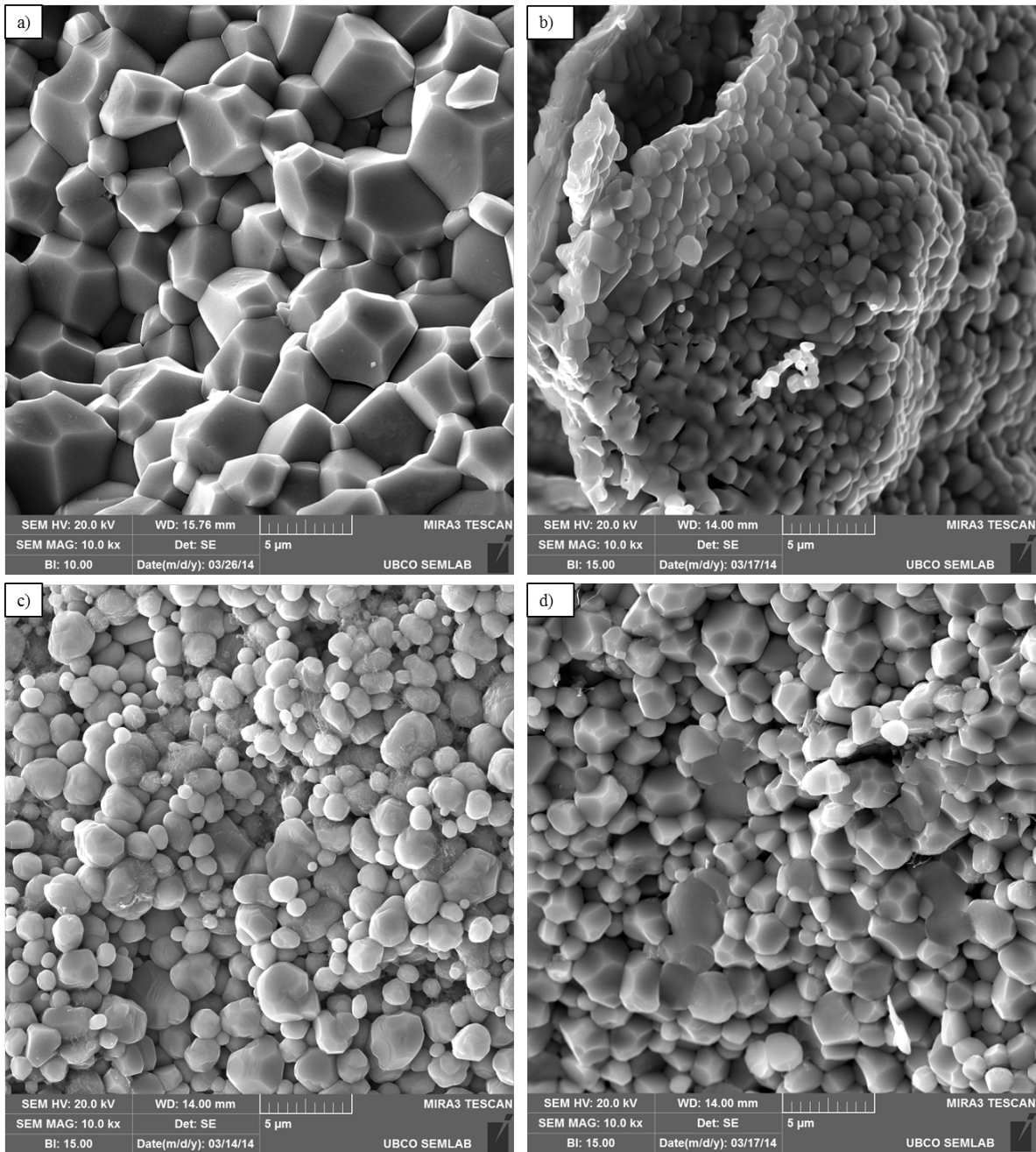


Figure 4.26: SEM images of the fracture surfaces of SWCNT-YSZ ceramic composites: a) YSZ; b) 0.2wt% SWCNT-YSZ; c) 0.5wt% SWCNT-YSZ and d) 1wt% SWCNT-YSZ.

The inhomogeneous nature of the grains was further confirmed from the deviations measured in the grain sizes of the as-sintered composites, as shown in Figure 4.27. It was seen that the

overall non-homogenous nature of the grains increased with the introduction of the SWCNTs to the YSZ matrix.

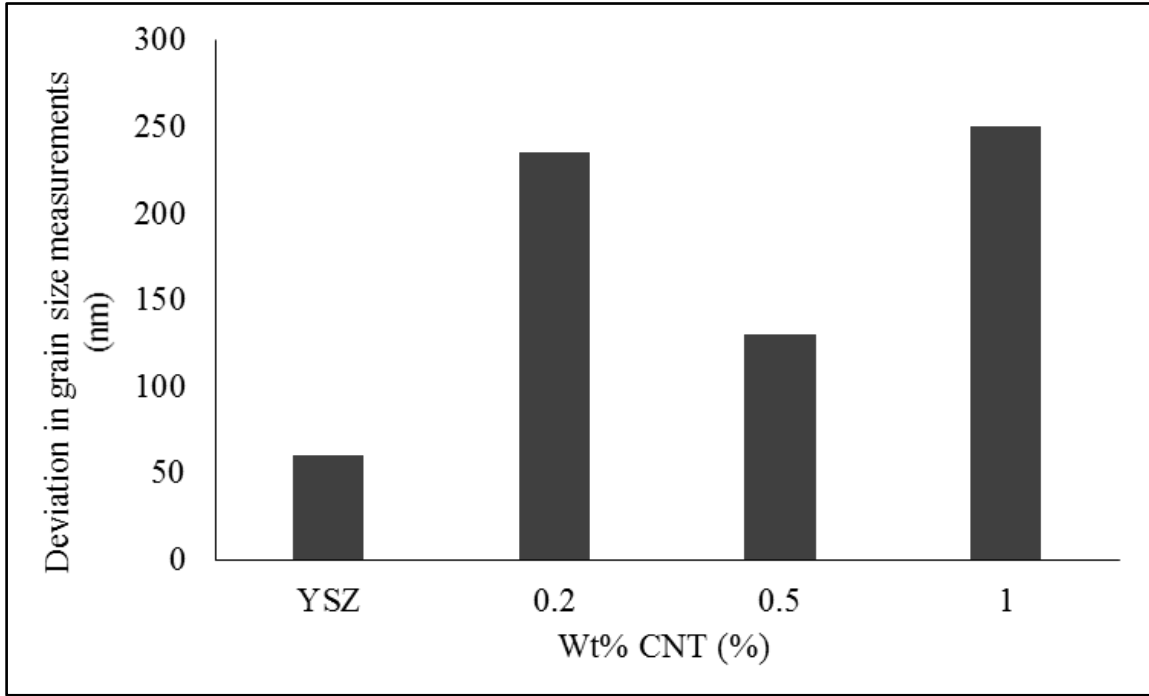


Figure 4.27: Deviations measured in the grain sizes of the as-sintered composites.

In the 1.0wt% SWCNT-YSZ sample, presence of the SWCNT agglomerations in the powder blends coincided with the regions of highly inhomogeneous YSZ matrix grains, as seen in Figure 4.28. With varying electrical resistance in the regions with SWCNT agglomerations, localized resistive heating possibly increased the temperature of the YSZ matrix grains in the immediate vicinity of the SWCNT bundles. In contrast, the SWCNT-free regions (Figure 4.28b) in the same as-sintered sample exhibited distinctly different grain growth and grain morphology. It was possible that with the localized heating, the activation energy for grain growth along new crystallographic directions was exceeded and a new grain growth mechanism was initiated. YSZ, with its cubic lattice structure, preferentially grows along the (100) plane [68]. In the case of the 1.0wt% SWCNT-YSZ composite, however, as a result of

the localized heating at the grain boundaries the activation energy to initiate growth along (100) and (111) faces was possibly achieved, resulting in the observed faceted grain growth.

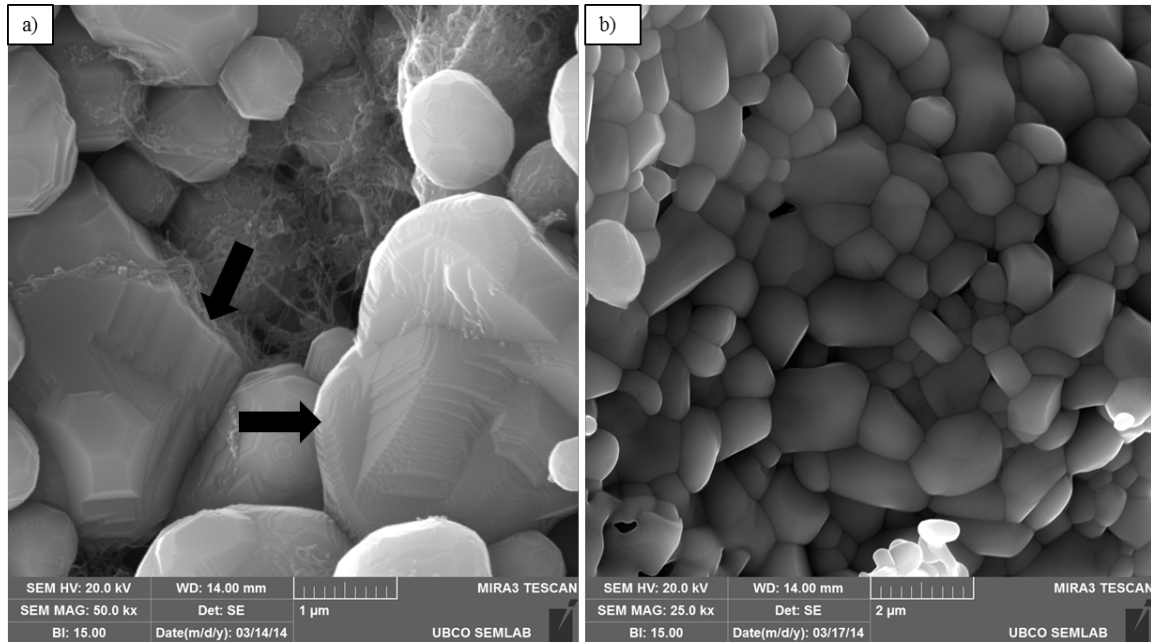


Figure 4.28: SEM images of 1.0 wt% SWCNT-YSZ composite showing: a) Faceted grains in the vicinity of the SWCNT bundles and b) Grains in regions free of SWCNTs.

Performing microstructure analysis and grain size measurement, it was seen that the grains of the SWCNT-YSZ ceramic composites were significantly smaller than those of the pure YSZ ceramic. The final density measurements reveal that the final density of the composites did not vary significantly despite the significant difference in the grain sizes, as can be seen in Figure 4.29a and b. This suggests that the grain growth did not have a considerable influence on the density of the samples.

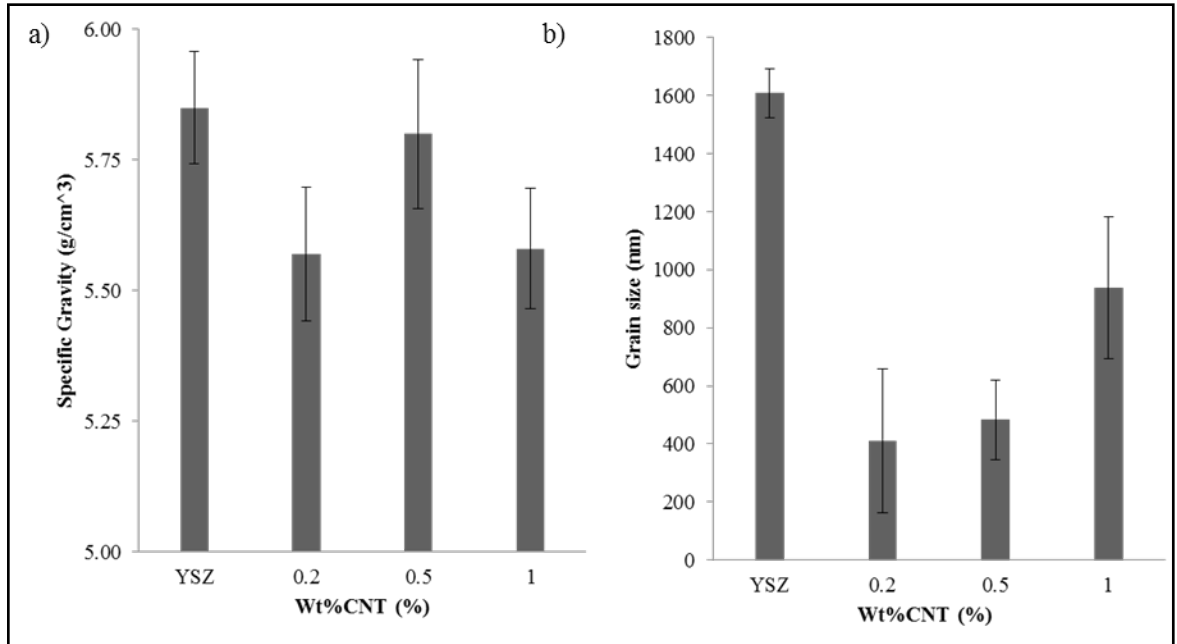


Figure 4.29: a) Specific gravity and b) Grain size measurements of the as-sintered SWCNT-YSZ ceramic composites.

Granger *et al.* [65] suggested that the densification of YSZ occurs by grain particle rearrangement due to grain boundary sliding and grain growth by diffusion [65]. However, it was seen previously from the sample height measurements that the SWCNTs in the YSZ matrix hinder grain boundary sliding. As the SWCNTs resisted the consolidation of the powders by mechanically opposing sliding and particle rearrangement, the overall pressure in the powder blends decreased, which resulted in thicker discs (seen in Figure 4.25). Since the total applied pressure during all the sintering runs was maintained constant (30MPa), the load transfer by the SWCNTs between the adjacent grains of the YSZ matrix possibly resulted in localized stress induced recrystallization, which was seen in the form of internal grain structures (observed on the polished surfaces) in the SWCNT-YSZ ceramic composites, as shown in Figure 4.30.

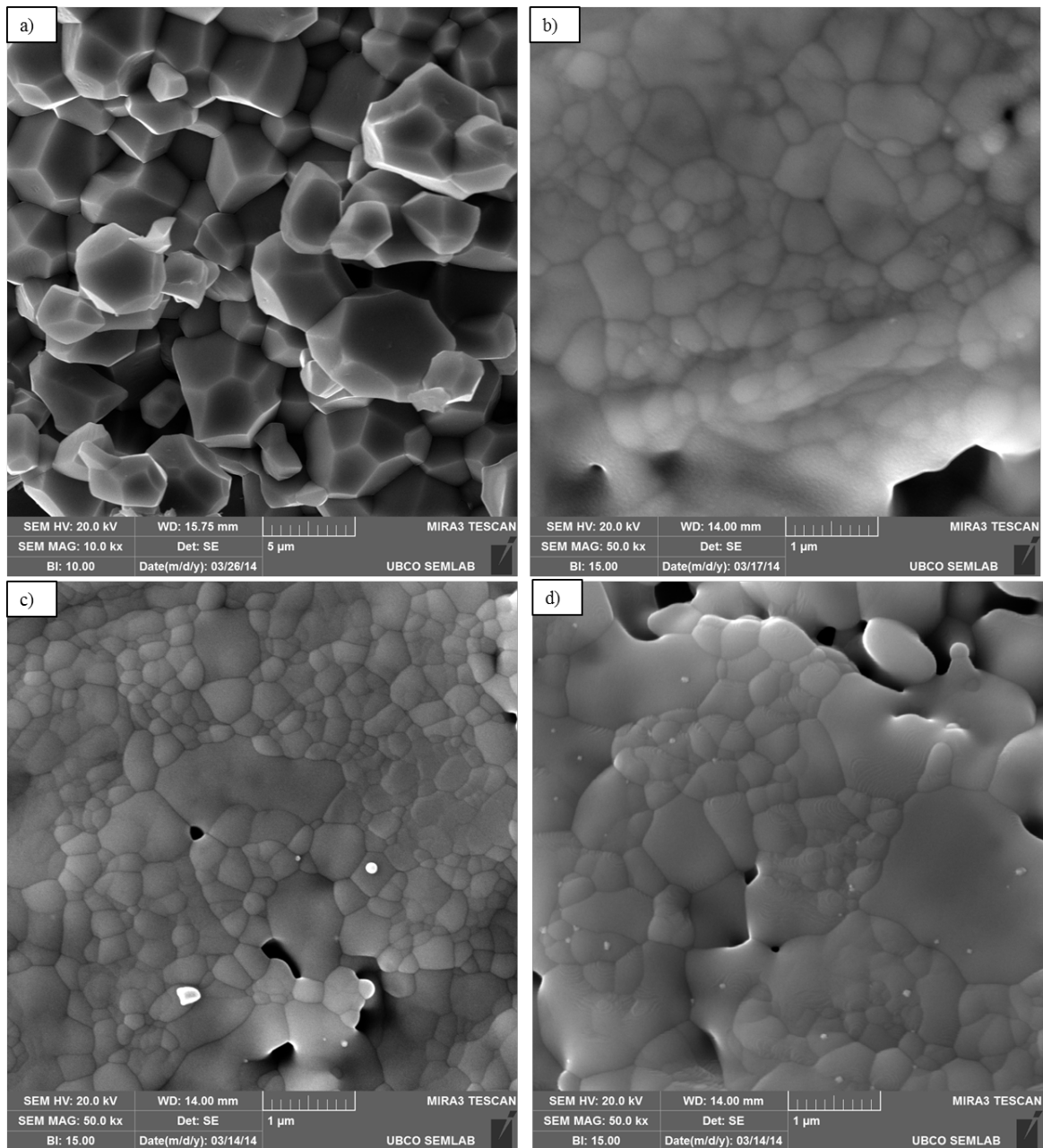


Figure 4.30: Internal structures in SWCNT-YSZ ceramic composites: a) YSZ; b) 0.2wt% SWCNT-YSZ; c) 0.5wt% SWCNT-YSZ and d) 1wt% SWCNT-YSZ.

4.3.1.2 Microhardness of the SWCNT-YSZ Ceramic Composites

The results of the microhardness testing are provided in Figure 4.31. From the results, it was seen that the hardness of the samples increased with the increase in the SWCNT content. Interestingly, comparing the hardness and the grain size measurements of the samples, it was observed that for the pure YSZ and the 0.2wt% SWCNT-YSZ composite, the hardness increased with a decrease in the grain size. This is according to the classical Hall-Petch effect [69, 70], where the hardness of the sample increases with the decrease in the grain size. On the contrary, for the SWCNT-YSZ composites, it can be seen that the hardness of the samples increased with an increase in the grain size. Similar results were reported by Carlton *et al.* [71], who studied the inverse Hall-Petch relationship in nanocrystalline materials. They stated that the inverse Hall-Petch effect means that nanocrystalline materials tend to soften as their grain size reduces below a certain limiting value. Choksi *et al.* [72] reported that the Hall-Petch relation could not yield expected values for materials with grain sizes less than 1 μ m. In this work, it can be seen that the inverse Hall-Petch effect was followed for the SWCNT-YSZ composites, with their average grain sizes less than 1 μ m.

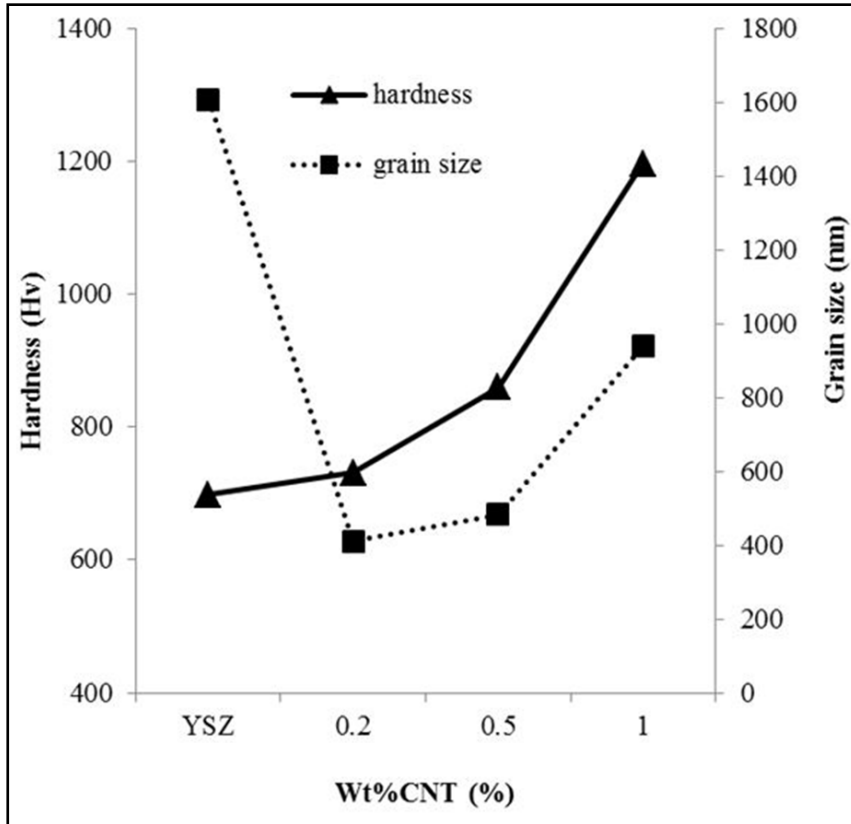


Figure 4.31: Hardness and grain size of the SWCNT-YSZ ceramic composites.

Zhou *et al.* [73] suggested that SWCNTs may enhance the hardness of composite materials by bridging adjacent grains and lowering the tensile stress around any nucleating cracks, thereby strengthening and toughening the composite ceramic material. In this work, SWCNTs were seen to bridge adjacent grains, thereby likely resisting grain boundary sliding and ensuing plastic deformation, as seen in Figure 4.32.

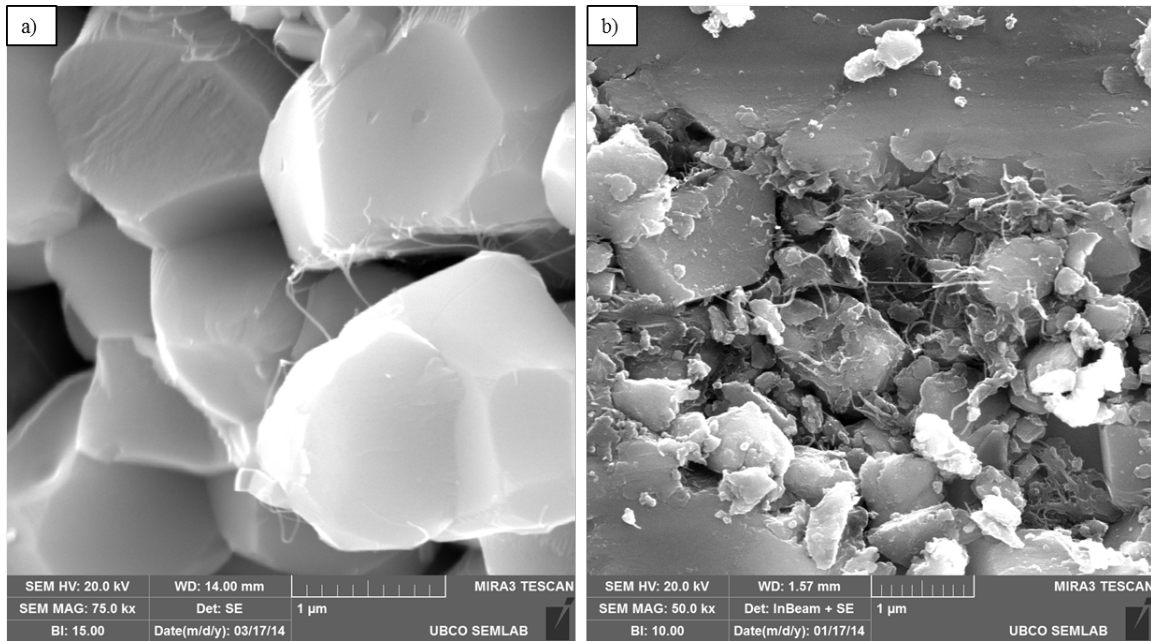


Figure 4.32: SWCNTs seen bridging grains in: a) 0.5wt%SWCNT-YSZ and b) 1wt% SWCNT-YSZ composites.

4.3.1.3 Nano Indentation of the SWCNT-YSZ Ceramic Composites

The nano indentation hardness results, shown in Figure 4.33, suggest that the nano-hardness of the composites decreased with increase in the SWCNT concentration. In case of the nano indentation experiments, the indentations were made in the interior of the grains. This observation suggests that the SWCNTs caused softening of the grains of the YSZ matrix.

As indicated in Figure 4.22d of section 4.3.1.1, the current passing through the SWCNT-YSZ ceramic compacts during sintering was less than that for pure YSZ, indicating higher electrical resistance of the SWCNT-YSZ ceramic composites. With the increased electrical resistance, localized heating possibly caused localized temperatures in the YSZ matrix grains in the vicinity of the SWCNTs, such that the localized temperatures possibly annealed the YSZ matrix grains leading to their softening.

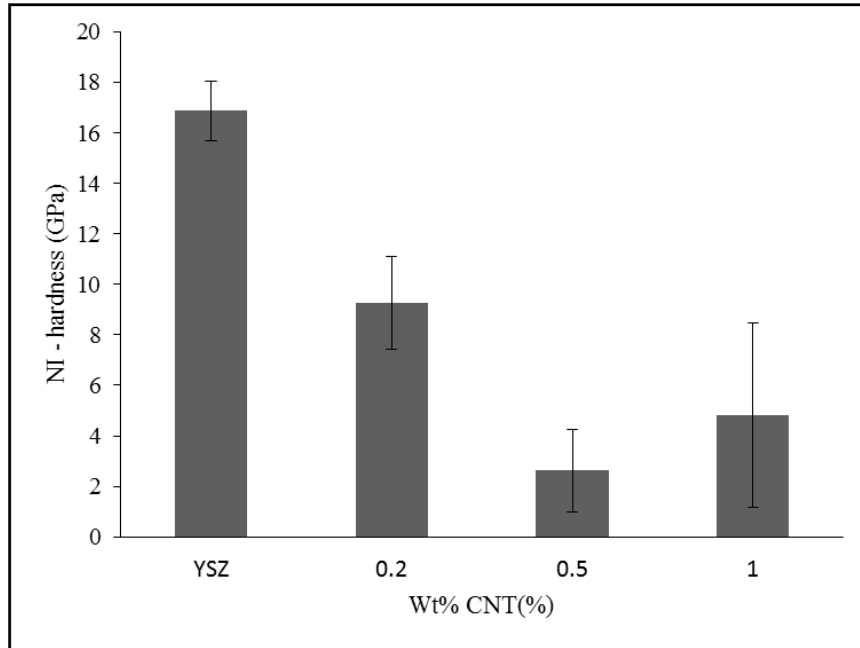


Figure 4.33: Nano Indentation hardness of the SWCNT-YSZ composites.

From Figure 4.33, it was seen that between the 0.2 and 0.5wt% SWCNT-YSZ composites, the hardness decreased with the increase in the SWCNT content; whereas, between the 0.5wt% and 1wt% SWCNT-YSZ composites, the hardness increased from 2.62GPa for 0.5wt% SWCNT-YSZ to 4.82GPa for 1wt% SWCNT-YSZ composites. Interestingly, the standard deviation for the NI-hardness also increased for the SWCNT-YSZ composites, with 1wt% SWCNT-YSZ composite having the highest standard deviation. The softening of the YSZ matrix grains in the 1wt% SWCNT-YSZ composites, was a localized phenomenon, due to the localized elevated temperatures in the vicinity of the SWCNTs. Since there were regions in the 1wt% SWCNT-YSZ ceramic composites free of SWCNTs, the NI-hardness had higher standard deviation with increasing SWCNT concentration.

Comparing the microhardness and the NI hardness values, as shown in Figure 4.34, it is evident that the microhardness increased with the SWCNT addition, while the NI hardness

decreased. These results confirm that the SWCNTs achieved grain pinning and resisted grain boundary sliding, thus successfully improving the resistance to plastic deformation.

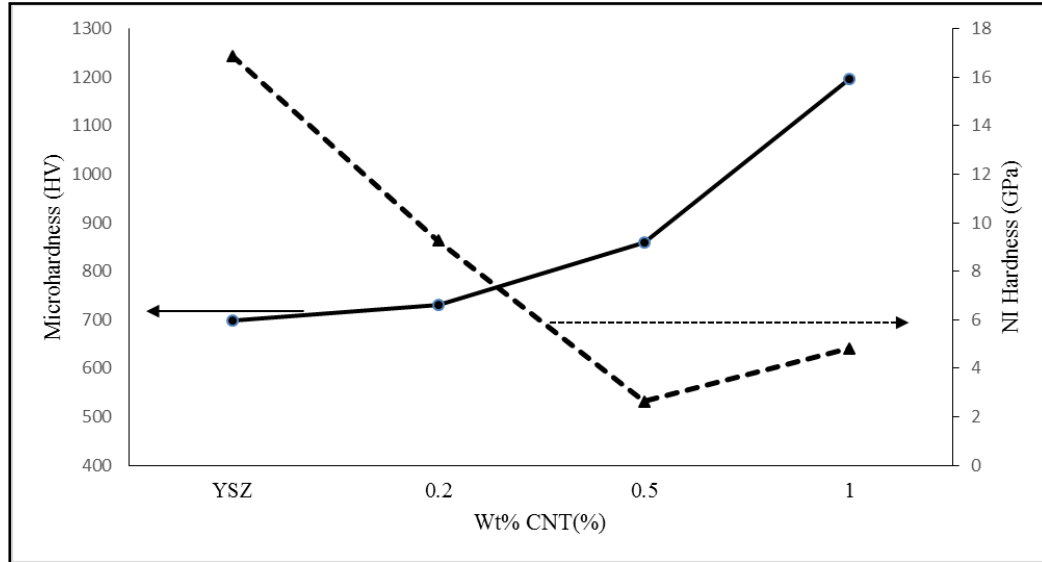


Figure 4.34: Comparison of the microhardness and the NI hardness of the SWCNT-YSZ ceramic composites

Load – Displacement curves obtained from the NI experiments are provided in Figure 4.35. It was observed that for the same load of $5000\mu\text{N}$, the depth of the indentation for the composites varied with the varying SWCNT concentration. The load – displacement peak shift with the addition of SWCNTs suggested that the matrix grains of the SWCNT-YSZ composites were softer than in the case of the monolithic YSZ grains. The 0.5wt% SWCNT-YSZ composite had softer grains than the 0.2wt% SWCNT-YSZ composite, but for the 1wt% SWCNT-YSZ composite, the hardness increased. This trend is currently not fully understood.

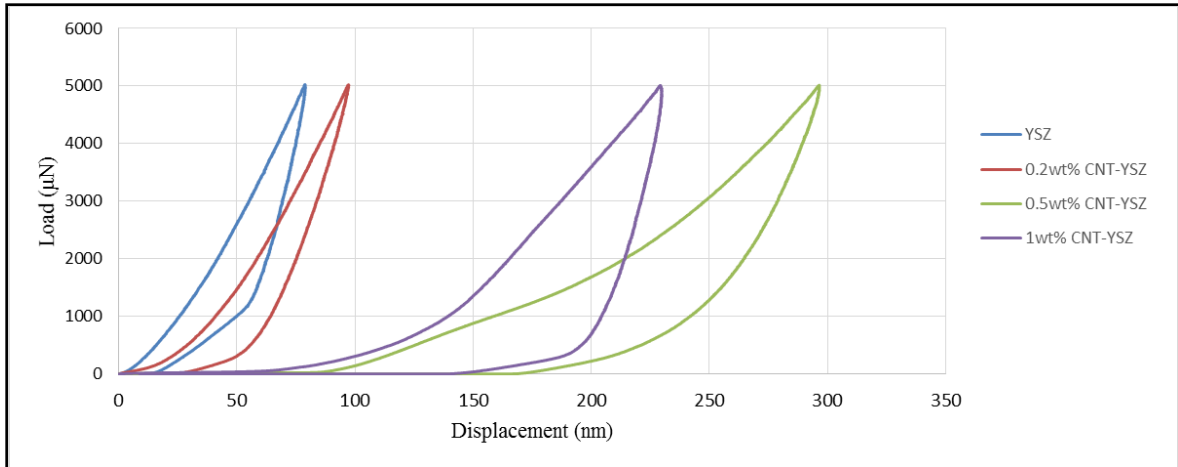


Figure 4.35: Load-Displacement curve for the SWCNT-YSZ ceramic composites.

YSZ ceramics are known to be very brittle in nature with minimal plastic deformation [7], but the grains of the ceramic composites in this study showed an elasto-plastic nature, as seen in Figure 4.35 (horizontal portion of the load curve). This depicts the plastic deformation undergone by the grains during the indentation process. The total plastic deformation in the composites increased with the addition of the SWCNTs, as seen in Figure 4.36. This result is in agreement with the NI hardness measurements which revealed that the matrix grains became softer as SWCNTs were added to YSZ.

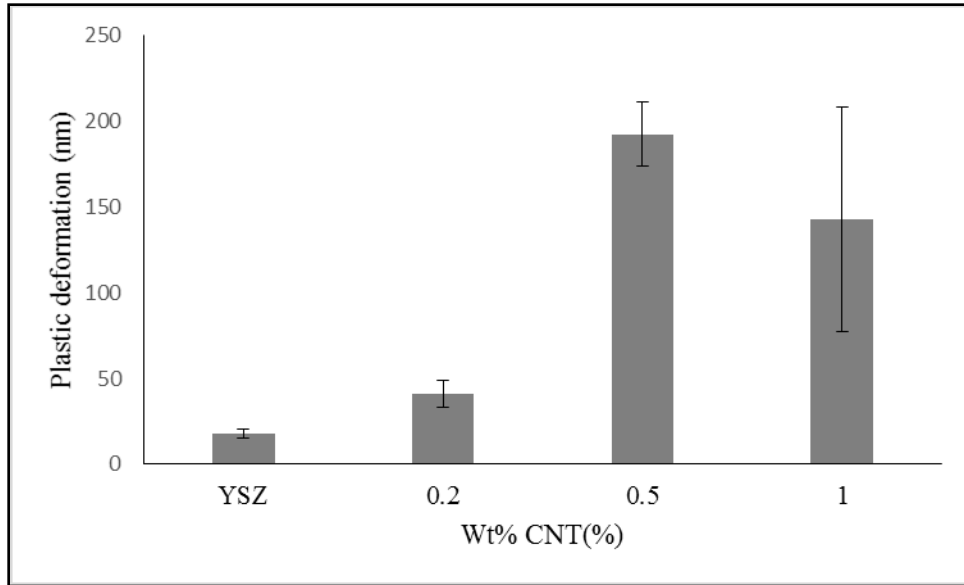


Figure 4.36: Plastic deformation measured in the composites after the indentation.

Results of Young's modulus measurement during the NI experiments are provided in Figure 4.37. It was seen that the Young's modulus decreased with the addition of the SWCNTs upto 0.5wt% SWCNTs and thereafter increased for 1wt% SWCNT content. This result also follows the similar trend as the NI hardness trend of the ceramic composites. This could possibly be due to the softening of the grains during the annealing of the grains in the vicinity of the SWCNTs.

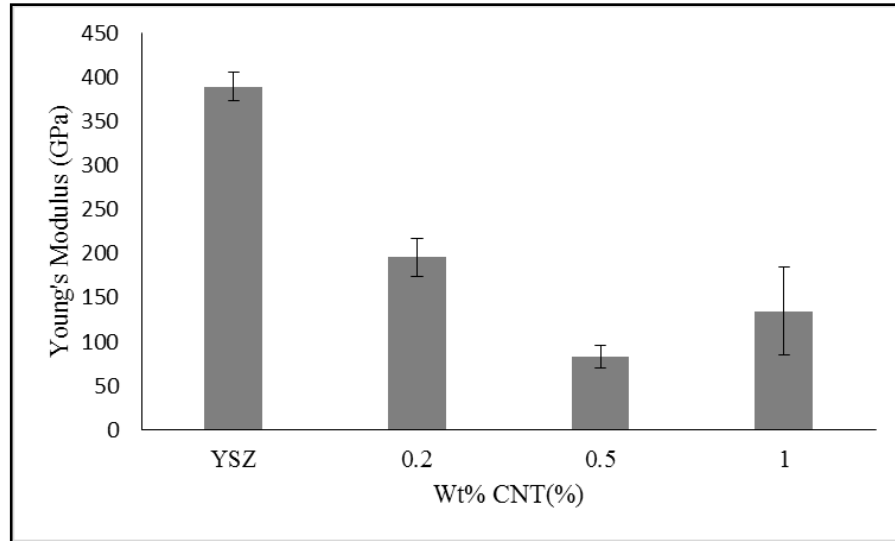


Figure 4.37: Young's modulus of the SWCNT-YSZ ceramic composites.

Mehdi *et al.* [56] conducted mechanical property experiments using Vickers diamond indenter, from which they calculated the Young's modulus of the MWCNT-YSZ ceramic composites based on the crack length originating from the indentation center. They reported that the Young's modulus of the ceramic (at a bulk scale) increased with the increase in the SWCNT content, as seen in Table 4.8 [56]. Their results contradicted the NI-Young's modulus results obtained in this work. The discrepancy in the results could be possibly contributed to the different instrumentation used, as well as different dispersion of the SWCNTs on the grain boundaries. Further, Mehdi *et al.* [56] deformed their material up to the point when cracks formed in the grains. Thus, some of the energy measured by Mehdi *et al.* [56] had gone into the nucleation and propagation of cracks.

Table 4.8: Comparison of the observed Young's modulus results with literature.

Sample	Young's modulus (GPa) as per Mehdi <i>et al.</i> [56]	Young's modulus (GPa) obtained in this work
YSZ	198 ± 15	389.3 ± 18
0.2wt% SWCNT-YSZ	_____	195.6 ± 21
0.5wt% SWCNT-YSZ	206 ± 21	82.8 ± 13
1wt% SWCNT-YSZ	_____	134.7 ± 36.2
1.5wt% SWCNT-YSZ	225 ± 18	_____
3wt% SWCNT-YSZ	241 ± 9	_____
5wt% SWCNT-YSZ	258 ± 22	_____

Similar to what was seen previously in the hardness of the SWCNT-YSZ ceramic composites, the bulk Young's modulus of the SWCNT-YSZ ceramic composites increased with the addition of SWCNTs [56], while the NI Young's modulus decreased with the addition of the SWCNTs. This phenomenon can be attributed to the softening of the YSZ matrix grains due to the localized annealing, as discussed previously.

4.3.1.4 Thermal Properties of the SWCNT-YSZ Ceramic Composites

The influence of the SWCNTs on the thermal properties of the ceramic composites was investigated in terms of the specific heat, thermal diffusivity and thermal conductivity. The effect of SWCNTs on the specific heat of the SWCNT-YSZ ceramic composites is shown in Figure 4.38.

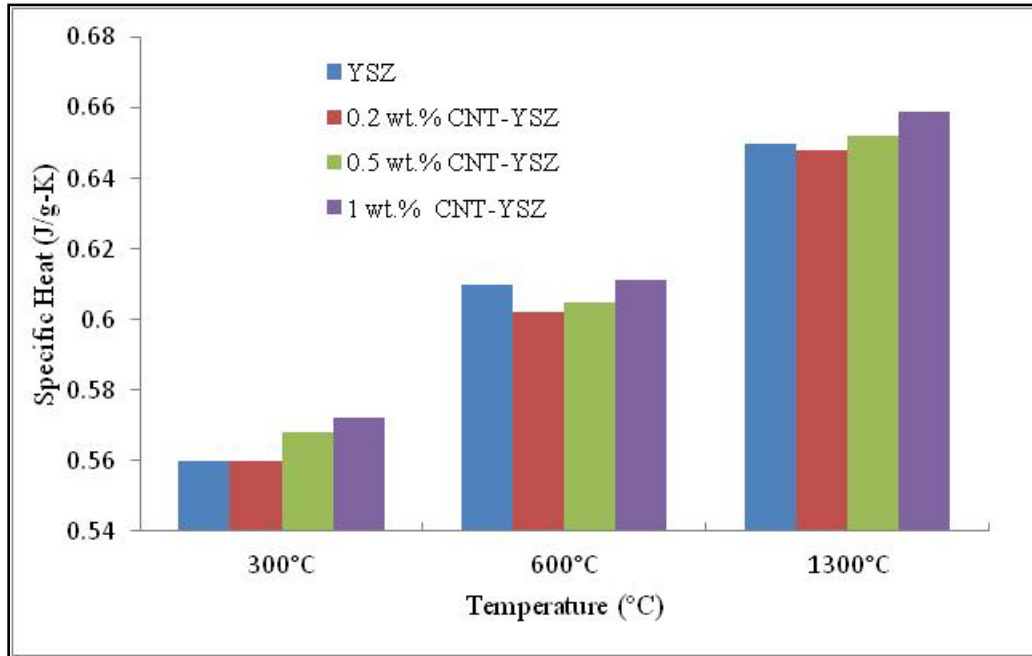


Figure 4.38: Specific heat of the SWCNT-YSZ ceramic composites measured at three different temperatures.

From Figure 4.38 it can be seen that for a given temperature, the specific heat of the ceramics increased with the increase in the SWCNT content, which implied that the internal energy of the ceramic composite grains was increasing with the addition of the SWCNTs.

The amount of heat supplied to a solid material translates into either vibrational energy of the atoms, increase in the energy level of electrons in the atomic structure or change in the atomic positions arising from defects. These changes in the material lead to an increase in the internal energy and the configurational entropy of the material [7]. This increase in the internal energy and the configurational entropy corresponds to an increase in the specific heat of the material [7, 74]. Determination of the exact factors responsible for the increase in specific heat in this research is beyond the scope of this thesis.

Debye [75] and Compton [76] postulated a simple theory of specific heat of solids, which stated that the specific heat of a solid is a consequence of the vibration of atoms in the solid lattice structure. The theory suggested that the specific heat is proportional to T^3 (where T was the temperature) [75]. Therefore, the results are in agreement with Debye's theory, since the specific heat of the ceramic composites increased with an increase in the temperature, as seen in Figure 4.38.

The thermal conductivity of the SWCNT-YSZ ceramic composites is shown in Figure 4.39. It was expected that the thermal conductivity of the SWCNT-YSZ composites would monotonically increase due to the relatively high thermal conductivity of the carbon nanotubes [77].

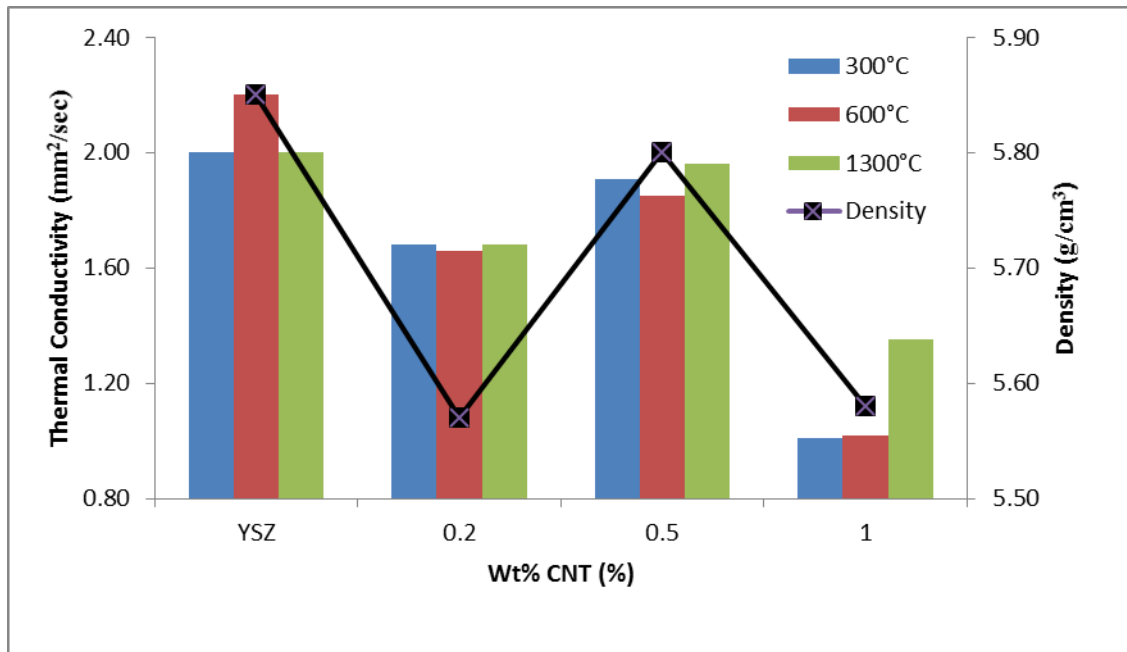


Figure 4.39: Thermal conductivity of the SWCNT-YSZ ceramic composites.

However, thermal conductivity of the composites decreased with the addition of the SWCNTs. The steady state thermal conductivity equation is given by [78]:

$$D = \frac{\lambda}{c_p \rho} \quad \text{Equation 4-3}$$

Where D was the thermal diffusivity, λ was the thermal conductivity, c_p was the specific heat and ρ was the density of the material. From Equation 4-3, it can be derived that for a given material, the thermal conductivity is directly proportional to the density of the material, provided that the thermal diffusivity and the specific heat are constant. Therefore, relating the density of the ceramic composites to their thermal conductivity, a direct relationship was observed, as seen in Figure 4.39. The density of the sintered materials was inversely related to the porosity in the ceramics, which has a major influence on the thermal conductivity of the ceramic. The heat transfer across pores is usually inefficient because of the low thermal conductivity of air [74].

From Equation 4-3, it can be stated that the thermal diffusivity is directly proportional to the thermal conductivity. The thermal diffusivity of the samples followed the same trend as the thermal conductivity of the samples for a given temperature. The thermal diffusivities of the samples is plotted in Figure 4.40.

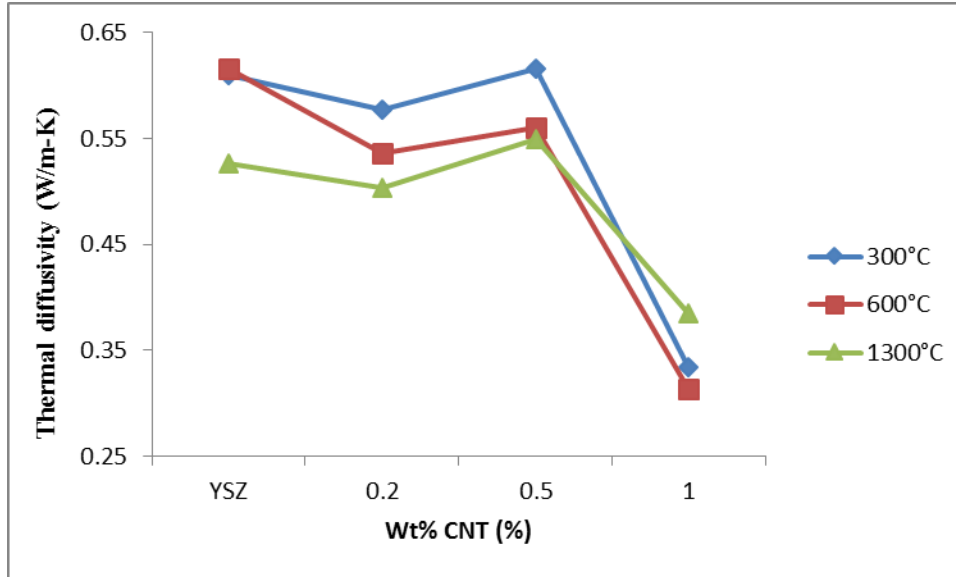


Figure 4.40: Thermal diffusivity of the SWCNT-YSZ ceramic composites.

It can be seen that as previously mentioned in the literature, the thermal diffusivity tends to decrease with the increase in the temperature [79, 80]. For the thermal diffusivity measured at 300°C, it reduced by 5.48% from pure YSZ to 0.2wt% SWCNT-YSZ. Further with the 0.5wt% SWCNT addition, the thermal diffusivity increased by 6.75% with respect to the 0.2wt% SWCNT-YSZ composite, higher than that of pure YSZ composite (both measured at 300°C). On adding 1wt% SWCNT, the thermal diffusivity of the composites reduced from 0.61mm²/sec for pure YSZ to 0.33mm²/sec for 1wt% SWCNT-YSZ.

Similar trends were seen for the thermal diffusivities measured at 600°C and 1300°C, with the exception of thermal diffusivity of pure YSZ at 600°C, which was the highest amongst all four composites.

4.3.2 Processing and Preliminary Characterization of MWCNT-YSZ Ceramic Composites

The MWCNT-YSZ powders were blended following the procedure outlined in Section 3.2. SEM analysis was performed to examine the homogeneity of the MWCNTs in the YSZ matrix. As seen in Figure 4.41, the MWCNTs did not form significant agglomerates in the mixed powders (arrows point towards the MWCNTs as seen in the powder blends).

All the sintering of the MWCNT-YSZ ceramic composites were carried out at similar conditions as the SWCNT-YSZ ceramic composites. The only difference with the MWCNT-YSZ ceramics was the sintering dwell time at 1300°C which was reduced to 3 minutes from 5 minutes. This was justified based on observations that the sintering dwell time did not have a statistically significant influence on the densification of the ceramic composites.

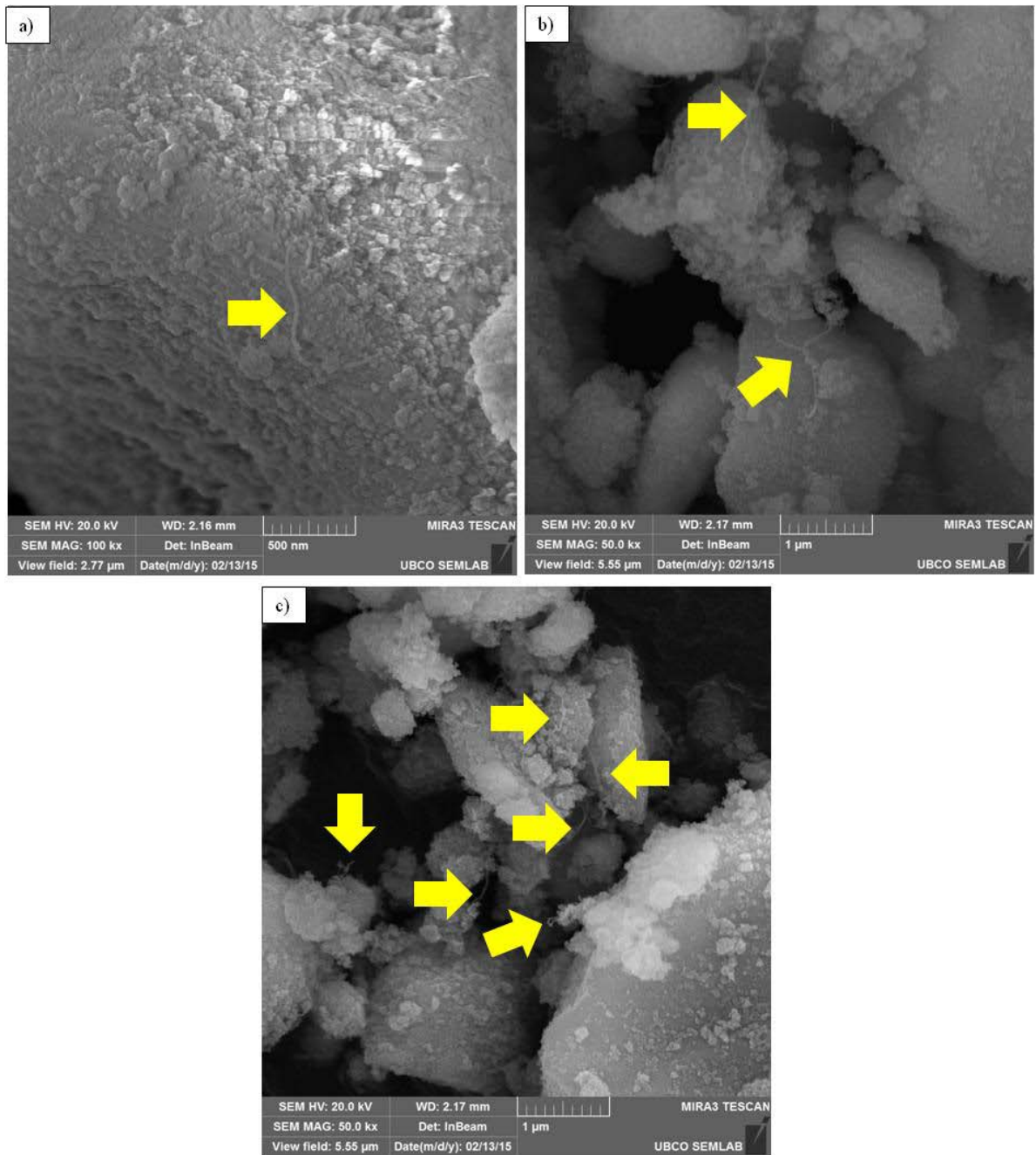


Figure 4.41: SEM images of MWCNT-YSZ powder blends: a) 0.2wt% MWCNT-YSZ; b) 0.5wt% MWCNT-YSZ and c) 1wt% MWCNT-YSZ.

4.3.2.1 Effect of MWCNTs on the Densification Behavior of the Ceramic Composites

The MWCNTs had a lesser impact on the densification behavior of the ceramic composites than in the case of SWCNT composites. Figure 4.42 shows the densification rate plots of the MWCNT-YSZ ceramic composites.

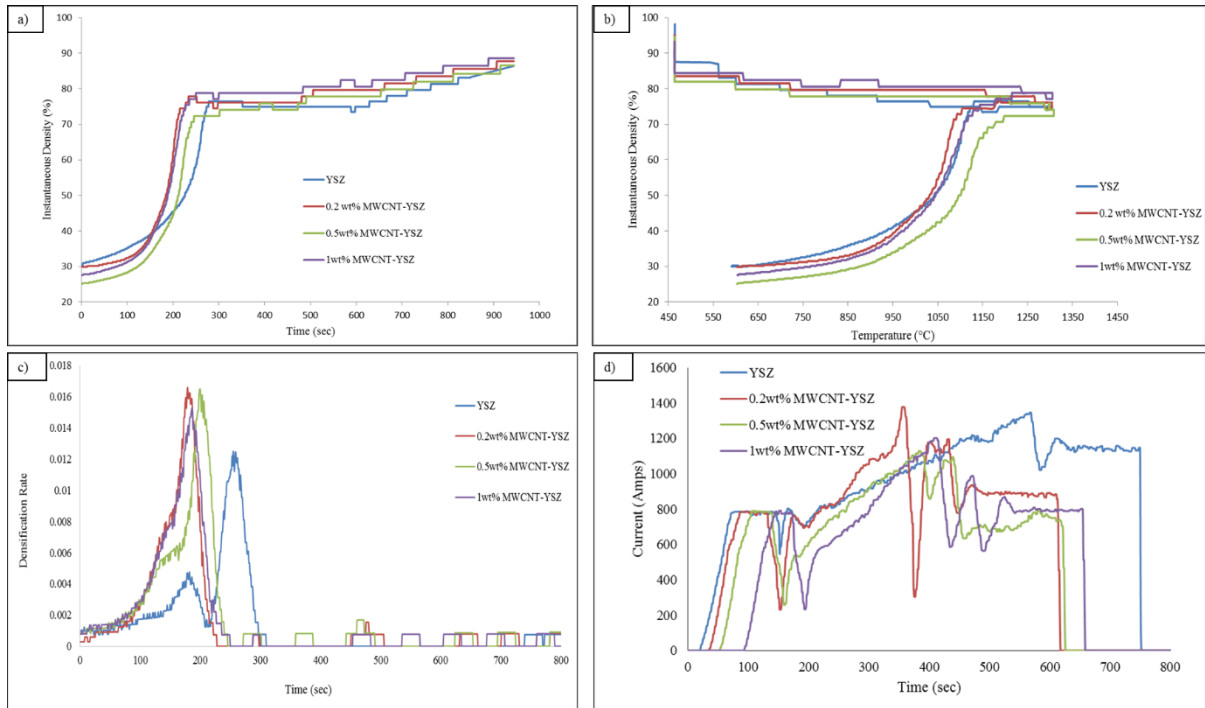


Figure 4.42: Densification behavior of the MWCNT-YSZ ceramic composites: a) Instantaneous density vs Time; b) Instantaneous density vs Temperature; c) Densification rate vs Time and d) Current vs Time plots.

From Figure 4.42a. and b it was seen that the green density of the precompacts (at time $t = 0$ and temperature $T = 600^{\circ}\text{C}$), decreased with the addition of the MWCNTs. This could be due to the MWCNTs hindering particle rearrangement. During the sintering cycle, the MWCNTs did not show much effect, as there was no considerable difference in the instantaneous density curves.

From the densification rate curves, shown in Figure 4.42c, it was seen that the MWCNTs did not delay the overall densification process. But, the dual peak nature of the densification rate curves of YSZ, representing particle rearrangement and grain growth was not prominent in the MWCNT-YSZ ceramic composites.

The densities of the as-sintered MWCNT-YSZ ceramic composites are shown in Figure 4.43. It was seen that the final densities of the composites decreased with the addition of the MWCNTs, as was also observed for SWCNTs.

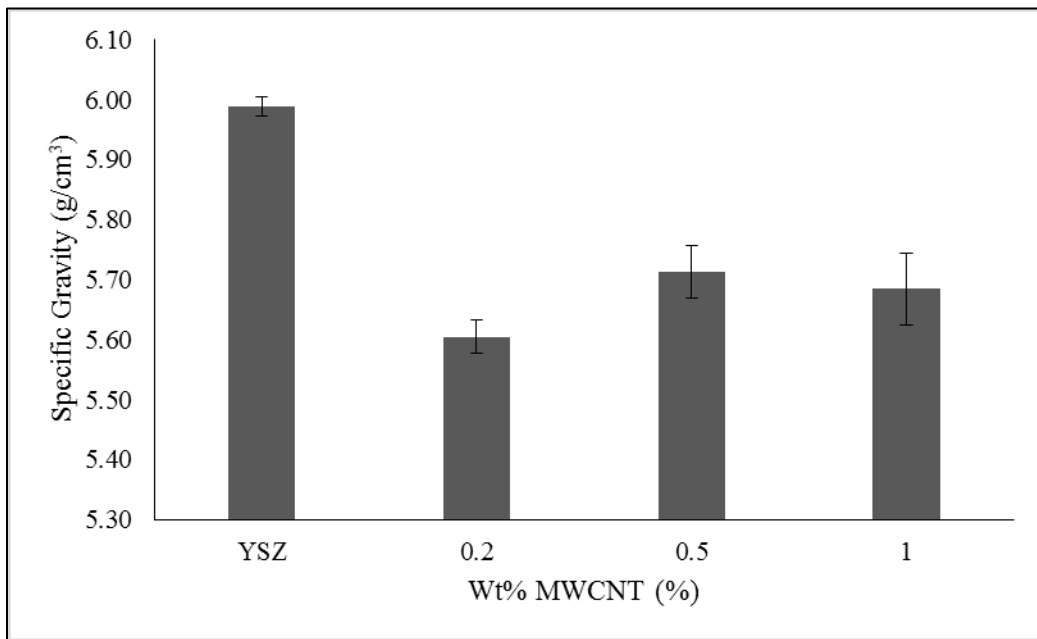


Figure 4.43: Specific gravity measurements of the MWCNT-YSZ ceramic composites.

SEM analysis was performed on the MWCNT-YSZ ceramic composites to examine the grain structure. Figure 4.44 shows that the grains in the YSZ composite were more closely packed in comparison to the grains in the MWCNT-YSZ ceramic composites, thus confirming that the lower specific gravity of the MWCNT composites (Figure 4.43) was likely related to interparticle porosity.

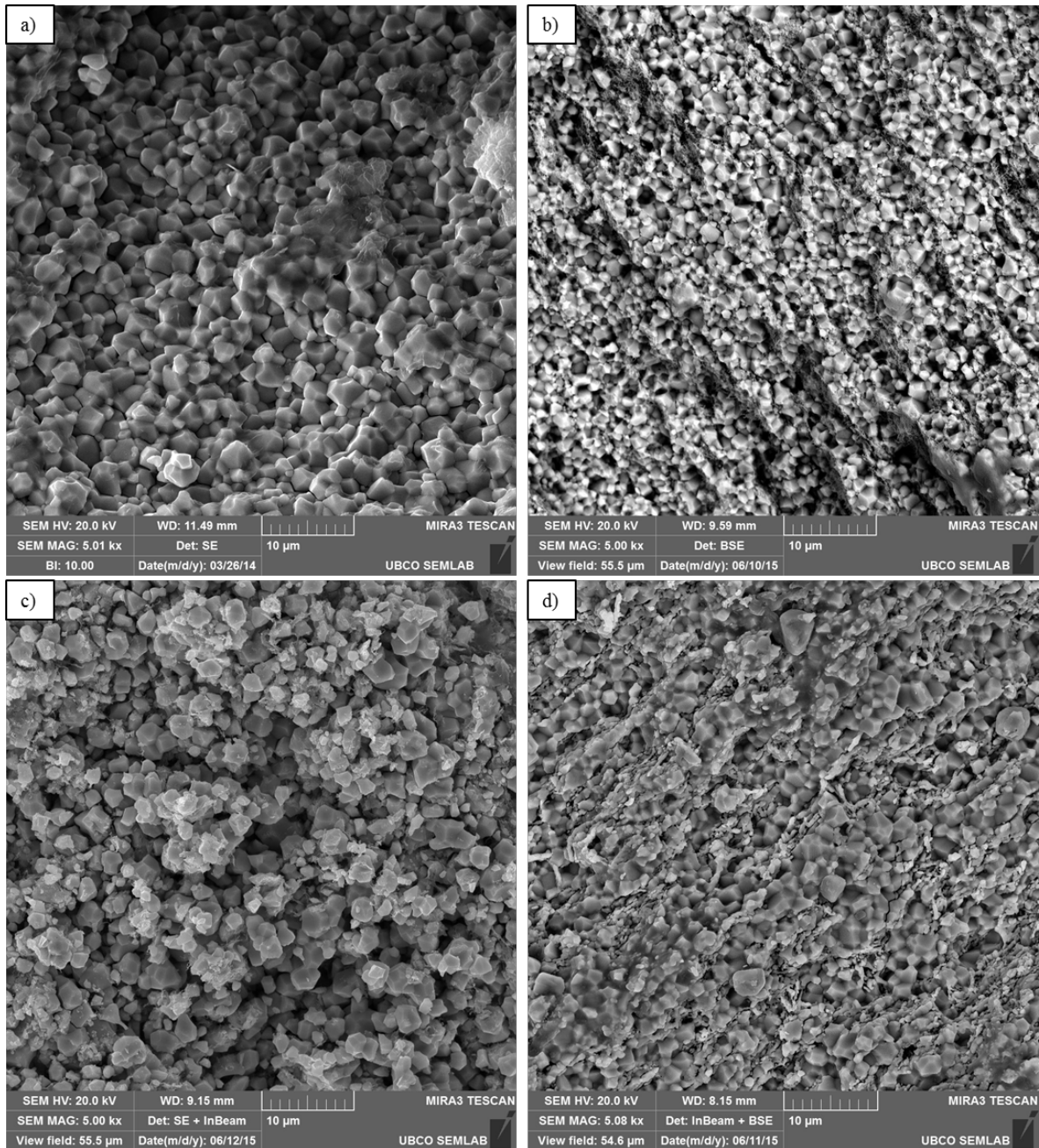


Figure 4.44: SEM images on the fracture surfaces of: a) YSZ; b) 0.2wt% MWCNT-YSZ; c) 0.5wt% MWCNT-YSZ and d) 1wt% MWCNT-YSZ ceramic composites sintered at 1300°C for 3min.

Performing grain size measurements on the MWCNT-YSZ ceramic composites (Figure 4.45) revealed no statistically significant change in the grain sizes as MWCNTs were added.

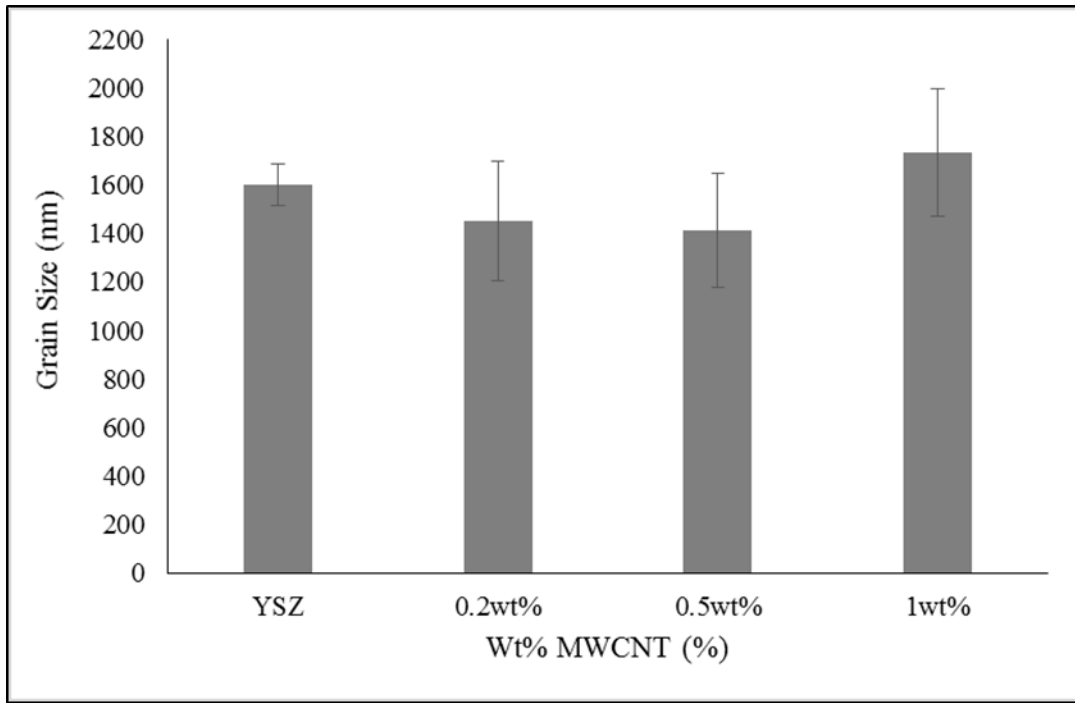
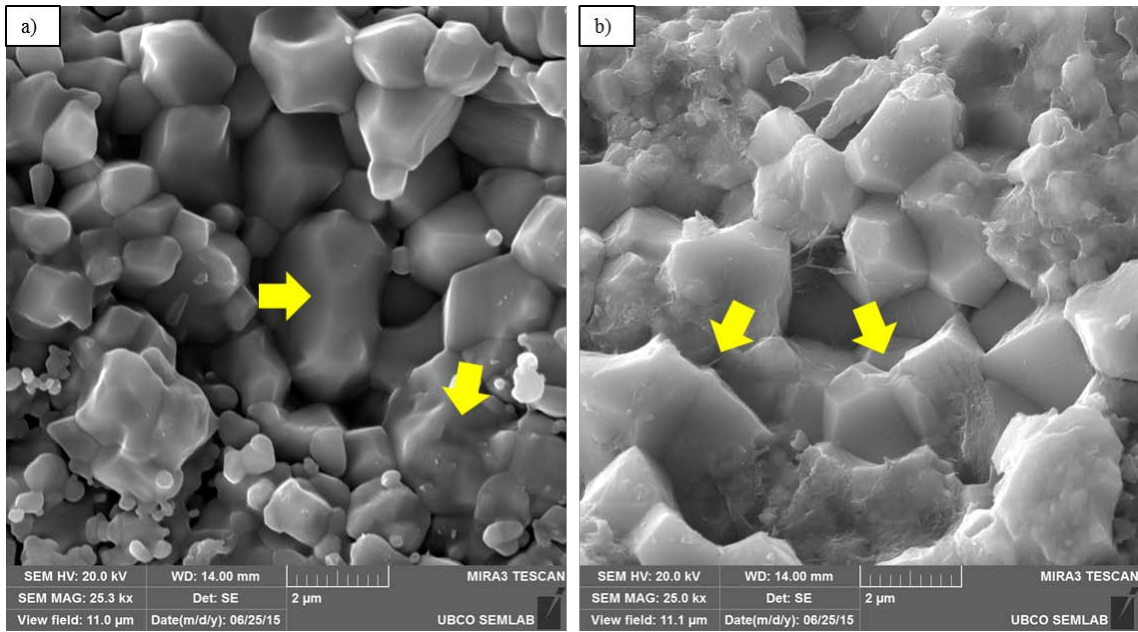


Figure 4.45: Grain size of the as-sintered MWCNT-YSZ ceramic composites.

From the grain size measurements, shown in Figure 4.45, it can be seen that the standard deviation in the measurements increased with the addition of the MWCNTs. This was similar to the trend seen in the case of SWCNT-YSZ ceramic composites (Figure 4.27). In case of the MWCNTs, it was seen that the total electrical resistance of the ceramic composites did not considerably increase with the addition of the MWCNTs (as shown in Figure 4.42d.). The high deviation in the grain size measurements could be due to the MWCNTs hindering the particle rearrangement, causing localized porosity. High levels of porosity would hinder transfer to the grains during sintering, thereby leading to non-uniform heating and grain growth.



*Figure 4.46: Fusion of grains as seen in: a) 0.2wt% MWCNT-YSZ and
b) 1wt% MWCNT-YSZ ceramic composites.*

From the SEM analysis, it was found that the MWCNTs formed agglomerates in the ceramic composites during the sintering. The agglomeration of the MWCNTs were seen distinctly in the 0.2 and 0.5wt% MWCNT-YSZ ceramic composites, as shown in Figure 4.47.

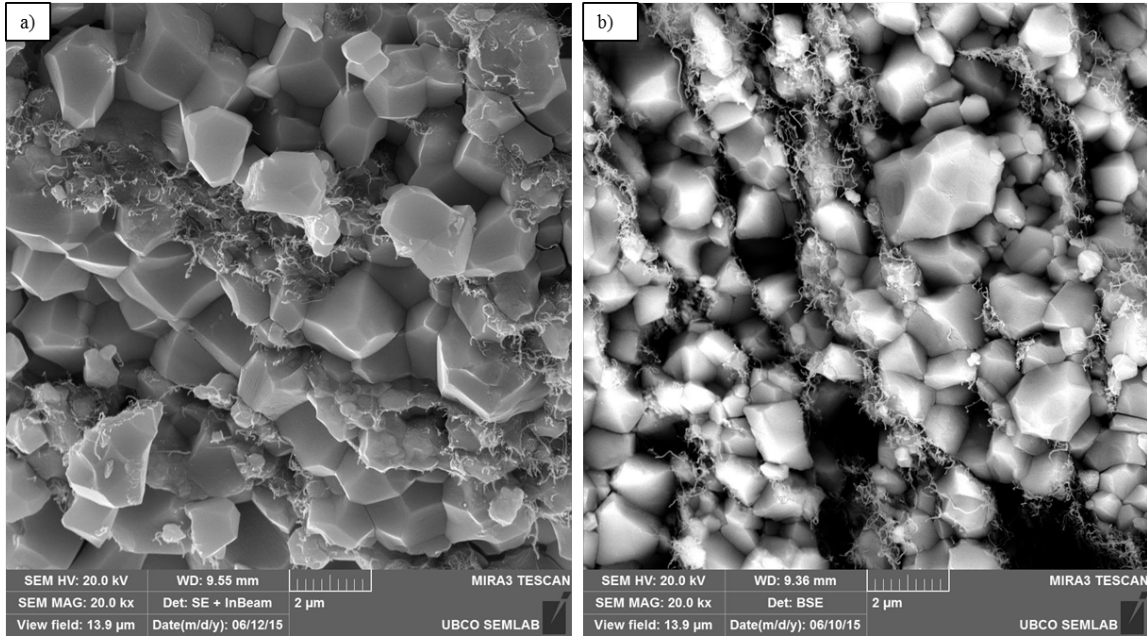


Figure 4.47: Agglomeration of the MWCNTs in: a) 0.2wt% MWCNT-YSZ and b) 0.5wt% MWCNT-YSZ ceramic composites.

In the 1wt% MWCNT-YSZ ceramic composite, regions with a second phase were seen along the grain boundaries, as shown in Figure 4.48. X-EDS analysis on one such network-like phase (shown in Figure 4.49), revealed a high amount of carbon (Table 4.9). In this composite, MWCNTs were not spotted. Thus, the secondary phases could be representative of disintegrated MWCNTs. The disintegration of the CNTs during sintering processes has previously been reported in many studies [81, 82, 83].

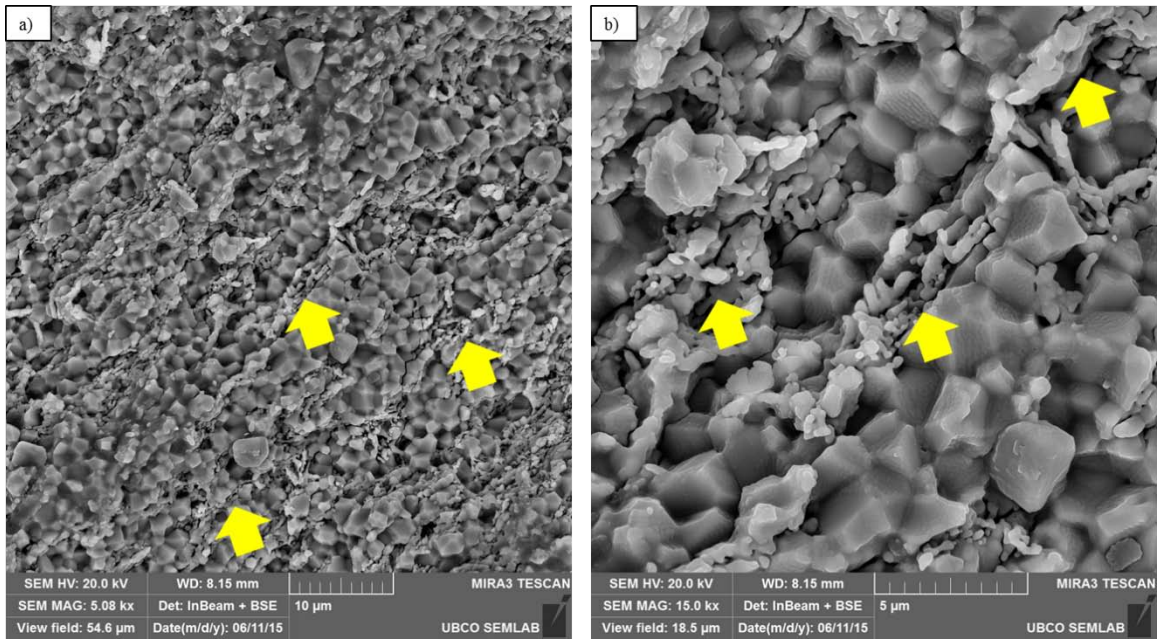


Figure 4.48: A secondary phase seen along the grain boundaries of the 1wt% MWCNT-YSZ composite at: a) 5000x and b) 15000x magnification.

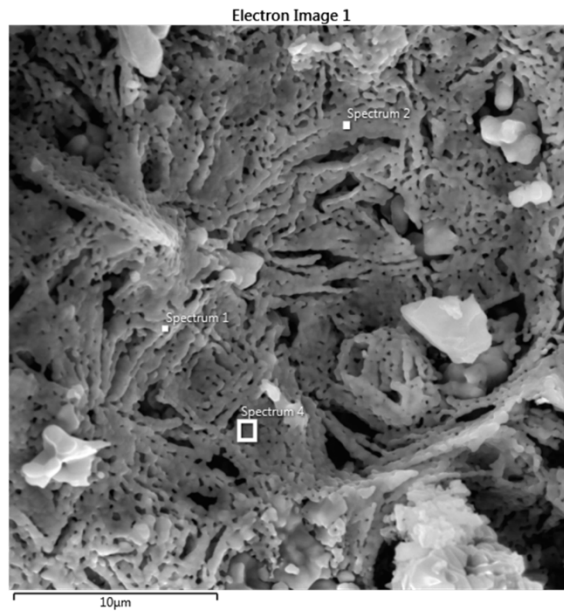


Figure 4.49: A secondary phase network in 1wt% MWCNT-YSZ composite.

Table 4.9: Composition of the second phase network as obtained from the X-EDS analysis.

Spectrum Label (Wt%)	Spectrum 1	Spectrum 2	Spectrum 3
C	11.86	16.67	18.60
O	30.76	29.26	25.83
Al	-	1.02	0.81
Fe	1.72	1.64	1.44
Y	41.20	35.69	32.68
Zr	14.45	15.73	20.64
Total	100.00	100.00	100.00

4.3.2.2 Hardness Measurement of the MWCNT-YSZ Ceramic Composites

The Vickers micro hardness results of the MWCNT-YSZ ceramic composites are summarized in Figure 4.50. It was seen that the average hardness of the composites was marginally higher than that of pure YSZ. However, considering the high standard deviation in the measurements, the effect of MWCNTs on the hardness was not statistically significant.

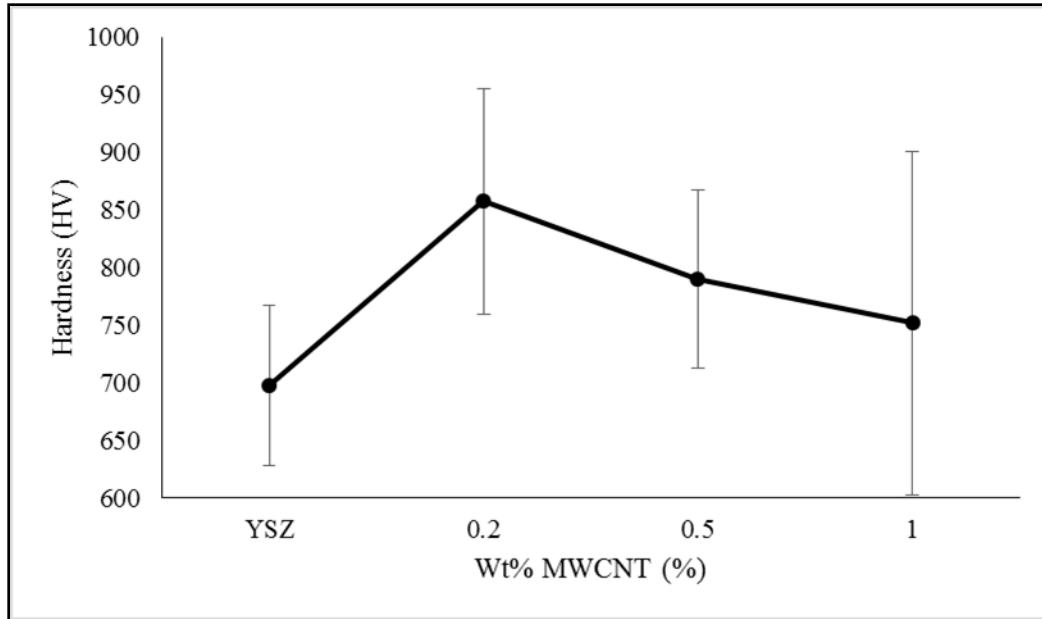


Figure 4.50: Hardness of the MWCNT-YSZ ceramic composites.

The increased hardness could be a consequence of the presence of the MWCNTs along the grain boundaries, hindering grain boundary sliding. In some sites, the MWCNTs were seen to be bridging two adjacent grains therefore possibly contributing to increased toughness of the ceramic composite, as shown in Figure 4.51.

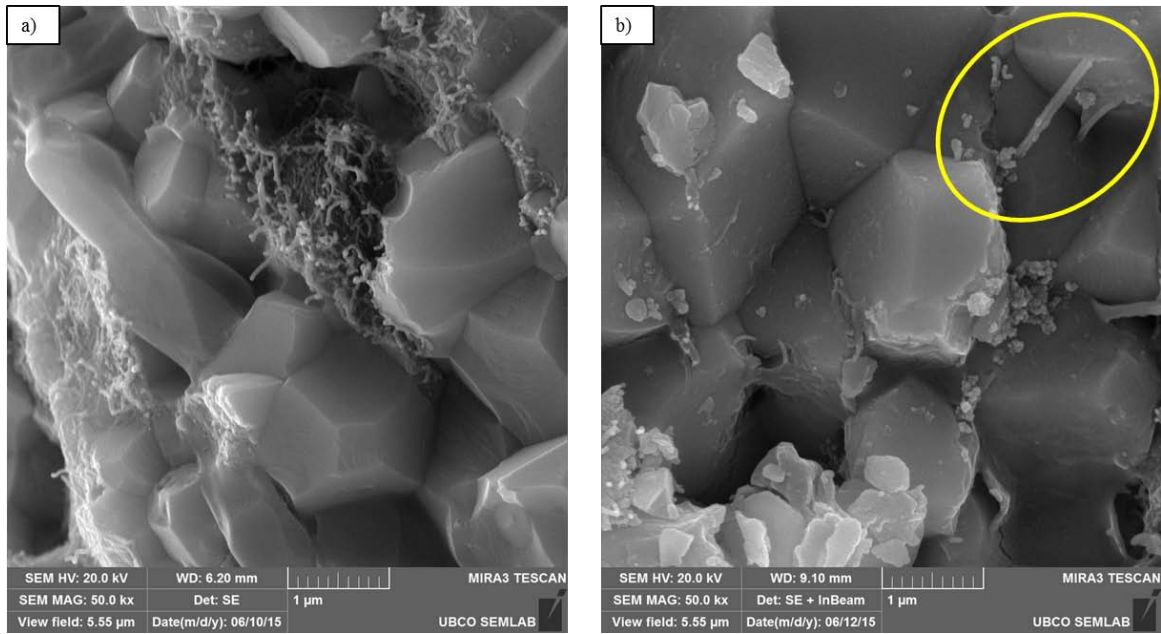


Figure 4.51: a) MWCNTs seen along the grain boundaries of 0.2wt% MWCNT-YSZ composite and b) Grain boundary pinning effect seen in 0.5wt% MWCNT-YSZ composite.

In conclusion, the addition of MWCNTs only marginally affected the hardness of the MWCNT-YSZ ceramic composites.

Chapter 5: CONCLUSIONS

The conclusions for this work are categorized into three sections:

5.1 Densification of 8mol% YSZ

- The final density of the as-sintered samples depends on the sintering parameters, such as the sintering temperature, pressure, heating and cooling rate.
- Intermediate dwelling at 600°C, resulted in samples with higher density as compared to dwelling at 1000°C.
- Tetragonal to monoclinic phase transformation was seen to be more pronounced in the samples dwelled at 1000°C.
- Formation of the YCl glassy phase had a detrimental effect on the integrity of the samples.
- The sintering dwell time did not have any appreciable effect on the final density of the as-sintered samples.

5.2 Processing and Characterization of SWCNT-YSZ Ceramic Composites

- SWCNTs hindered particle rearrangement and hindered the densification of the SWCNT-YSZ ceramic composites.
- SWCNTs delayed the densification process.
- The two peak nature of the densification rate curves, seen in case of pure YSZ was not noticeable in the presence of the SWCNTs.
- The SWCNTs increased the electrical resistance of the ceramic composites.

- At relatively lower compositions (0.2 and 0.5 wt%) SWCNT were found along the grain boundaries with no agglomerations.
- The SWCNTs did not disintegrate during the sintering process.
- In case of 1wt% SWCNT-YSZ ceramic composite, some SWCNT agglomeration was seen. The SWCNT agglomerations introduced a new densification mechanism, seen in the form of faceted growth of the matrix YSZ grains.
- Addition of SWCNTs reduced the grain size of the composites.
- SWCNTs increased the overall bulk hardness of the ceramic composites. The SWCNT-YSZ composites possibly followed the inverse Hall-Petch effect for the hardness. This was seen as increase in hardness with the increase in the grain size.
- The overall increase in the hardness of the SWCNT-YSZ composites was due to the presence of the SWCNTs along the grain boundaries.
- The NI-hardness and Young's modulus of the composites decreased with the increase in the SWCNT content.
- The matrix grains of the SWCNT composites softened with the addition of the SWCNTs.
- Specific heat of the composites did not change significantly with the addition of SWCNTs, but increased with increase in temperature.
- The thermal conductivity and the thermal diffusivity of the composites decreased with the addition of the SWCNTs.

5.3 Processing and Characterization of MWCNT-YSZ Ceramic

Composites

- The addition of the MWCNTs had a very minor effect on the densification process as there were only minor differences in the densification curves with the introduction of the MWCNTs.
- The final densities of the composites decreased with the addition of the MWCNTs.
- There was no appreciable change in the grain size of the composite matrix with the addition of the MWCNTs.
- MWCNT agglomerations were seen in all the composites of the MWCNT-YSZ ceramic.
- In 1wt% MWCNT-YSZ ceramic composites, the MWCNTs disintegrated during the sintering process.
- The average hardness of the MWCNT-YSZ ceramic composites marginally increased with the addition of MWCNTs.

Chapter 6: RECOMMENDATIONS FOR FUTURE WORK

The suggested recommendations for future work based on the work done and the results obtained in this thesis are enlisted below.

6.1 Densification of 8mol% YSZ by SPS

1. Study in detail the densification mechanism of 8mol% YSZ. This could be carried out by studying the microstructure of the compacted discs by pausing the sintering cycle at intermediate stages and determining the microstructural evolution during the sintering process.
2. Study the mechanical and thermal properties of the as-sintered YSZ compacts and investigate the effect of varying sintering parameters on the mechanical properties of the sintered discs.
3. Study the effect of initial grain size and geometry on the sintering behavior and mechanical properties of the sintered YSZ discs.
4. Determine a method to sinter layered discs of a base metal and YSZ, and compare the mechanical and thermal performance of the as-sintered and as-sprayed component for thermal barrier coating application.

6.2 Processing and Characterization of As-Sintered SWCNT-YSZ

Ceramic Composites

Determine the bulk Young's modulus, stiffness and plastic deformation of 0.2, 0.5 and 1wt% SWCNT-YSZ ceramic composites and compare the results with the reported nano-properties of the ceramic composites.

6.3 Processing and Characterization of As-Sintered MWCNT-YSZ

Ceramic Composites

1. Study in detail the effect of MWCNTs on the densification behavior of as-sintered MWCNT-YSZ ceramic composites.
2. Determine a more efficient mixing procedure to ensure homogenous distribution of the MWCNTs in the YSZ matrix.
3. Determine sintering parameters to avoid disintegration of the MWCNTs during the sintering process.
4. Study the mechanical and thermal properties of the as-sintered MWCNT-YSZ ceramic composites.

Bibliography

- [1] W. H. Duckworth, A. D. Schwoppe, O. K. Salmassy, R. L. Carlson and H. Z. Schofield, "Mechanical property test on ceramic bodies," Battelle Memorial Institute, Columbus, Ohio, 1952.
- [2] R. Ramamoorthy, P. K. Dutta and S. A. Akbar, "Oxygen sensors: Materials, methods, designs and applications," *Journal of Materials Science*, vol. 38, no. 21, pp. 4271 - 4282, 2003.
- [3] W. C. Maskell and B. C. H. Steele, "Solid state potentiometric oxygen gas sensors," *Journal of Applied Electrochemistry*, vol. 16, no. 4, pp. 475 - 489, 1986.
- [4] F. A. Administration, "FAA forecast predicts air travel to double in two decades," 2012.
- [5] W. Pan, S. R. Phillpot, C. Wan, A. Chernatynskiy and Z. Qu, "Low thermal conductivity oxides," *BRS Bulletin - Thermal-barrier coatings for more efficient gas turbine engines*, vol. 37, no. 10, pp. 917 - 21, October 2012.
- [6] D. M. Krestos, "An X-Ray Diffraction investigation of α -Al₂O₃ addition to yttria stabilized zirconia (YSZ) thermal barrier coatings subject to destabilizing vanadium pentoxide (V2O5) exposure," Naval Post Graduate School, Monterey, CA, 1993.
- [7] W. D. Kingery, *Introduction to Ceramics*, New York: Wiley Interscience, 1976.
- [8] J. Spišiak, M. Hartmanova, G. G. Knab and S. Krcho, "Thermal properties of Yttria Stabilized Zirconia (SPS)," *Journal of European Ceramic Society*, vol. 11, no. 6, pp.

509-514, 1993.

- [9] H. Zhou, J. Li, D. Yi and L. Xiao, "Effects of manganese oxide on the sintered properties of 8YSZ," *Physics Procedia*, vol. 22, pp. 14-19, 2011.
- [10] X. Wang, Q. Li, J. Xie, Z. Jin, J. Wang, Y. Li, K. Jiang and S. Fan, "Fabrication of ultralong and electrically uniform single-walled carbon nanotubes on clean substrates," *Nano Letters*, vol. 9, no. 9, pp. 3137 - 3141, 2009.
- [11] M. Suárez, A. Fernández, H. U. Kessel, J. Hennicke, J. L. Menéndez, R. Kirchner, R. Torrecillas and T. Kessel, Challenges and opportunities for spark plasma sintering: a key technology for a new generation of materials, INTECH Open Access Publisher, 2013.
- [12] C. Sun, R. Hui, W. Qu and S. Yick, "Progress in corrosion resistant materials for super critical water reactors," *Journal of Corrosion Science*, vol. 51, no. 11, pp. 2508 - 2523, 2009.
- [13] K. Obradović-Đuričić, V. Medić, S. Dodić, D. Gavrilov, Đ. Antonijević and M. Zrilić, "Dilemmas in zirconia bonding : A review," *Srpski arhiv za celokupno lekarstvo*, vol. 141, no. 5-6, pp. 395 - 401, 2013.
- [14] "Temperature-dependent phase transitions of ZrO₂," Materials Design Inc ., Angel Fire, NM 87710, USA, 2009.
- [15] G. K. Bansal and A. H. Heuer, "On a martensitic phase transformation in zirconia (ZrO₂) - I. Metallographic evidence," *Acta Metallurgica*, vol. 20, no. 11, pp. 1281 -

1289, 1972.

- [16] J. E. Bailey, "The monoclinic - tetragonal transformation and associated twinning in thin films of zirconia," *Proceedings of the Royal Society A*, vol. 279, pp. 395-412, 1964.
- [17] X. Xia, "Computational modelling study of yttria stabilized zirconia," Doctoral dissertation, University College of London, 2010.
- [18] A. G. Evans and R. M. Cannon, "Toughening of brittle solids by martensitic transformations," *Acta Materialia*, vol. 34, no. 5, pp. 761 - 800, 1986.
- [19] B. Basu, "Toughening of yttria-stabilised tetragonal zirconia ceramics," *International Materials Rev*, vol. 50, no. 4, pp. 239-56, 2005.
- [20] X. J. Jin, "Martensitic transformation in zirconia containing ceramics and its applications," *Current Opinion in Solid State and Materials Science*, vol. 9, no. 6, pp. 313 - 318, 2005.
- [21] D. A. Porter, K. E. Easterling and M. Sherif, *Phase Transformation in Metals and Alloys*, CRC Press, 2011.
- [22] Y. L. Zhang, X. J. Jin and T. Y. Hsu, "Thermodynamic calculation of M_s in ZrO_2 - CeO_2 - Y_2O_3 system," *Journal of European Ceramic Society*, vol. 23, no. 5, pp. 685-690, 2003.
- [23] N. S. Jacobson, "Thermodynamic properties of some metal oxide-zirconia systems," NASA Technical Memorandum 102351, National aeronautics and space administration,

Cleveland, OH, Lewis Research Center., 1989.

- [24] Y. Zhang, V. Ji and K. W. Xu, "The detailed geometrical and electronic structures of monoclinic zirconia," *Journal of Physics and Chemistry of Solids*, vol. 74, no. 3, pp. 518-523, 2013.
- [25] J. E. Alaniz, F. G. Perez-Gutierrez, G. Aguilar and J. E. Garay, "Optical properties of transparent nanocrystalline Ytria Stabilized Zirconia," *Optical Materials*, vol. 32, no. 1, pp. 62-68, 2009.
- [26] E. Farshihagho, "Pyrolysis of yttria stabilized zirconia and its characterization," 2013.
- [27] X. J. Chen, K. A. Khor, S. H. Chan and L. G. Yu, "Preparation of yttria stabilized zirconia electrolyte by spark plasma sintering," *Materials Science and Engineering*, vol. A341, no. 1, pp. 43-48, 2003.
- [28] T. M. Yonushonis, "Overview of thermal barrier coatings in diesel engines," *Journal of Thermal Spray Technology*, vol. 6, no. 1, pp. 50-56, 1997.
- [29] R. Dutton, R. Wheeler, K. S. Ravichandran and K. An, "Effect of heat treatment on the thermal conductivity of plasma-sprayed thermal barrier coatings," *Journal of Thermal Spray Technology*, vol. 9, no. 2, pp. 204-209, 2000.
- [30] M. Tokita, "Mechanism of spark plasma sintering," in *Proceeding of NEDO - International Symposium on Functionally Graded Materials*, Japan, 1999.
- [31] P. Dahl, I. Kaus, Z. Zhao, M. Johnsson, M. Nygren, K. Wiik, T. Grande and M. A.

- Einarsrud, "Densification and properties of zirconia prepared by three different sintering techniques," *Ceramics International*, vol. 33, no. 8, pp. 1603-1610, 2007.
- [32] Y. Bangchao and J. Jiawen, "Spark plasma sintering the 8mol% yttria stabilized zirconia electrolyte," *Journal of Materials Science*, vol. 39, pp. 6863-6865, 2004.
- [33] G. Bernard-Granger, A. Addad, G. Fantozzi, G. Bonnefont, C. Guizard and D. Vernat, "Spark plasma sintering of commercially available granulated zirconia powders: comparison with hot-pressing," *Acta Materialia*, vol. 58, no. 9, pp. 3390-3399, 2010.
- [34] A. Robert, "Spark Plasma Sintering," *Ceramic Industry Magazine*, Elgin, Ill, 2008.
- [35] S. Grasso, Y. Sakka and G. Maizza, "Effects of initial punch - die clearance in spark plasma sintering process," *Materials Transaction JIM*, vol. 12, pp. 2899-2906, 2008.
- [36] S. Grasso, Y. Sakka and G. Maizza, "Pressure effects on temperature distribution during spark plasma sintering with graphite sample," *Materials Transactions*, vol. 50, no. 8, pp. 2111-2114, 2009.
- [37] X. J. Chen, K. A. Khor, S. H. Chan and L. G. Yu, "Preparation of yttria stabilized zirconia electrolyte by spark plasma sintering," *Materials Science and Engineering*, vol. A341, pp. 43-48, 2003.
- [38] R. Chaim, S. Amit and C. Estournes, "Densification of Y₂O₃ ceramic powder by spark plasma sintering," *Journal of European Ceramic Society*, vol. 29, pp. 91-98, 2009.
- [39] A. W. Curtin and W. B. Sheldon, "CNT-reinforced ceramics and metals," *Materials*

Today, vol. 7, pp. 44-9, 2004.

- [40] U. Anselmi-Tamburini, J. E. Garay and Z. A. Munir, "Fast low-temperature consolidation of bulk nanometric ceramic materials," *Scripta Materialia*, vol. 54, no. 5, pp. 823-828, 2006.
- [41] T. Takeuchi, I. Kondoh, N. Tamari, N. Balakrishnan, K. Nomura, H. Kageyama and Y. Takeda, "Improvement of mechanical strength of 8 mol% yttria-stabilized zirconia ceramics by spark plasma sintering," *Journal of The Electrochemical Society*, vol. 149, no. 4, pp. 455-461, 2002.
- [42] R. S. Ruoff, D. Qian and W. K. Liu, "Mechanical properties of carbon nanotubes: theoretical predictions and experimental measurements," *Comptes Rendus Physique*, vol. 4, no. 9, pp. 993-1008, 2003.
- [43] C. Laurent, E. Flahaut and A. Peigney, "The weight and density of carbon nanotubes versus the number of walls and diameter," *Carbon*, vol. 48, no. 10, pp. 2994-2996, 2010.
- [44] O. Lourie and H. D. Wagner, "Evaluation of Young's modulus of carbon nanotubes by micro-Raman spectroscopy," *Journal of Materials Research*, vol. 13, pp. 2418-2422, 1998.
- [45] M. F. Yu, B. S. Files, S. Arepalli and R. S. Ruoff, "Tensile loading of ropes of single wall carbon nanotubes and their mechanical properties," *Physical Review Letters*, vol. 84, no. 24, pp. 5552-5555, 2000.

- [46] C. E. Inglis, "Stresses in a plate due to the presence of cracks and sharp corners," *Royal Institute of Naval Architects Transactions*, vol. 55, pp. 219-230, 1913.
- [47] A. A. Griffith, "A crack energetical analysis," *Philosophical Transactions of the Royal Society of London A*, vol. 221, p. 163, 1920.
- [48] S. S. Samal and S. Bal, "Carbon nanotube reinforced ceramic matrix composites - A review," *Journal of Minerals and Materials Characterization and Engineering*, vol. 7, no. 4, pp. 355-370, 2008.
- [49] I. Ahmad, A. Kennedy and Y. Q. Zhu, "Carbon Nanotubes reinforcing MgO doped Al₂O₃ nanocomposites," in *ECCM13: 13th European Conference on Composite Materials*, 2008.
- [50] S. C. Tjong, *Carbon nanotube reinforced composites: metal and ceramic matrices*, John Wiley and Sons, 2009.
- [51] R. Z. Ma, J. Wu, B. Q. Wei, J. Liang and D. H. Wu, "Processing and properties of carbon nanotubes-nano-SiC ceramic," *Journal of Material Science*, vol. 33, pp. 5243-5246, 1998.
- [52] J. Hurst, "Fracture toughness enhancements in carbon nanotube reinforced ceramic matrix composites," NASA Glenn Research Centre, Cleveland, Ohio, 2003.
- [53] Y. Go and T. Hashida, *Carbon Nanotube reinforced alumina composite materials*, INTECH Open Access Publisher, 2012.

- [54] B. Milsom, G. Viola, Z. Gao, F. Inam, T. Peijs and M. J. Reece, "The effect of carbon nanotubes on the sintering behaviour of zirconia," *Journal of European Ceramic Society*, vol. 32, pp. 4149-4156, 2012.
- [55] S. d. B. Martin, R. Poyato, D. G. Garcia and A. D. Rodriguez, "Processing of SWCNT-reinforced yttria stabilized zirconia by spark plasma sintering and microstructure characterization," *Journal of Nano Research*, Vols. 18-19, pp. 317-323, 2012.
- [56] M. Mehdi, M. Daniele, S. Robert, B. Guillaume and F. Gilbert, "Processing of yttria stabilized zirconia reinforced with multi-walled carbon nanotubes with attractive mechanical properties," *Journal of European Ceramic Society*, 2010.
- [57] A. Datye, K. H. Wu, G. Gomes, V. Monroy, H. T. Lin, J. Vleugels and K. Vanmeensel, "Synthesis, microstructure and mechanical properties of yttria stabilized zirconia (3YTZP) - Multi - walled nanotube (MWNTs) nanocomposite by direct in - situ growth of MWNTs on zirconia particles," *Composites Science and Technology*, vol. 70, pp. 2086 - 2092, 2010.
- [58] S. Jung-Hoo and H. Seong-Hyeon, "Microstructure and mechanical properties of single wall carbon nanotube reinforced yttria stabilized zirconia ceramics," *Materials Science and Engineering A*, vol. 556, pp. 382-387, 2012.
- [59] Inframat Advanced Materials, "8 mol% YSZ Powder (Product # 4039OR- 8601)," Manchester, USA.
- [60] ASTM, "C1327-08. Standard Test Method for Vickers Indentation Hardness of

Advanced Ceramics," Standard A.S.T.M, 2003.

- [61] ASTM, "E1461-13 Standard Test Method for Thermal Diffusivity by the Flash Method," ASTM.
- [62] B. Okolo, V. Schulze, A. Wanner and D. Lohe, "The residual stress state in sintered yttria-stabilized zirconia micro-specimens," 2007.
- [63] L. Bichler and D. Sediako, "Phase evolution and residual stress measurement in yttria stabilized zirconia based composites prepared by spark plasma sintering technique," CNBC, 2014.
- [64] U. Anselmi-Tamburini, S. Gennari, J. E. Garay and Z. A. Munir, "Fundamental investigations on the spark plasma sintering / synthesis process: ii. Modelling of current and temperature distributions," *Materials Science and Engineering A*, vol. 394, no. 1, pp. 139-148, 2005.
- [65] G. B. Granger and C. Guizard, "Spark plasma sintering of a commercially available granulated zirconia powder: I.Sintering path and hypothesis about the mechanism(s) controlling densification," *Acta Materialia*, vol. 55, pp. 3493-3504, 2007.
- [66] J. Rösler, H. Harders and M. Bäker, *Mechanical Behaviour of Engineering Materials - Metals, Ceramics, Polymers and Composites*, Springer, 2007.
- [67] "Sigma - Aldrich product," SIGMA - ALDRICH, [Online]. Available: <http://www.sigmaaldrich.com/catalog/product/aldrich/450103?lang=en®ion=CA>.

- [68] S.-M. Lee, Y.-w. Jun, S.-N. Cho and J. Cheon, "Single crystalline star-shaped nanocrystals and their evolution: Programming the geometry of nano-building blocks," *Journal of American Chemical Society Communications*, vol. 124, pp. 11244-11245, 2002.
- [69] N. J. Petch, "The cleavage strength of polycrystals," *Journal of Iron and Steel Institute*, 1953.
- [70] E. O. Hall, "The deformation and aging of mild steel: discussion of results," *Proceedings of the Physical Society B*, 1951.
- [71] C. E. Carlton and P. J. Ferreira, "What is behind the inverse Hall-Petch effect in nanocrystalline materials," *Acta Materialia*, vol. 55, pp. 3749-56, 2007.
- [72] A. H. Choksi, A. Rosen, J. Karch and H. Gleiter, "On the validity of the Hall Petch relationship in nanocrystalline materials," *Scripta Metallurgica*, vol. 23, pp. 1679-1684, 1989.
- [73] J. P. Zhou, Q. M. Gong, K. Y. Yuan, J. J. Wu, Y. F. Chen, C. S. Li and J. Liang, "The effects of multiwalled carbon nanotubes on the hot-pressed 3 mol% yttria stabilized zirconia ceramics," *Materials Science and Engineering A*, no. 520, pp. 153-157, 2009.
- [74] W. D. Callister and D. G. Rethwisch, *Materials Science and Engineering An Introduction*, John Wiley and Sons, Inc, 2000.
- [75] *A Dictionary of Physics*, Oxford University Press, 2009.

- [76] A. H. Compton, "The variation of the specific heat of solids with temperature," *Physical Review*, no. 6.5, p. 377, 1915.
- [77] D. R. Lide, Ed., CRC Handbook of Chemistry and Physics, 73 ed., CRC Press, 1993, pp. 4-146.
- [78] W. J. Parker, R. j. Jenkins, C. P. Butler and G. L. Abbott, "A flash method of determining thermal diffusivity, heat capacity and thermal conductivity," *Journal of Applied Physics*, vol. 32, p. 1679, 1961.
- [79] A. M. Limarga and D. R. Clarke, "The grain size and temperature dependence of the thermal conductivity of polycrystalline, tetragonal yttria stabilized zirconia," *Applied Physics Letters*, vol. 98, p. 211906, 2011.
- [80] G.-D. Zhan and A. K. Mukherjee, "Processing and characterization of nanocomposites with interesting structural and functional properties," *Reviews on Advanced Materials Science*, vol. 10, pp. 185-196, 2005.
- [81] J. Sun and L. Gao, "Development of a dispersion process for carbon nanotubes in ceramic matrix by heterocoagulation," *Carbon*, vol. 41, no. 5, pp. 1063-1068, 2003.
- [82] H. J. Dai, "Carbon nanotubes: opportunities and challenges," *Surface Science*, vol. 500, no. 1-3, pp. 218-241, 2002.
- [83] S. Rul, F. Lefevre-Schlick, C. Laurent and A. Peigney, " Percolation of single-walled carbon nanotubes in ceramic matrix nanocomposites," *Acta Materialia*, vol. 52, no. 4,

pp. 1061-1067, 2004.

- [84] J. A. Greenwood, "Constriction Resistance and the Real Area of Contact," *British Journal of Applied Physics*, vol. 17, pp. 1621-1632, 1966.
- [85] M. Runde, "Mass Transport in Stationary Contact Points," *Components, Hybrids and Manufacturing Technology*, vol. 10, pp. 89-99, 1987.
- [86] M.-. d. Nono and C.-. d.-. Andrade, "Tetragonal to monoclinic transformation influence on the mechanical properties of CeO₂-ZrO₂ ceramics," *Materials Science Forum*, vol. 498, pp. 506-511, 2005.
- [87] R. C. Garvie, R. H. Hannink and R. T. Pascoe, "Ceramic Steel?," *Nature*, vol. 258, pp. 703 - 704, 1975.
- [88] S. J. L. Kang, *Sintering : Densification, Grain Growth and Microstructure*, Butterworth-Heinemann, 2004.

Appendix A: Grain Size Distribution Curves

Based on the observations of the grain size measurements, the grain size distribution plots have been made for samples from sections 4.2.1, 4.2.2 and 4.3.1 and shown in Figure A.1, Figure A.2 and Figure A.3, respectively. The grain size distribution plots are as follows:

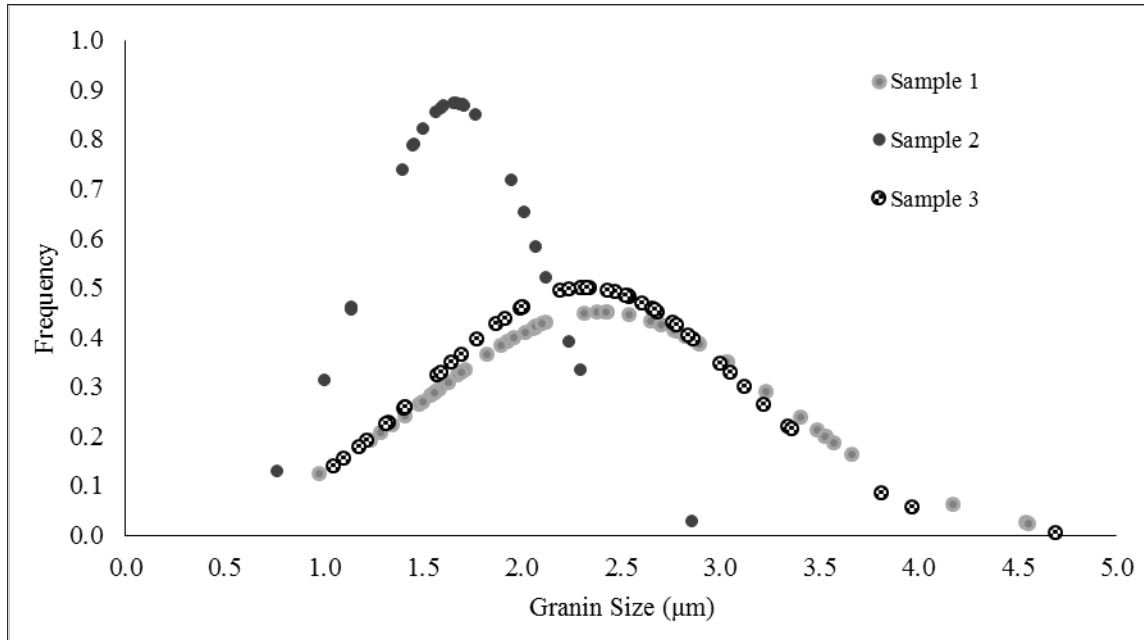


Figure A.1: Grain size distribution for samples of Group 1

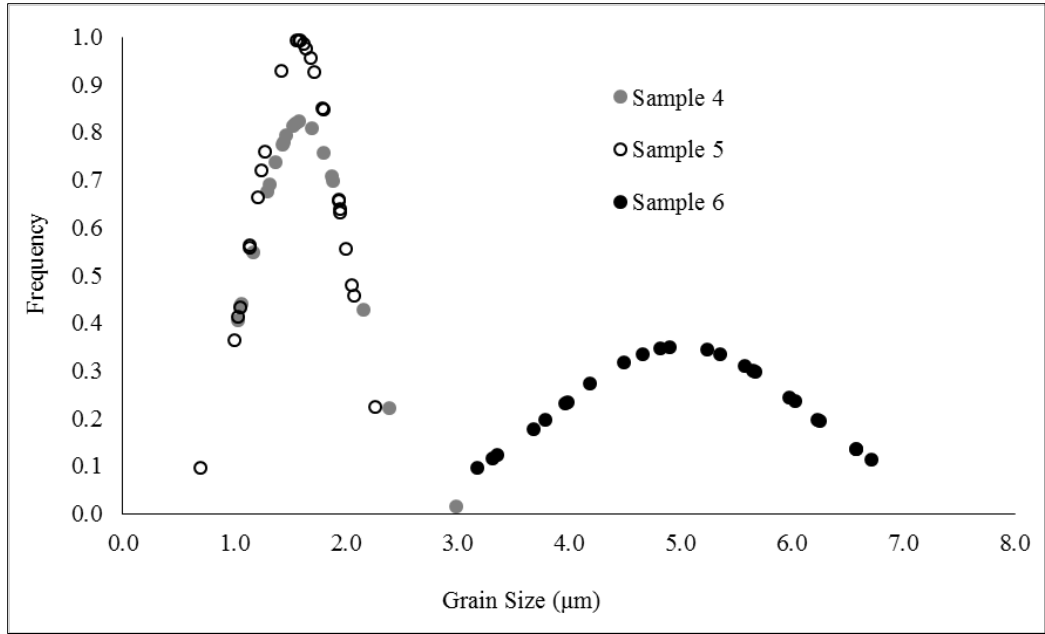


Figure A.2: Grain size distribution of samples of Group 2

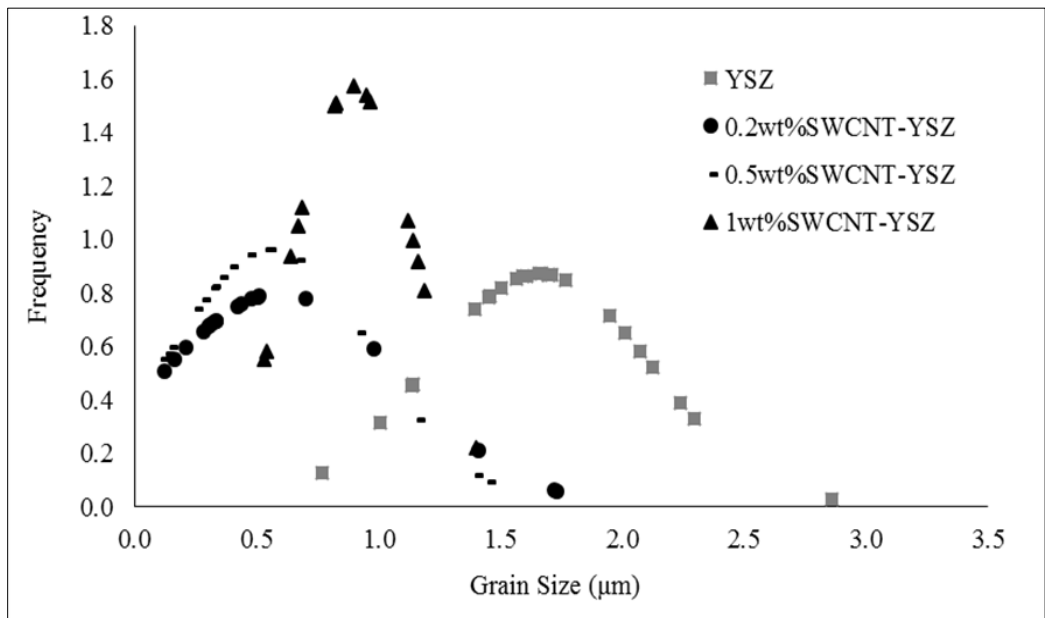


Figure A.3: Grain size distribution of SWCNT-YSZ ceramic composites